Delft University of Technology

Development of Magnetocaloric Wax Composites for Biodegradable Membranes for Microfluidic Platforms

MSc Biomedical Engineering

Pornpawee Uliss

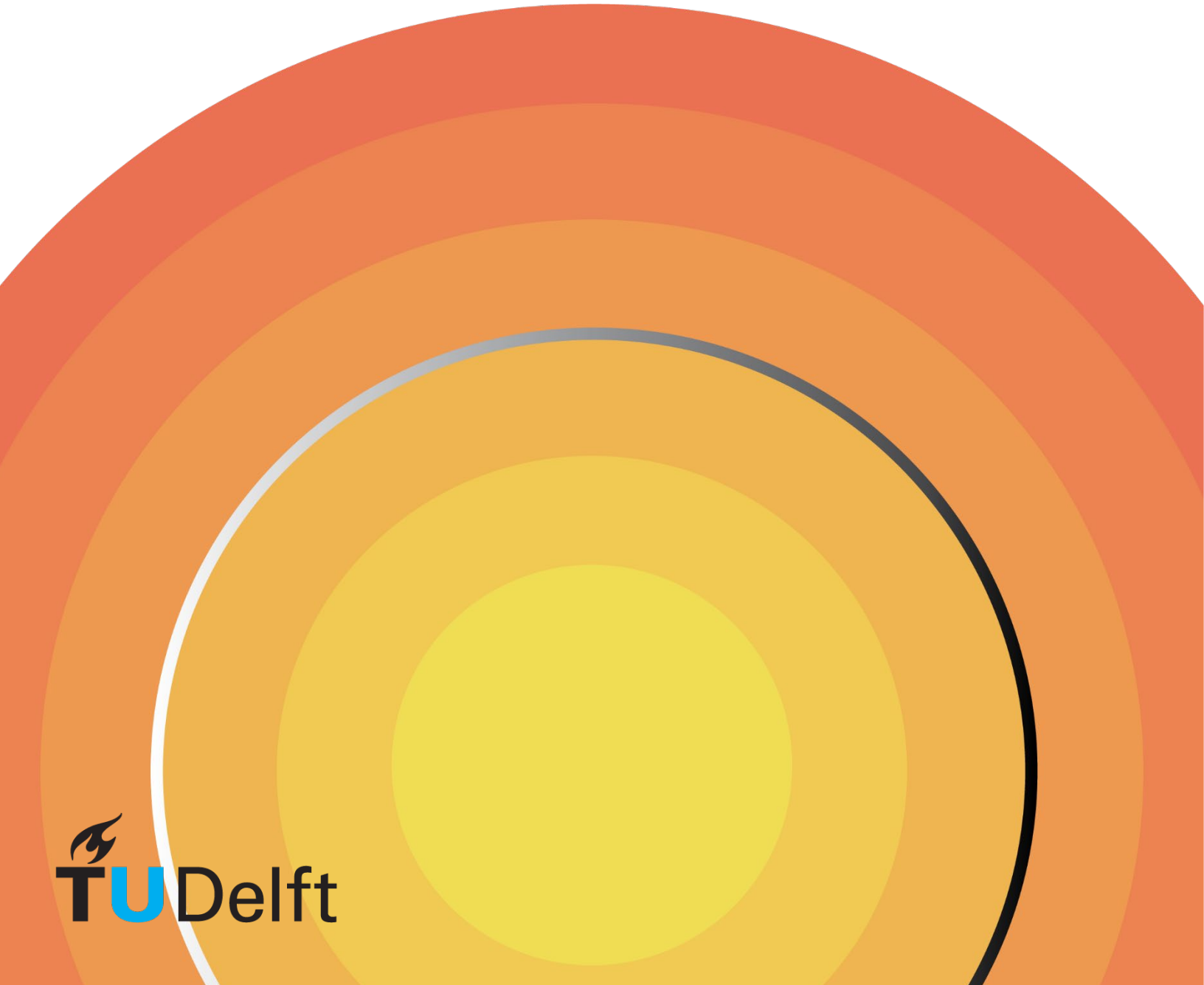

Development of Magnetocaloric Wax Composites for Biodegradable Membranes for Microfluidic Platforms

by

Pornpawee Uliss

in partial fulfillment of the requirements for the degree of

Master of Science in Biomedical Engineering

Specialization in Medical Devices and Biodegradable Technologies at Delft University of Technology

to be defended publicly on Wednesday, August 28th, 2024, at 02:00 PM

Student number:	5691044	
Project duration:	December 11, 2023 – August 28, 2024	
Thesis committee:	Dr. Clementine Boutry	TU Delft, Supervisor
	Prof. Ekkes Brück	TU Delft, Supervisor
	Prof. Jenny Dankelman	TU Delft
	Prof. Leon Abelman	TU Delft

TU Delft

Acknowledgement

This report encapsulates nearly a year of my research journey, a roller-coaster ride filled with numerous experiences. Throughout this time, I have encountered both highs and lows, yet I firmly believe that every experience, whether good or bad, has been beneficial. During the course of my master's thesis, I have learned and tried many new things, each of which has enriched and strengthened me. These memorable experiences have not only shaped my personality as a researcher and engineer but have also prepared me mentally to embrace opportunities and learn from mistakes.

I would like to extend my heartfelt gratitude to several individuals. My deepest thanks go to Prof. Ekkes Bruck and Dr. Clementine Boutry, whose invaluable guidance and direction have been instrumental in navigating this project. Dr. Clementine Boutry, thank you for giving me the opportunity to explore this thesis topic and for your unwavering support and insightful suggestions. Prof. Ekkes Bruck, I have greatly benefited from our discussions. Your availability and willingness to assist whenever I sought your advice have been immensely helpful.

I also extend my sincere thanks to the ECTM and FAME groups for their support. Thank you, Prof. Niels van Dijk, for your guidance during our weekly FAME group meetings. Thank you, Hang Gai, for your guidance on synthesizing materials and for explaining some background knowledge that enhanced my understanding of the results. Thank you, Bert, for always being willing to help me make quartz tubes, and to Sebastian and Anton for assisting me with the DSC and SQUID machines. I am also grateful to the EKL team for our valuable discussions, and to Filip Simjanoski for ensuring a conducive working environment.

Finally, I would like to extend my deepest gratitude to my parents and my beloved pets in Thailand for their unwavering emotional support. A special thank you to my grandfather, my first teacher, who opened the door to the world of science for me and has always believed in my success.

Abstract

In recent years, there has been growing interest in the magnetocaloric effect (MCE) which is a magneto-thermodynamic phenomenon observed in certain magnetic materials. MCE materials undergo temperature changes when subjected to magnetic fields. Researchers are now exploring the possibilities of utilizing this material in biomedical application technologies, as they offer the potential for non-invasive control of their properties through external magnetic fields. However, there is a lack of research on suitable magnetic compositions that exhibit desired magnetic properties for medical purposes, while ensuring no adverse effects on the cells.

This master project explores the potential of a magnetocaloric $(Mn,Fe)_2(P,Si)$-based compound as a biodegradable membrane for multi-cell separation in organ-on-chip platforms. $Mn_{0.65}Fe_{1.30}Si_{0.37}P_{0.65}$ compound was selected due to its sharp phase transition characteristics and tunable Curie temperature (T_c), which enable self-regulation of temperature within the therapeutic range, thus preventing potential damage to living cells. The synthesized $Mn_{0.65}Fe_{1.30}Si_{0.37}P_{0.65}$ compound exhibited a transition temperature of 316 K (43°C) with particle sizes ranging from 1-5 µm. A magnetocaloric wax-based composite was synthesized by integrating these particles with a wax component. Characterization under alternating magnetic fields (AMF) showed a significant temperature rise with higher magnetic concentrations and field amplitudes. At an applied AMF of 9 mT and a frequency of 244 kHz, a sample containing 15 vol.% magnetic particles stabilized at 44°C, effectively maintaining controlled temperatures within the therapeutic range (42-47°C) and efficiently melting the wax without harming living cells. Water absorption tests and SEM imaging further demonstrated the composite's low water permeability and minimal development of microcracks over time. These findings validate the potential of magnetocaloric materials with adjustable Curie temperatures for precise self-regulation of temperature in biomedical applications. The observed high heating efficiency and prevention of overheating offer promising opportunities for controlled thermal activation processes across various biomedical fields.

Content

List of Figures

List of Tables

Nomenclature

Abbreviations

Abbreviation	Definition
PCM	Phase change material
MCE	Magnetocaloric effect
MCM	Magnetocaloric material
M	Magnetization
H	Magnetic field
AMF	Alternating magnetic field
SCT	Self-controlled temperature
Fe_3O_4	Iron(II,III) oxide
GMCE	Giant magnetocaloric effect
FOMT	First-order magnetic phase transition
SOMT	Second-order magnetic phase transition
MPS	Mononuclear phagocyte system
CIP	Carbonyl iron powder
PNIPAM	Poly(N-isopropylacrylamide)
LCST	Lower critical solution temperature
FeRh	Iron-rhodium
M-SMP	Magnetic shape memory polymer
SMP	Shape memory polymer
NdFeB	Neodymium magnet
HEBM	High-Energy ball milling
$C_{18}H_{34}O_2$	Oleic acid
TEM	Transmission electron microscopy
SEM	Scanning electron microscopy
OoC	Organ-on-chip
EC	Endothelial cell
ECM	Extra cellular matrix
W	Tungsten
Mo	Molybdenum
AC	Active carbon
PBS	Phosphate-buffered saline
PLGA	Poly(lactic-co-glycolic) acid
PDMS	Polydimethylsiloxane
XRD	X-ray diffraction
SQUID	Superconducting quantum interference device
RSO	Reciprocating sample option
CEM43	Cumulative equivalent minutes at 43°C
BBW	Bayberry wax
TAG	Triacylglycerol
MAG	Monoacylglycerol

DAG	Diacylglycerol

Symbols

Symbol	Definition	Unit
μ	Magnetic moment	
μ_S	Spin angular moment	
μ_L	Orbital angular moment	
$\vec{\mu}_{total}$	Total magnetic moment	
$\vec{J}$	Total angular momentum vector	
$\vec{S}$	Total spin angular momentum vector	
$\vec{L}$	Total orbital angular momentum vector	
μ_0	Permeability of the vacuum	[4π x 10^{-7} N A^{-2}]
μ_B	Bohr magneton	[9.27 x 10^{-24} Am^2]
g_J	Landé spectroscopic g-factor	
χ	Susceptibility	
C	Curie constant	
T_C	Curie temperature	[K]
T	Temperature	[K] or [°C]
M_s	Saturation magnetization	[Am^2/Kg]
M_r	Remanent magnetization	[Am^2/Kg]
H_c	Coercive field or coercivity	[kA/m]
$\mu_0 H$	Applied magnetic field	[T]
A	Amount of heat released via hysteresis loss	[kJ/m^3]
ΔT_{ad}	Adiabatic temperature change	[K]
ΔE	Magnetic anisotropy energy barrier	
ΔS	Magnetic entropy	
C_p	Heat capacity	[J/°C]
C_s	Specific heat capacity	[J/kg °C]
G	Gibbs free energy	
B_h	High frequency AC magnetic field	
B_a	DC magnetic field	
m_s	Mass of the sample	[g]
m_p	Mass of magnetic particles in the composite	[g]
SLP	Specific loss power	[W/kg]

1

Introduction

1.1. Motivation for Magnetocaloric Composite

In recent years, the magnetocaloric effect (MCE) has gained significant interest due to its unique magneto-thermodynamic properties observed in certain magnetic materials. The MCE occurs when these materials undergo a change in magnetic alignment in response to an applied magnetic field, leading to a corresponding change in temperature. Specifically, the application or removal of a magnetic field results in the material heating up or cooling down, respectively. This phenomenon has attracted attention for its potential in energy-efficient technologies, such as magnetic refrigeration and magnetic heat pump. Currently, the exploration of MCE materials for biomedical applications has opened new avenues, particularly for noninvasive control via external magnetic fields. Notably, the transition temperature (T_c) of these materials can be precisely regulated within a desired therapeutic range, thereby mitigating the risk of overheating which may lead to severe cell damage. Magnetic materials that exhibit a large magnetocaloric effect with sharp phase transition, so called first-order magnetic phase transition (FOMT), hold promise for integration into medical implants and organ-on-chip (OoC) technology.

Despite the promising properties of magnetocaloric materials, such as excellent magnetization, tunable transition temperatures, and non-toxic compositions, comprehensive research on their performance in medical applications remains limited. Among magnetocaloric materials, $(Mn,Fe)_2(P,Si)$-based magnetocaloric compound is selected to investigate further. It has shown potential as heating agents for biodegradable membranes in vascularized organ-on-chip platforms. It has been reported that the co-culturing of organoids and vascular cells at an early stage can impede proper development, making precise timing crucial for co-seeding. Traditionally, organoids and vascular cells are cultured separately off-chip until they reach sufficient differentiation, a process that can be streamlined by an integrated approach. A promising strategy involves developing an organoid-on-chip platform featuring a non-permeable barrier membrane that separates the two cell cultures. When the cultures are ready for co-culturing, the membrane can be triggered to be degraded by heat generated from magnetic particles exposed to a magnetic field. This allows cell cultures to interact when the appropriate time has been reached.

In this master's project, magnetocaloric materials, $(Mn,Fe)_2(P, Si)$-based compound has been investigated. This compound exhibits outstanding properties, such as excellent magnetization and tunable critical temperatures, and consists of non-toxic elements. By adjusting their chemical composition, the Curie temperature of the compounds can be finely tuned, making them suitable as magnetic heating agents in magnetic composites for transient membranes. Natural wax, a phase change material (PCM), is also explored for its potential application as a binder for encapsulating magnetic particles. Its hydrophobic properties and compatibility make it a promising candidate for effectively separating two culture cells until they reach the appropriate maturation stage. This research project primarily focuses on the fabrication and characterization of magnetocaloric composites for biodegradable membranes. The central research question of this master's thesis is:

"How can a magnetocaloric wax composite be fabricated for a biodegradable membrane to facilitate the temporary separation of organoids and perfusable vascular networks in a microfluidic platform?"

This study aims to investigate the fabrication and characterization of $(Mn,Fe)_2(P,Si)$-based compounds, tuning their properties with respect to their transition temperature (T_c) and other essential properties for the intended biomedical application. Another focus will be on developing a magnetocaloric wax-based composite and exploring its performance as a biodegradable membrane for cell separation in organ-on-chip platforms.

1.2. Overview of the Report

In **Chapter 2**, the report delves into the background of the study, exploring the theoretical knowledge of magnetic materials and the mechanisms of heat generation in magnetic particles. It also discusses examples of applications utilizing magnetic particles as heating agents. Moreover, the chapter reviews the vascularized organoid-on-chip platform and the latest advancements in the fabrication and characterization of wax composites. **Chapter 3** provides details of the conducted experiments in this master's project, including the choice of materials, the fabrication techniques used to synthesis magnetic particles and wax composites, along with the characterization methods to evaluate the magnetic properties and heating performances of synthesized magnetocaloric particles to be able to be used as a heating agent for biodegradable membrane. In **Chapter 4**, the results of experiments are presented and discussed, and **Chapter 5** offers future recommendations based on the findings. Finally, **Chapter 6** concludes the report, summarizing the key insights and implications of the research.

2

Background

2.1. Magnetic Materials

This section details the theoretical frameworks that are related to the master's research project. Initially, it starts with the fundamental concepts of magnetic materials, the mechanisms underlying heat generation in magnetic particles, and the review of some applications of magnetic materials used in biomedical fields. Subsequently, it discusses the current development of a vascularized organoid-on-chip platform, which serves as a focused application for this project. The section then presents a review of the literature focusing on the use of phase change materials (PCM), specifically wax-based composites, and their potential application as transient membrane materials. Finally, key insights obtained from the literature study and the objectives of the research project are explained, as well as the overview of the research plan.

2.1.1. The Basic Concept of Magnetism

Magnetic Moment

Magnetic ordering refers to the behavior of magnetic moments within a material. The magnetization of a material is the average magnetic moment of its atoms. Magnetic moments originate from the quantum mechanical properties of electrons at the atomic level. There are two aspects regarding the study of magnetic order by concerning the nature of the magnetic order: the ground-state arrangement of the magnetic moments and the process of ordering itself (i.e., phase transition and critical behavior near the transition temperature). The magnetic moment (μ) is determined by two components: the intrinsic spin of the electrons (spin angular moment, μ_S) and the orbital motion of the electrons around the nucleus (orbital angular moment, μ_L). The total angular momentum vector ($\vec{J}$) can be approximated using the following formula (**Eq. 2.1**). It is the sum of the total spin angular momentum vector ($\vec{S} = \Sigma_i \vec{s_l}$) and the total orbital angular momentum vector ($\vec{L} = \Sigma_i \vec{l_l}$).

$$\vec{J} = \vec{L} + \vec{S} \qquad \textbf{(Eq. 2.1)}$$

The total magnetic moment ($\vec{\mu}_{total}$) for the Landé spectroscopic g-factor (g_J) is used to predict the moment of the atom during its ground state or when subjected to a weak magnetic field. The equation is represented based on **Eq. 2.2**, where μ_B is the Bohr magneton, $\mu_B = e\bar{h}/2m_e =$ 9.27 x 10^{-24} Am^2 and $g_J = 1 + \frac{J(J+1)+S(S+1)-L(L+1)}{2J(J+1)}$, where the value of J, L, and S can be determined by using Hund's rules.

$$\vec{\mu}_{total} cos\theta = -g_J \mu_B J \qquad \textbf{(Eq. 2.2)}$$

Based on the orientation and interaction of magnetic moments, magnetic materials can be classified according to their response to an applied magnetic field. These categories include ferromagnetism, antiferromagnetism, and ferrimagnetism, diamagnetism, and paramagnetism. **Figure 2.2** illustrates the alignment of magnetic moments in different magnetic states. In the paramagnetic state, the magnetic moments are randomly oriented. In contrast, the materials that exhibit ferromagnetism show fully aligned magnetic moments when subjected to an external magnetic field. Furthermore, ferromagnetic materials can maintain their magnetization even without an external magnetic field. This phenomenon is known as spontaneous magnetization. However, factors such as temperature can influence this alignment, which will be discussed further. Ferrimagnetic materials display a mixture of parallel and antiparallel-aligned magnetic moments, while antiferromagnetic materials show magnetic moments aligned in antiparallel directions, resulting in a net magnetic moment of zero.

Ferromagnetic Materials

Ferromagnetism is a phenomenon where a material can become a permanent magnet or strongly react to an external magnetic field. This behaviour arises due to the spontaneous parallel alignment of magnetic moments within the material. These magnetic moments are aligned in parallel within areas called magnetic domains, as represented in **Figure 2.1(left)**. This alignment is the result from the balance of several competing energy terms. When an external magnetic field changes over time, this energy equilibrium is disturbed, leading to rearrangements in the domain structure, primarily through the movement of the domain walls that separate neighbouring domains.

The various states of magnetization are demonstrated in **Figure 2.1(right)** by using the magnetization curve (M) as a function of applied magnetic field (H). Within the material, the magnetic domains tend to align themselves with the magnetic field direction when an external magnetic field is applied, resulting in a significant net magnetization of the material. The external magnetic field causes domain walls to move and leads to the growth of domains that are aligned with the magnetic field. The alignment of magnetic moments intensifies with the strength of the external field. At high field strengths, the material becomes uniformly magnetized in the direction of the applied field, forming a single large domain occupying the whole specimen and reaching saturation magnetization (M_s). Once the threshold is reached, any further increase in the field results in only a minimal increase in magnetization. The ordered arrangement of magnetic moments within each domain contributes to the strong magnetism, distinguishing ferromagnetic materials from paramagnetic materials and other magnetic materials.

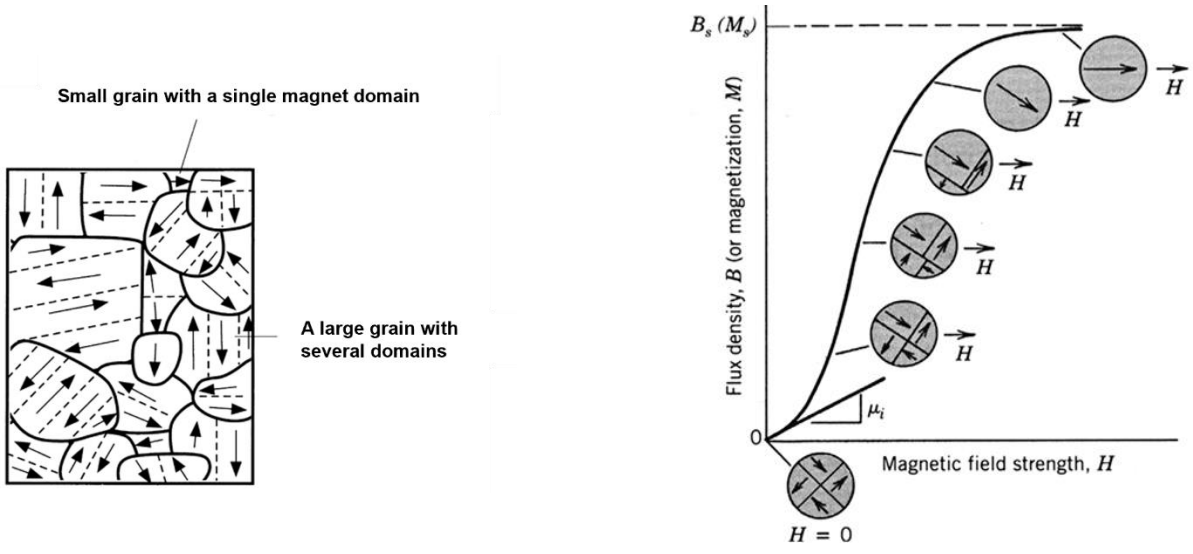

Figure 2.1 A schematic representation of magnetic domains within the grains in a ferromagnetic material (left) and the various states of magnetization (M) of the ferromagnetic material when subjected to external magnetic field (H) (right) (copied from [1]).

The magnetic behavior of ferromagnetic materials is characterized by the magnetization curve (M) as a function of applied magnetic field (H), as illustrated in **Figure 2.1(right)**. The ratio of magnetization (M) to the applied magnetic field (H), described by the following relation **(Eq. 2.3)**, is known as magnetic susceptibility (χ). Magnetic susceptibility reveals how a material responds to an applied magnetic field, helping to identify the magnetic nature of the material.

$$\chi = \frac{M}{H} \qquad \textbf{(Eq. 2.3)}$$

Materials with high magnetic susceptibility, such as ferromagnetic materials, become strongly magnetized even in relatively weak magnetic fields. This strong magnetization indicates a high degree of alignment of their magnetic moments with the external field, as illustrated in **Figure 2.2**. Ferrimagnetic materials, which exhibit a mixture of parallel and antiparallel-aligned magnetic moments, display magnetic behavior similar to ferromagnetic materials but typically possess lower saturation magnetization. In contrast, paramagnetic materials exhibit only a slight alignment of atomic magnetic moments in the direction of the applied field when subjected to a magnetic field, resulting in a small positive susceptibility. It exhibits rather weak positive magnetization compared to other types of magnetism and shows linear response to magnetic field. Antiferromagnetic materials exhibit an anti-parallel alignment of their atomic magnetic moments. This causes the magnetic fields to cancel each other out, making the material behave similarly to paramagnetic materials. The response of any material to the applied magnetic field (H) is called magnetic induction (B) and is defined by **Eq. 2.4**, where the magnetic constant (μ_0) = $4\pi \times 10^{-7}$ N A^{-2}.

$$B = \mu_0(H + M) \qquad \textbf{(Eq. 2.4)}$$

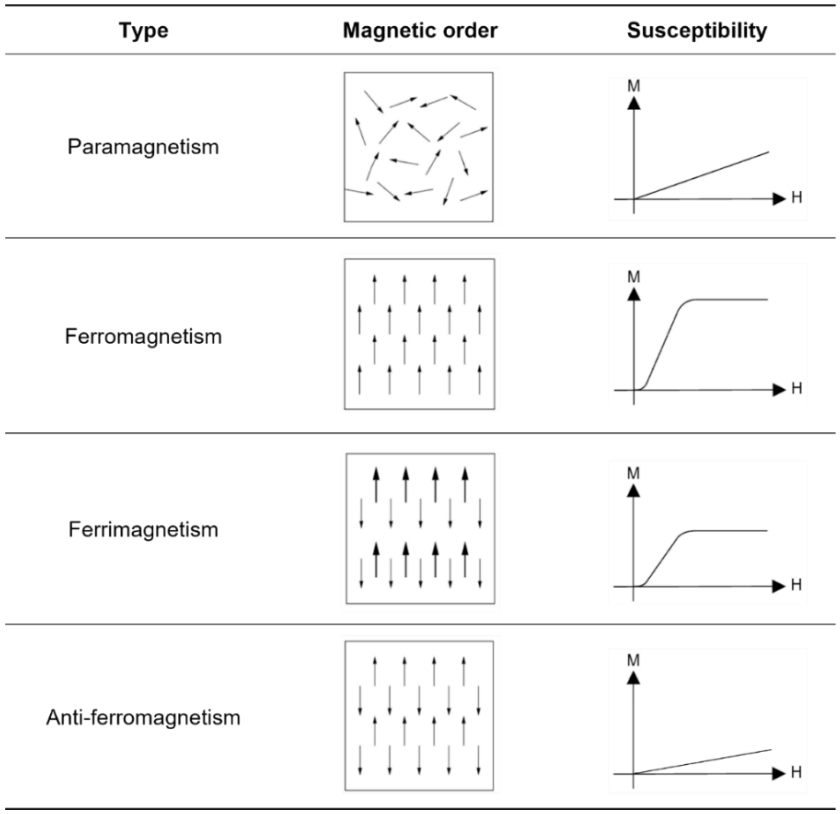

Figure 2.2 A schematic diagram of the different types of magnetic behaviour (adapted from [2]). In this table, “M” denotes magnetization, while “H” represents the applied magnetic field.

Effect of Temperature: Curie-Weiss Law

The materials with ordered magnetic structures, such as ferromagnetic materials, exhibit ferromagnetism only below a specific temperature known as the Curie temperature (T_c). At Tc, an order-disorder transition occurs, leading to the transformation from an ordered ferromagnetic state to a disordered paramagnetic state. This transition happens because, above Tc, the thermal energy becomes sufficient to overcome the exchange interactions that align the magnetic moments in the ferromagnetic state. Consequently, the orientation of magnetic order is destroyed, and the material transitions to a paramagnetic state where the magnetic moments are randomly oriented, resulting in minimal to zero magnetization even in the presence of an external magnetic field, as illustrated in **Figure 2.3**.

For ferromagnetic materials the temperature dependence of the susceptibility is described by the Curie-Weiss law. The Curie-Weiss law describes the susceptibility (χ) of a material above the Curie temperature, which is expressed as (**Eq. 2.5**):

$$\chi = \frac{C}{T - T_c} \qquad \textbf{(Eq. 2.5)}$$

Where χ is the magnetic susceptibility, C is the Curie constant, T is the temperature, and T_c is the Curie-Weiss temperature.

The susceptibility increases as the temperature decreases due to reduced thermal fluctuations. **Figure 2.3** illustrates the temperature dependence of χ comparing between paramagnetic and ferromagnetic materials. At low temperatures, the value of χ in paramagnetic materials is smaller in comparison with ferromagnetic materials and decreases steadily with increasing temperature ($\chi \propto 1/T$). In contrast, the value of χ in ferromagnetic materials is higher at low temperatures and drops rapidly as the temperature approaches T_c, where it transforms into a paramagnetic state. Tuning temperature threshold is crucial in applications requiring the self-regulation of temperature in magnetic particles used for transient membranes, discussed later in this report.

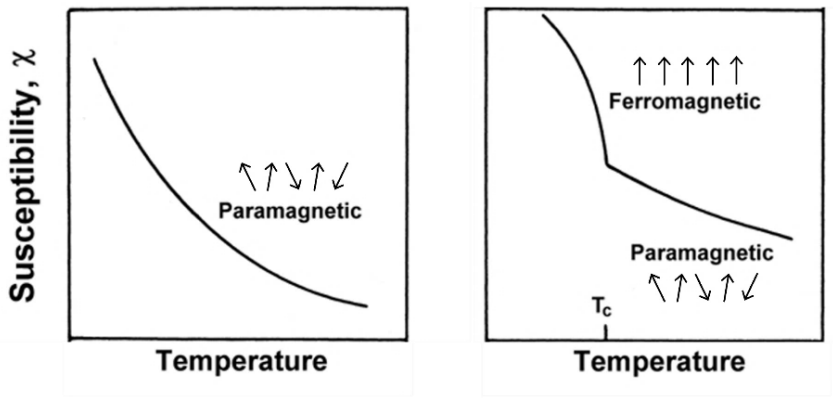

Figure 2.3 Temperature dependence of susceptibility in various magnetic materials (adjusted from [1]).

2.1.2. Mechanism of Heat Generation in Magnetic Particles

Under an alternating magnetic field (AMF), magnetic particles start to generate heat. The rate at which they heat up depends on the amplitude of the AMF, with higher AMF power resulting in greater heat production from the particles [3]. The heating process is mainly explained by hysteresis loss and Néel and Brownian

relaxation [4]. In addition to these mechanisms, heat generation through magnetocaloric effect (MCE) and eddy current is also explored in this section.

AC Hysteresis Loss

According to multi-domain magnetic particles with the size larger than approximately 40 nm, magnetic heating is usually delivered by hysteresis loss [5]. Generally, hysteresis loss is the mechanism that dominantly occurs in ferro/ferri-magnetic particles. Hysteresis loss occurs during the cycle of magnetization-demagnetization (**Figure 2.4**) when magnetic materials are subjected to an alternating applied magnetic field. According to the loop, there are three key parameters: (1) the saturation magnetization (M_s) represents the maximum level of magnetization that a material can achieve when subjected to a magnetic field, (2) the remanent magnetization (M_r), that is preserved magnetization in absence of field, and lastly (3) the coercivity or coercive field (H_c) denotes the field required for entire demagnetization.

As the applied magnetic field intensity increases, the magnetization (magnetic flux) increases. During this process, more domains rotate and align with the field until eventually all domains are aligned, reaching saturation magnetization (M_s). However, when the magnetic field intensity is decreased, the magnetization of the material does not decrease at the same rate and their domains also do not return to their original random orientation. Some domains remain aligned, resulting in a remanent magnetization (M_r). To reduce the magnetization to zero, a reverse magnetic field (H_c) must be applied to cause the domains to rotate in the opposite direction. Increasing the reverse field further causes the magnetization to saturate in the opposite direction, tracing out the characteristic hysteresis loop. The reorientation of magnetic moments in the material during the magnetization and demagnetization contributes to hysteresis losses during a hysteresis cycle [6]. The area of the hysteresis loop shows the energy required to complete full cycle of magnetizing and de-magnetizing. The loop of the area is crucial because it represents the amount of energy irreversibly transformed into heat during one magnetization cycle [7].

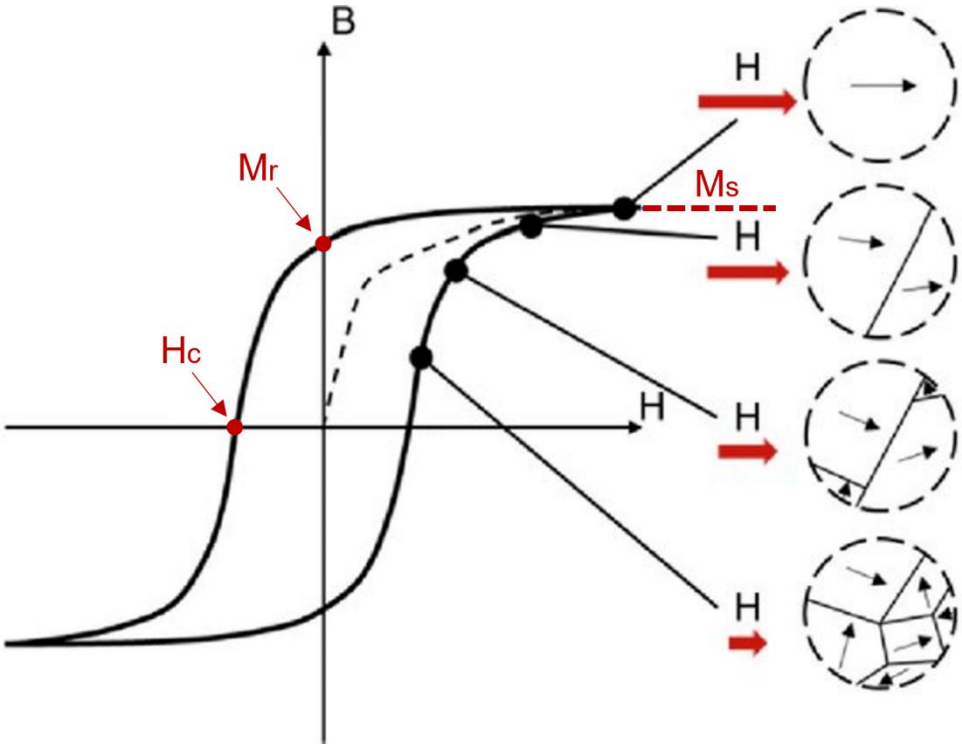

Figure 2.4 The schematic illustration of magnetic hysteresis loop. The magnetization (M) of the sample is plotted as a function of the magnetic field strength (H) (copied from [8]).

The amount of heat generated by this mechanism is proportional to the area of the magnetic hysteresis cycle and the applied frequency [9]. The area of hysteresis loss can be calculated based on **Eq. 2.6**, where H denote applied magnetic field, μ_0 is permeability, M is magnetization.

$$A = \int_{-H_{max}}^{+H_{max}} \mu_0 M(H)\, dH \qquad \textbf{(Eq. 2.6)}$$

The hysteresis losses were estimated using **Eq. 2.7**, where f is the frequency.

$$Hysteresis\ losses = Af \qquad \textbf{(Eq. 2.7)}$$

In practical aspects, especially in the biomedical field, magnetic materials are usually applied under small fields. Most studies report the range of the frequencies and AC fields ranging between 80 and 800 kHz and between 1 and 60 mT [10]. At low magnetic field strengths, from zero to about one oersted (Oe) or 80 A/m [11], the system falls into the region of minor loops, as shown in **Figure 2.5**. These minor loops can be observed, which always lie within the main hysteresis loop. These smaller loops do not reach M_s for applied fields below coercivity, $|H| < H_c$.

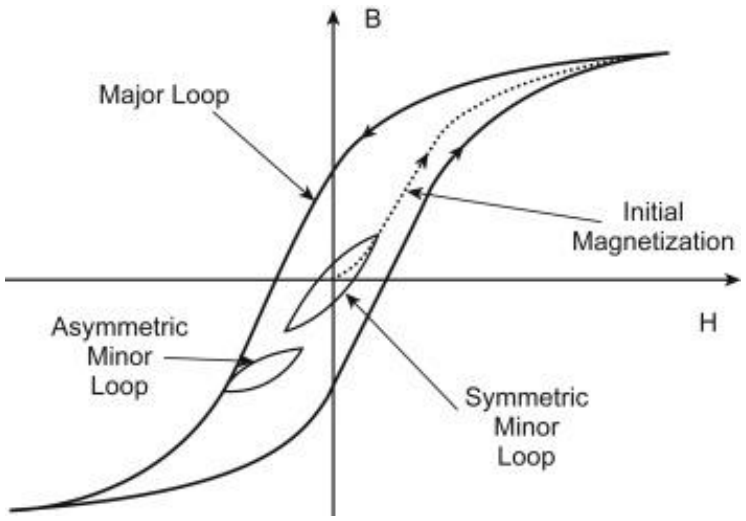

Figure 2.5 The magnetization curve and a set of symmetric minor hysteresis loops (copied from [12]).

Joule's Heating (Eddy Current)

In addition to hysteresis losses, eddy currents can also play a crucial role in heating [13]. When magnetic materials (conducting materials) are subjected to an alternating magnetic field (AMF), the system not only produces a magnetic field, but it also generates an electric field, inducing eddy currents. The induced eddy currents results in eddy current losses [14]. This induced current leads to a resistor heating called Joule's heating (Q). The eddy currents are concentrated at the skin of the conducting materials, between the outer surface and a level called skin depth (δ), **Eq. 2.8**, where σ is the conductivity of the material, μ is the permeability of conductor, and f is the excitation frequency, and only this area is heated. Depending on the testing frequency and tested specimen parameters such electrical conductivity and permeability [15], the density of induced eddy current falls exponentially from the surface with depth inside the specimen.

$$\delta \approx \frac{1}{\sqrt{\pi f \mu \sigma}} \quad \text{(Eq. 2.8)}$$

In the clinical application of magnetic hyperthermia heating, it is crucial to manage the generation of eddy currents to prevent undesired heating of normal tissues, which can lead to overheating issues. Currently, there is an established patient tolerable limit, known as the safety limit, which defines the acceptable levels of eddy current effects. One of the key parameters to consider is the product of the magnetic field amplitude and frequency (H x f). Considering smaller diameter of the exposed body region, Hergt et al. have suggested a safety limit for the product H x f $\leq 5 \times 10^9$ A m^{-1} s^{-1} [16].

Néel and Brownian Relaxation

Based on the process of hysteresis loss, the movement of domain walls appears to significantly contribute to heat generation. In contrast, when the size of magnetic particles decreases below a certain critical domain wall thickness, a single domain spin becomes energetically more favorable. In this configuration, the magnetic spin is aligned in the same direction, causing the particle to behave like a single giant magnetic moment. Magnetic nanoparticles with a size lower than 40 nm convert magnetic energy into thermal energy through magnetic relaxation [5]. Magnetic relaxation is governed by a combination of external rotation (Brownian relaxation) and internal rotation (Néel relaxation) of the magnetic moment of the particle. Under this regime, the magnetic moments of magnetic particles tend to align with the preferred direction of spontaneous magnetization, known as easy axis. As shown in **Figure 2.6**, a barrier of magnetocrystalline anisotropy energy separates the two opposite orientations (i.e., up and down) along this axis.

Under external AC magnetic field, Néel relaxation (τ_N) occurs when the easy axis of the particle is fixed and only the magnetic spin of the particles responds to the change in the external magnetic field, as shown in **Figure 2.6a**. An external magnetic field applied to supply energy sufficient to overcome the anisotropy energy barrier (ΔE) causes the magnetic spins to flip and release the given magnetic energy as heat. When the particle size increases, the magnetic energy barrier becomes high enough to hinder the Néel relaxation process, therefore preventing the flipping between two energetically favorable states. Due to this, Brownian relaxation (τ_B) becomes dominant. In this process, its magnetic moment rotates in the fluid, aligning its magnetic moment with the external magnetic field, as shown in **Figure 2.6b**. This rotation can overcome the viscous resistance of the medium, and the friction between the rotating particles and the surrounding fluid generates heat

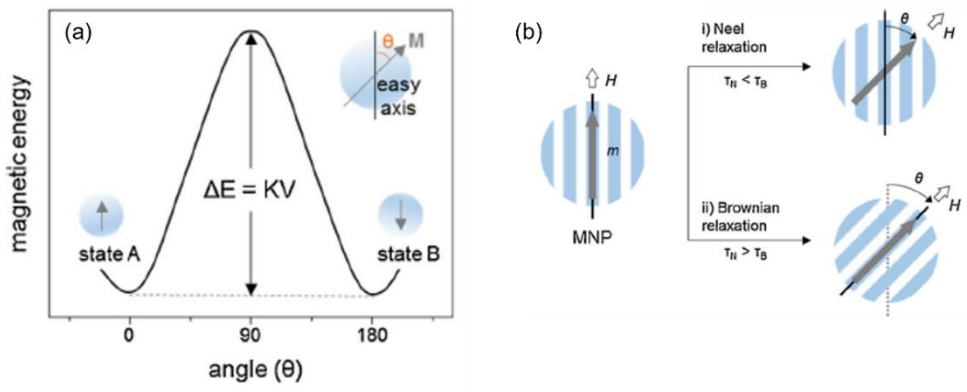

Figure 2.6 a) The magnetic anisotropy energy barrier (ΔE) varies with the angle between the easy axis and **b)** an illustration of magnetic loss in magnetic nanoparticles through Néel and Brownian relaxation mechanisms (copied from [17]).

Magnetocaloric Effect (MCE)

In recent years, there has been ongoing research regarding the magnetocaloric effect (MCE), which is one of the heat generation mechanisms of magnetic particles. It is a magneto-thermodynamic phenomenon observed in all magnetic materials. The magnetocaloric effect is the physical phenomenon where a magnetic material is heated or cooled when an external magnetic field is applied or removed. In general, as shown in **Figure 2.7**, when such materials are subjected to a magnetic field, they change their magnetic alignment, which causes a corresponding change in their temperature. When a magnetic field is applied to a magnetic material, its magnetic entropy (ΔS) decreases, leading to an increase in its lattice entropy and, consequently, an increase in temperature (ΔT). Conversely, when the magnetic field is removed, the material cools down, going back to the paramagnetic phase with randomly oriented spins and the magnetic entropy rises back again. MCE effect has gained attention for its potential in energy-saving technologies, such as magnetic refrigeration (cooling) and magnetocaloric heat pump (heating) [18].

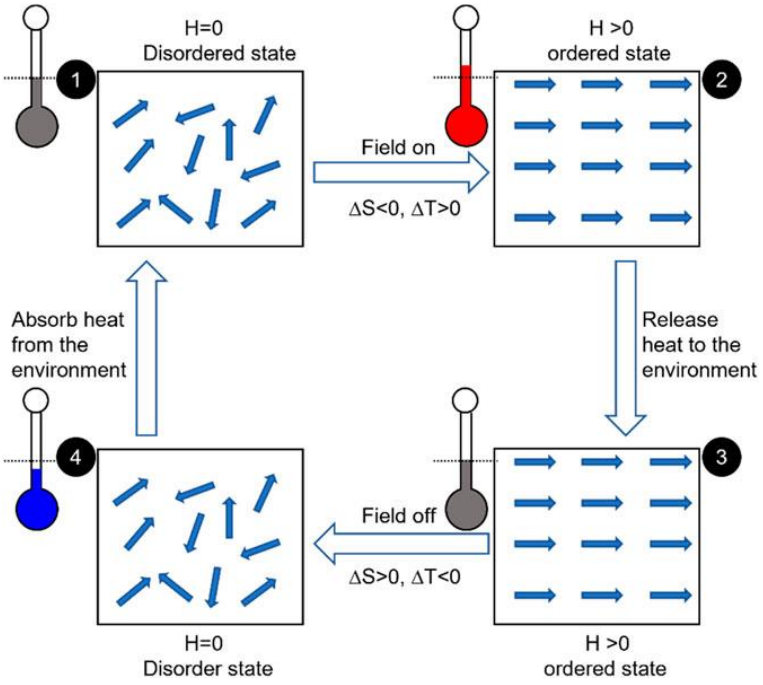

Figure 2.7 A schematic diagram of conventional magnetocaloric effect (copied from [19]).

The temperature change can be thermodynamically described by the following **Eq. 2.9**.

$$\Delta T_{ad}(T, \Delta H) - \int_{\mu_0 H_0}^{\mu_0 H_1} \frac{T}{C_p(T,H)} \left(\frac{\partial M}{\partial T}\right)_H dH \qquad \textbf{(Eq. 2.9)}$$

By measuring heat capacity, $C_p(T,H)$ and the temperature-dependent magnetization (M) under different applied magnetic fields, the adiabatic temperature change (ΔT_{ad}) of the magnetic system around temperature T can be calculated. $\mu_0 H_0$ is the initial applied magnetic field, while $\mu_0 H_1$ is the applied magnetic field. It is worth noting that although magnetocaloric materials can generate heat in the presence of a magnetic field under adiabatic conditions, triggering the magnetocaloric effect usually requires large magnetic fields on the order of 1 to 5 T [20].

2.1.3. Self-regulated Controlled by Transition Temperature (T_c)

As previously mentioned, the Curie temperature (T_c) is the critical temperature for a magnetic phase transition in magnetic materials. Below T_c, the magnetic compound exhibits ferri/ferromagnetic phases, while above T_c, it exhibits paramagnetic behavior. Ferromagnetic particles generate heat under an applied magnetic field, and their heating behavior can be interrupted at T_c. This self-regulation feature allows the magnetic particles to control their temperature based on their magnetic phase transition properties.

The term self-regulated refers to a system that can automatically regulate, monitor, or deactivate itself without external intervention once the target task is completed. The working principle of self-controlled temperature (SCT) is that once the temperature of the magnetic particles exceeds T_c under an external magnetic field, the phase of the magnetic particles transition to paramagnetic, as shown in **Figure 2.8**. At this point, the material will no longer respond to the external magnetic field, causing system magnetization to become very weak and halting further heating. With this, T_c serves as a threshold temperature for magnetic particles which help prevent overheating and potential damage to living cells.

The main physical challenge in effectively implementing SCT is maintaining the T_c of the magnetic particles within a therapeutic range, ensuring that it does not cause overheating issues to cells. However, the T_c of most magnetic materials is significantly higher than the desired range of 40-48°C [21]. For instance, the T_c of bulk Fe_3O_4 is 655°C [22]. Thus, the desired temperature range of T_c has gained attention for further investigation into its intended use. Several approaches have been pursued to reduce and control the high Curie temperature to achieve intended use for each application. It includes tuning various physical parameters such as chemical composition of the magnetic particles, crystal structure, geometric shape, and particle size [4].

Among the magnetic materials that exhibit a giant magnetocaloric effect (GMCE), those with a sharp phase transition have been taken into consideration. In general, magnetic materials with GMCE can be divided into two types of phase transitions: first-order magnetic phase transition (FOMT) and second-order magnetic phase transition (SOMT). The phase transitions are characterized by a discontinuity in the derivative of the Gibbs free energy (G) with respect to thermodynamic variables. In FOMT, this derivative is discontinuous, leading to an abrupt change in magnetization near the transition temperature (T_c), as illustrated in **Figure 2.8**. Conversely, SOMT materials exhibit a smooth and continuous transition at T_c, with the derivative changing gradually. The distinction between these types lies in the presence or absence of latent heat [23]. Moreover, the first-order magnetic transition materials display thermal hysteresis, while this phenomenon is absent in second-order magnetic phase transitions.

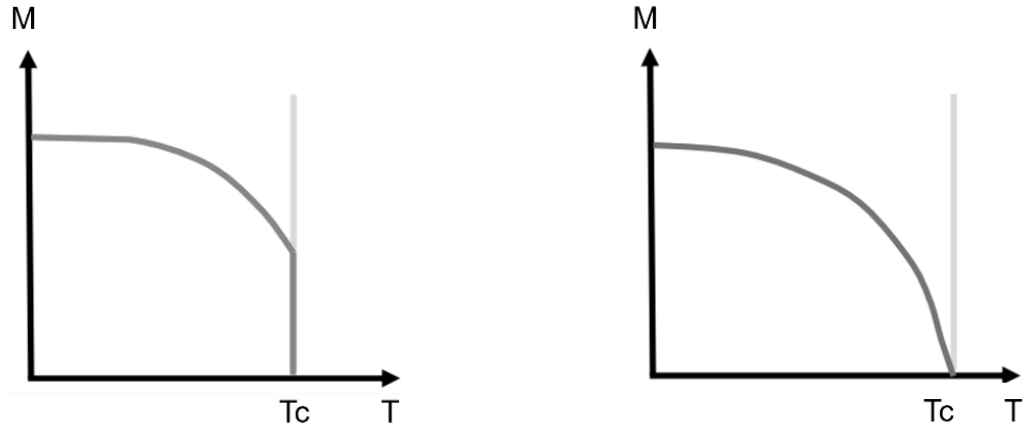

Figure 2.8 The difference in continuity between (left) first order magnetic phase transition (FOMT) and (right) second order magnetic phase transition (SOMT) (adjusted from [18]).

Among FOMT materials, compounds such as $(Mn,Fe)_2(P,Si)$ are particularly noteworthy due to their tunable Curie temperature [24], [25]. This compound is composed of non-toxic elements [26]. As a result, $(Mn,Fe)_2(P,Si)$-based compounds are promising candidates for magnetic particles exhibiting sharp phase transitions, with potential for use in biomedical applications.

2.1.4. The Use of Magnetic Materials in Biomedical Applications

Thermal energy is increasingly recognized as an important trigger for various applications in medical applications, especially in the field of drug-releasing systems [27], [28], [29] and hyperthermia treatment [30], [31]. Magnetic materials can be used as heating agents generating the local heating for intended activation. Magnetic heating exhibits more appealing properties than other physical stimuli (e.g., light) that are extensively used in biology and medicine. It has no penetration depth limit, is not attenuated by tissue, can be remotely controlled, and can be triggered on demand [32]. One possibility is using ferromagnetic materials for non-invasive control through an external alternating magnetic field (AMF).

There are a number of requirements for magnetic materials that are intended to be used with living cells or inside the human body. First, they must be biocompatible and not cause any adverse effects to the healthy cells. Second, the materials must be biodegradable or can be extracted from the human body after therapeutic procedure is completed. With this in mind, the size of the magnetic particles is significantly crucial. As shown in **Figure 2.9**, magnetic particles should be smaller than 8 μm to prevent blocking capillaries. For magnetic particles in the range of 10 nm to 8 μm, it can be taken up by the MPS immune system [33]. Third, in order to prevent adverse effects (i.e., overheating issue) that may cause severe damage to cell cultures, the temperature should be limited within the therapeutic range by controlling and maintaining the temperature between 41°C and 47°C for a given period [9].

Ferrimagnetic materials and ferromagnetic materials, such as iron oxide (II, III) (Fe_3O_4) and carbonyl iron powder (CIP), respectively, are commonly used as they exhibit outstanding magnetization in comparison with other magnetic materials and effectively undergo magnetic and thermodynamic changes when exposed to an external magnetic field. These materials appear to be biocompatible with the human body.

In the field of medical technology, the magnetothermal effect has been reported for use in induced pulsatile drug release system [29], hyperthermia treatment [30], and soft actuators for micro-soft robots [34]. Komlev et al. developed a composite coating for the controlled release of bioactive compounds under an external magnetic field, exploring its potential as an implant coating [29]. The composite coating primarily consists of Fe0.49Rh0.51, exhibiting a significant inverse magnetocaloric effect (-6 K/T), and PNIPAM, a thermosensitive polymer used to regulate the rate of drug release. Poly(N-isopropylacrylamide) (PNIPAM) has a lower critical solution temperature (LCST) of 32°C, making it hydrophilic (swollen) below this temperature, facilitating drug release. Above 32°C, corresponding to body temperature, PNIPAM becomes hydrophobic (collapsed), retaining the drug substances. The concept leverages the negative magnetocaloric effect, using a rapid cooling cycle achieved by quickly bringing a permanent magnet close to the drug container, thus changing the magnetic field from zero to 2 T and cooling the sample, triggering drug release, as illustrated in **Figure 2.10**.

Another application of the use of magnetothermal effect has been reported in hyperthermia treatment developed by Tan et al. [30]. A composite structure of 3D-printing magnetic PNIPAM hydrogel and elastomer was developed. Under an alternating magnetic field (AMF), magnetothermal-sensitive hydrogels (PNIPAM) encapsulated with Fe_3O_4 undergo a phase transition and abrupt volume collapse due to the magnetothermal effect. This shape-transformative structure can simultaneously encase and destroy cancer cells due to the temperature increase of magnetic hydrogel under magnetic field, as depicted in **Figure 2.11**. An alternating magnetic field with a current of 230 A was used to actuate the structure, maintaining a steady temperature above 50°C for 20 min, a temperature sufficient to cause thermoablation and damage to cancer cells and this can be controlled by changing the strength of alternating magnetic field. **Figure 2.11** shows the deformation process and temperature increase over time.

The magnetothermal effect has also been applied in soft actuators for soft robots. Ze et al. have developed a new magnetic shape memory polymer (M-SMP) with multifunctional features, including reprogrammable, untethered, reversible actuation and shape locking [34]. A soft gripper capable of grabbing objects is an example of application using the advantages of reversible actuation and shape locking of the M-SMP. The M-SMP comprises two forms of magnetic particles (Fe_3O_4 and NdFeB). Under a high frequency AC magnetic field (B_h), the Fe_3O_4 particles allow inductive heating, therefore enabling shape change when heated and shape locking when cooled, as illustrated in **Figure 2.12b** and **Figure 2.12c**. When the material was soft, the DC magnetic field (B_a) was applied, causing the NdFeB particles to move to align their magnetic field and then allowing the shape of the polymer to be manipulated. Moreover, NdFeB particles are able to remagnetized, allowing programmable deformation under an actuation magnetic field (B_a). For instance, the M-SMP strip can be magnetized with a desired magnetic profile, such as along its longitudinal direction or remagnetized into a folding shape, as shown in **Figure 2.12a** and **Figure 2.12d**.

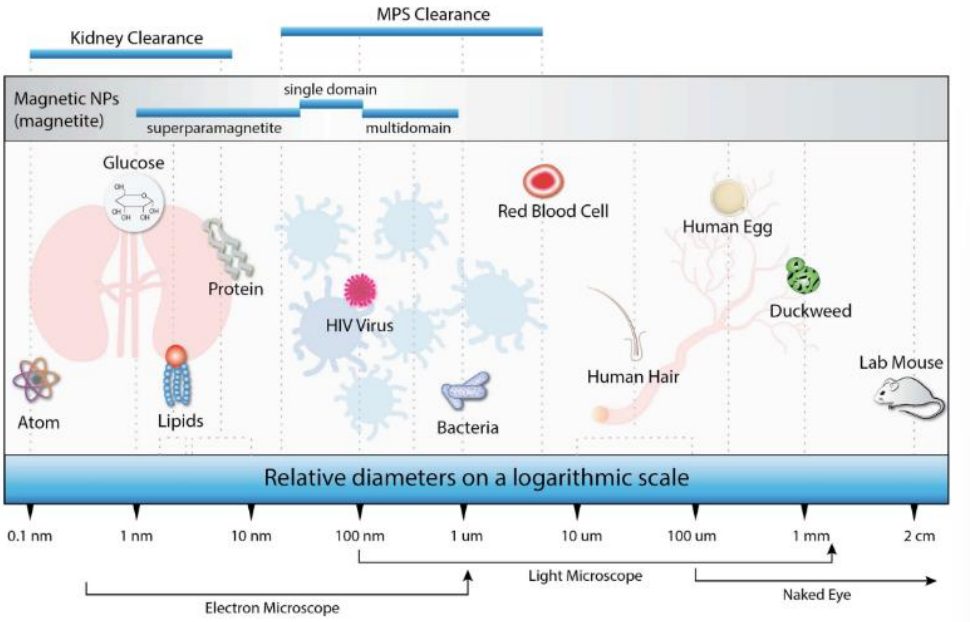

Figure 2.9 Size regimes for biological samples and magnetic particles, ranging from atomic level to lab mouse (copied from [33]).

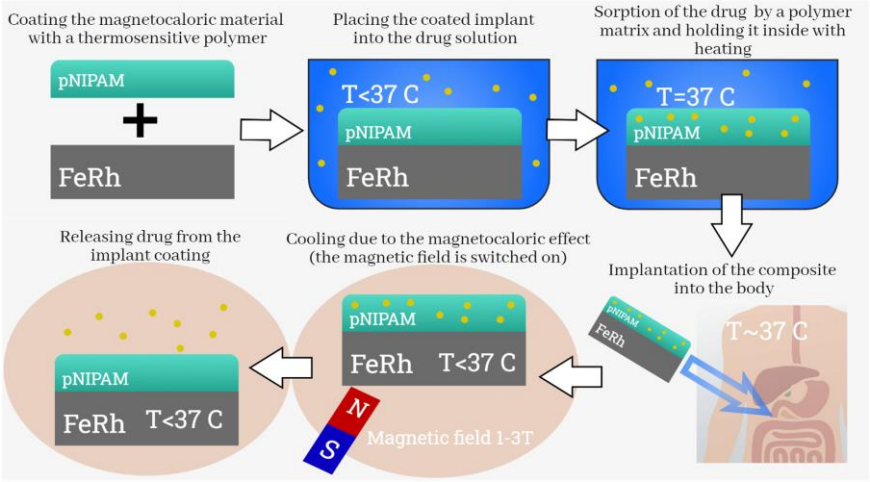

Figure 2.10 The general mechanism of the drug release from the implant's surface (copied from [29]).

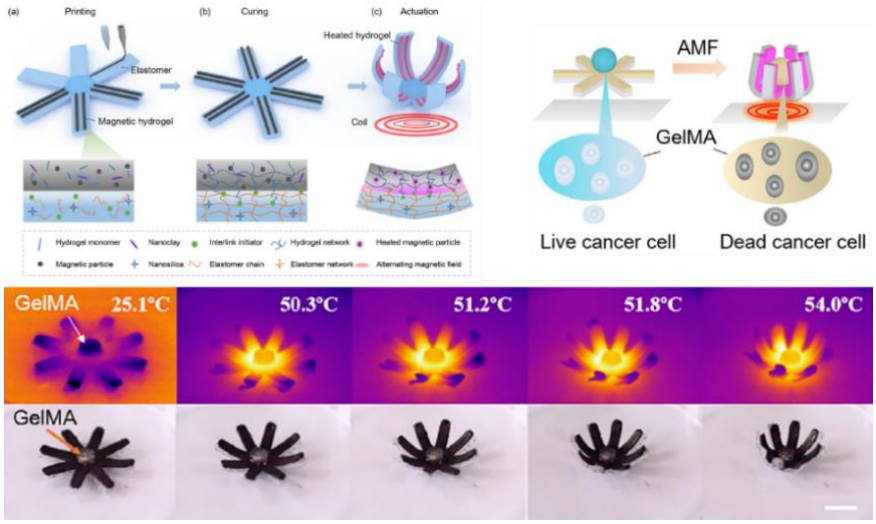

Figure 2.11 The schematic overview of printing and deformation of the composite structure of magnetic hydrogel and elastomer for magnetic hyperthermia (above) and infrared images of the eight-arm structure illustrate the thermal behavior of the structure when subjected to a magnetic field over time (bottom) (adapted from [30]).

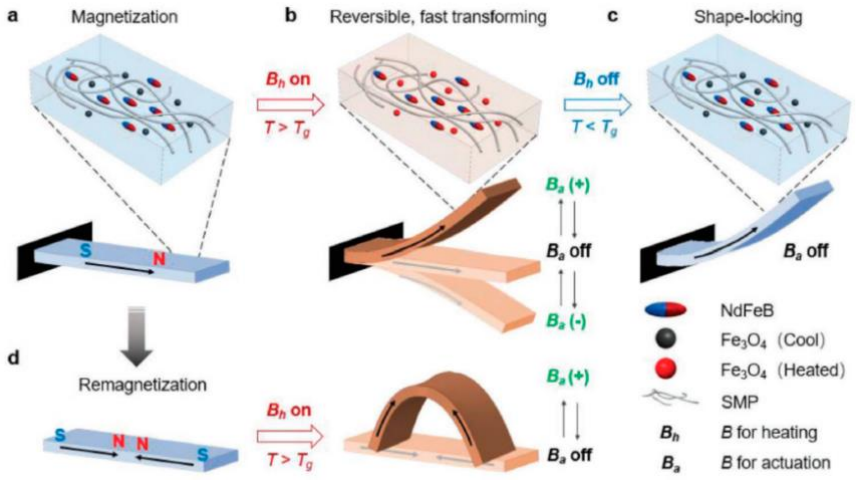

Figure 2.12 The mechanism of magnetic shape memory polymer (M-SMPs) (copied from [34]).

2.1.5. Synthesis of Magnetic Particles

The shape and size of magnetic particles play an important role in determining their magnetic properties [35]. The saturation magnetization (M_s) increases with particle size because the surface effect diminishes, reducing the difference between the spins on the surface and those in the bulk [36]. Different synthetic methods are used to obtain magnetic particles of desired size, ranging from macro- to nano- scale. The magnetic particles can be synthesized based on three different routes, including chemical synthesis, physical synthesis, and biological synthesis, respectively [37]. In physical methods, there are mainly two approaches, which are bottom-up approach and top-down approach. As shown in **Figure 2.13**, the top-down approach begins with bulk materials at the macroscopic scale and then reduces them to the desired particle size through grinding. The top-down approach is more suitable for creating thin films and nanomaterials that are greater than 100 nm in size [38]. Examples of the top-down approach include ball milling, thermal evaporation, and etching techniques. Conversely, the bottom-up approach fabricates

particles at the atomic level and then integrates into the desired size. This process uses chemical or physical forces to assemble individual molecules into larger structures using noncovalent bonds like hydrogen bonds, ionic bonds, and van der Waals forces. The techniques for bottom-up approach include spray and freeze drying, laser evaporation, and sol-gel process. This method results in well-dispersed, fine nano-scaled particles that are smaller than those produced by the top-down approach. In this review, the physical methods (i.e., ball milling) will be the main focus.

One of the commonly used physical approaches is ball milling. It is a synthesis technique used to generate nanoparticles of metal materials with various shapes and dimensions. The planetary ball mill is a commonly used system for mechanical alloying, especially suitable for laboratory research since only a small portion of powder is required. The High-energy ball milling (HEBM) process begins by placing a powder mixture inside the ball milling jar, where it is subjected to high-energy collisions from the balls within the jar. These moving balls transfer their kinetic energy to the milled compound, resulting in the rupture of chemical bonds and a decrease in size with newly formed surfaces [39]. To achieve the desired particle size range, several parameters must be considered, including milling media, milling speed, ball-to-powder weight ratio, as well as milling duration. These parameters regulate the energy transfer between the balls and the material during the process, influencing the physical and morphological properties of the resulting nanomaterials.

In general, there are two primary approaches to ball milling: dry milling and wet milling. In dry milling, no solutions or surfactants are added; only the raw materials and milling balls are present in the milling jars. However, the particle size of magnetic materials prepared using this approach can be limited to the micrometer range due to the cold-welding effect [40], where particles tend to stick together, forming larger aggregates. To address these issues, wet milling is proposed, where surfactants are added during the milling process. Surfactant molecules adsorbed on the fresh surfaces of the generated particles help lower their surface energy by creating an organic layer, thereby preventing aggregation. In addition, surfactant is used to protect the crystal structure of the magnetic phase and reduce particle oxidation during and after ball milling [41]. It also acts as lubricants, preventing the re-welding of crushed particles and facilitating the dispersion of nano/microparticles during milling. Nguyen reported regarding the utilization of oleic acid ($C_{18}H_{34}O_2$) as a surfactant in the synthesis of the $(Fe,Mn)_2(P,Si)$ ferromagnetic particles during ball milling [24]. The concentration of the surfactant ranged from 0 to 30% of the weight of the powder, while the amount of solvent remained constant at 60% of the powder weight. It was discovered that the concentration of surfactant had no significant impact on the structural and magnetic characteristics of the particles.

Figure 2.14a illustrates the ball-milling system, which comprises a single-turn disc (turn table) and four jars. **Figure 2.14b** shows the motions of the balls and the powders. The jar and turn disk rotate in opposite directions, resulting in alternating synchronization of centrifugal forces. The grinding balls and material inside the jar are subjected to the centrifugal forces generated by the overlapping rotations. The interaction between the balls and jar generates a mix of impact and friction forces that affect the material inside the jar. The interaction between these forces is accountable for the reduction of particle size and the simultaneous generation of macrostrains within them. Changes in the size and the surface morphology of synthesized magnetic particles are commonly determined via techniques, such as transmission electron microscopy (TEM) and scanning electron microscopy (SEM).

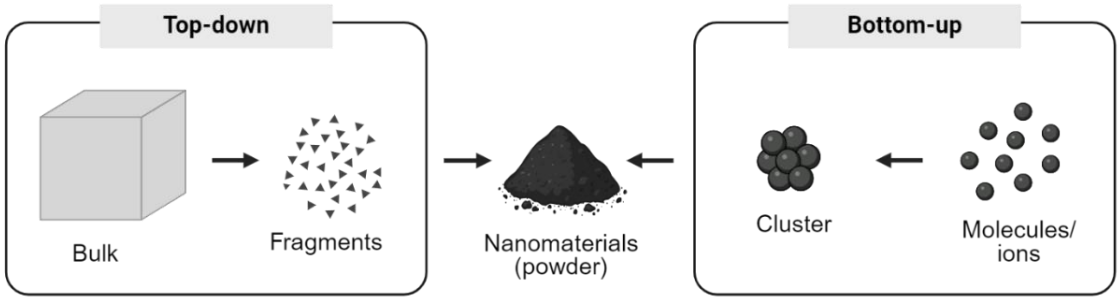

Figure 2.13 A schematic representation of top-down and bottom-up approaches for magnetic materials fabrication (created with BioRender).

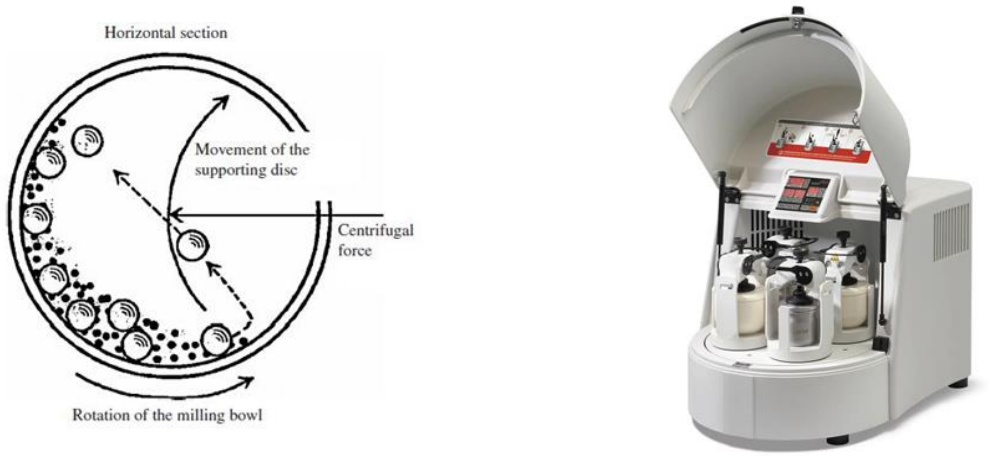

Figure 2.14 a) A schematic diagram of the ball milling process and **b)** an example of the planetary mill machine (copied from [42] and [43]).

2.2. Vascularized Organoid-on-chip Platform

Organoids are complex 3D cell structures that can self-organize and mimic the functions and physiological characteristics of organs found in living organisms. In contrast to conventional spheroids, organoids exhibit greater tissue complexity, enabling more detailed investigation into tissue-specific functions, as shown in **Figure 2.15**. Moreover, due to their inherent ability to differentiate and self-organize, they serve as essential tools in studying genetic disorders and diseases, drug screening, and also personalized medicine [44].

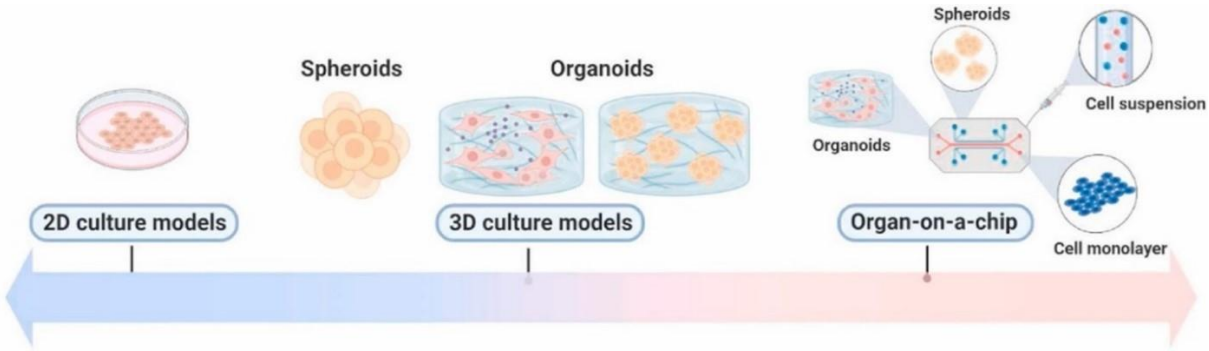

Figure 2.15 An illustration of the evolution of in vitro study technologies, from 2D conventional culture models to organ-on-chip (OoC) platforms (copied from [45]).

Current organoids are still facing limitations, especially their inability to respond to mechanobiological stimuli such as flow, shear stress, and cyclic strain, which play important roles in promoting vascular network perfusion and production [46]. This hinders their comparability to living organ systems. Typically, organoids ranging in diameter from 50 to 1000 μm depend on passive diffusion for the exchange of nutrients, oxygen, and metabolic waste [47]. However, as these organoids continuously grow larger, diffusive transport becomes insufficient to meet their escalating metabolic demands, eventually impeding their growth and development. Regarding biological systems, cells positioned more than 200 μm away from a blood vessel struggle to survive due to the limited diffusion of oxygen and nutrients [48].

Incorporating vascular networks into organoids shows promise for enhancing their lifespan and enabling them to progress beyond the embryonic stage. To address this limitation, organ-on-chip (OoC) technology offers a promising solution for generating these vascular networks. It is a microfluidic device designed to

mimic the microenvironment and physiological functions of specific organs in vitro. OoC typically consists of multi-channels where cells can be cultured under controlled conditions, allowing researchers to study organ-level responses to various stimuli, drugs, or diseases in a more physiologically relevant context. With this in mind, it can offer an environment where in vitro vascular networks can be constructed. Moreover, the microfluidic flow generated within the channels facilitates the timely replenishment of nutrients and removal of waste, thereby fostering favorable conditions for cell viability during long-term culture.

Self-organizing vascular networks represent one of the available microfabrication techniques for cultivating in vitro vascularization on OoC platforms. This approach can be broadly categorized into two main models: vasculogenesis and angiogenesis [47]. Vasculogenesis in vivo is the process by which new blood vessels are formed during embryonic development, beginning with the differentiation of mesodermal cells into angioblasts, and it is responsible for the basic formation of a vascular network. For in vitro vasculogenesis models, endothelial cells (ECs) are initially seeded within a hydrogel, and once they self-assemble into a vascular bed, the organoid is placed onto the chip, as demonstrated in **Figure 2.16a**. On the other hand, angiogenesis produces the vascular sprouts from existing vessels. According to the in vitro model of angiogenesis, EC monolayers are usually seeded onto the surface of a microfluidic platform with a centrally located organoid. ECs are seeded into the medium channels on both sides of the hydrogel, enabling them to adhere to the hydrogel interface and form a pre-existing blood vessel, as shown in **Figure 2.16b**. Subsequently, it can be either the organoids are placed onto the central hydrogel once the vascular bed is differentiated and formed, or the organoids are first seeded into the chip, and ECs are seeded afterward once the organoid is completely differentiated.

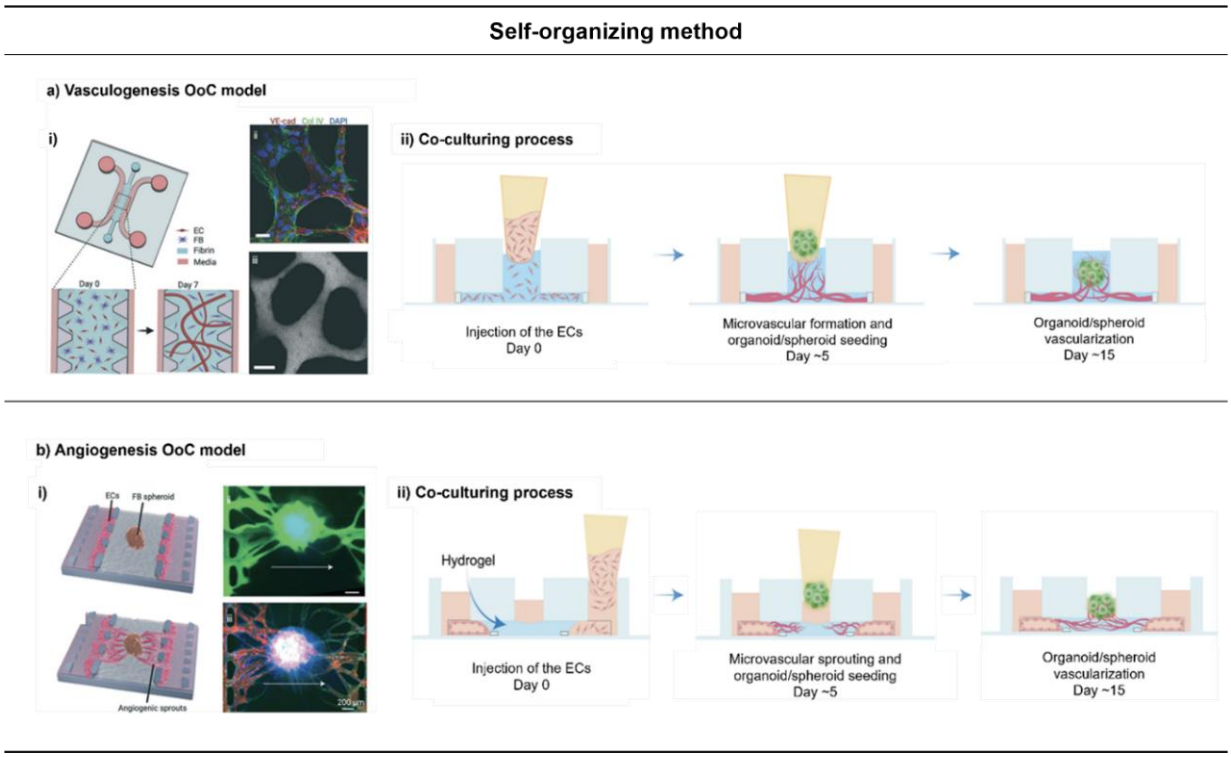

Figure 2.16 An illustration of vasculature formed by self-organization **a)** Vascular bed formed through vasculogenesis and **b)** Vascular bed formed through angiogenesis (adjusted from [44], [47]).

The study reported the development of a 3D-co-culture spheroid model with a perfusable vascular network in a microfluidic chip [48]. This angiogenesis model was constructed using polydimethylsiloxane (PDMS) and fabricated via soft lithography and replica molding **Figure 2.17a**. As can be seen in **Figure 2.17b**, the vascular cells and spheroid were separated using micro posts with a thickness of 100 µm. Before co-culturing the brain organoid and vascular endothelial cells within the microfluidic platform, the organoid was

initially precultured off the chip before being introduced into the designated well located at the center of channel 3. Subsequently, the endothelial cells (i.e., HUVECs) were introduced into channels 2 and 4. Angiogenic sprouts were induced by culturing for 8-19 days after the introduction of the organoid. As a result, 3D-blood vessels efficiently formed and gradually penetrated the core of cerebral organoids (42%).

Another study introduced a 3D printing-based OoC co-culturing platform involving an organoid (i.e., human pluripotent stem cell (hPSC)-derived pericytes), and endothelial cell (EC) sprouts [49]. Similar to the previously mentioned research, the organoid and vascular cells were seeded separately to reach their maturation. The chip design is depicted in **Figure 2.18**. The chip features two cell compartments separated by a wall, with a 50 μm gap at the channel bottom. Before co-seeding two different cell cultures, the organoid was seeded and differentiated off-chip for 5 days, while the vascular cells were seeded and differentiated within the microfluidic channels for 6 days. It has been observed from another report that co-culturing at an earlier stage when the organoid is undifferentiated can disrupt proper organoid development due to the presence of vascular growth factors in the media and paracrine signals from ECs [44]. This indicates that the pre-culturing of the cell cultures with precise timing is crucial to ensure optimal maturation of both cultures before co-seeding. Successful perfusion of fluorescent dextran dye into the core of the spheroid showed a fully perfusable network across the central gel. This paves the way for developing a fully functional vascularized organoid-on-chip with perfusable vascular networks.

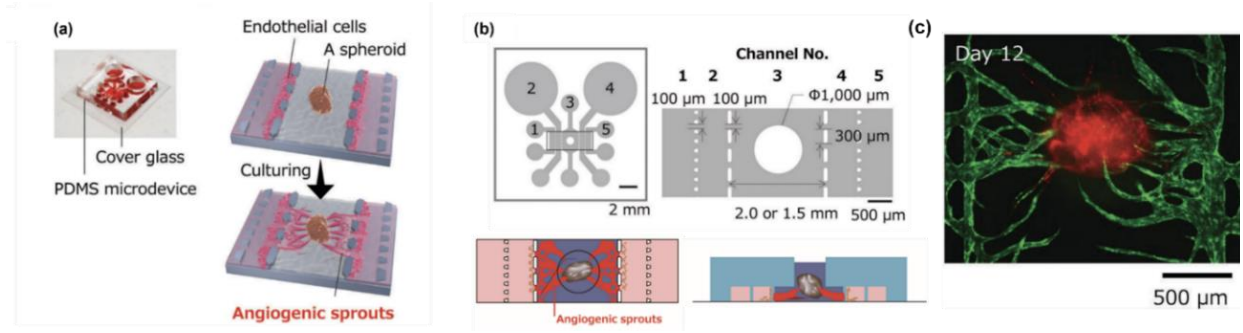

Figure 2.17 A schematic overview of the design of the microfluidic platform for spheroid cultures on chip: **a)** Illustration of a microfluidic device, **b)** Top and side views of the device, and **c)** Sequential images of channel 3. Red represents the spheroid and green denotes HUVECs cultured in microchannels (adjusted from [48]).

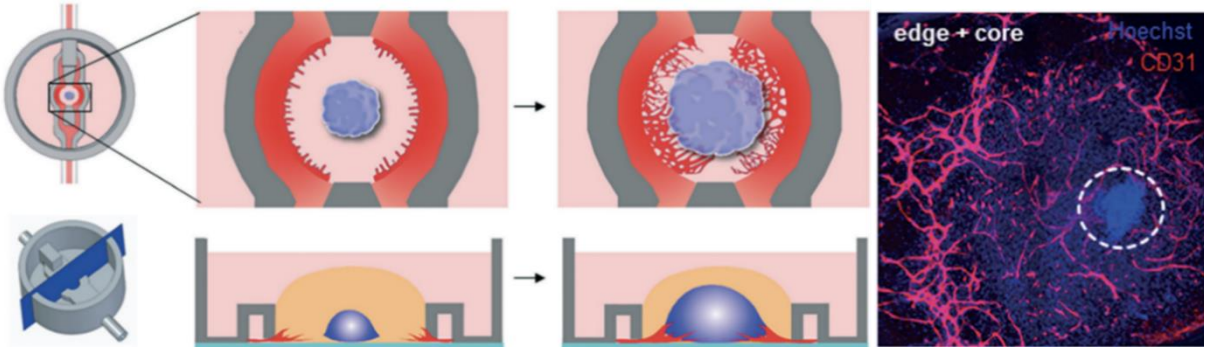

Figure 2.18 A schematic overview of the design of a microfluidic platform for vascularized organoid cultures on chip and schematic representations of on-chip angiogenic sprouting (adjusted from [44]).

As previously discussed, co-culturing the organoid and vascular cells at an early differentiated stage can impede their proper development. Therefore, the precise timing of co-seeding when two distinct cell cultures are sufficiently matured is important. Furthermore, these cell types exhibit considerable fragility. Previous studies have generally cultured organoids and vascular cells separately off-chip until they attain adequate

differentiation. To streamline this process and minimize the potential damage caused by relocating cell cultures, an integrated approach that eliminates the need for off-chip culturing is proposed. One promising strategy involves the development of an organoid-on-chip platform by creating a non-permeable barrier membrane that completely separates both cell cultures. Then, when they are ready for co-culturing, such membranes would be triggered via external activation (e.g., magnetic field, near-infrared light, etc.), resulting in a degradation/opening of the membrane, allowing two different cell cultures to interact and cross-talking. The human body's vascular system is complex and dynamic with various stages. For instance, in vivo angiogenesis, the main mechanism behind vascular sprout formation, involves the degradation of the extracellular matrix (ECM) by specific enzymes, allowing endothelial cells to escape from the parent vessel wall. By integrating the transient membrane, not only the complete separation of the organoid and vascular systems is achieved, but also the membrane's functionality to act as a barrier is leveraged, emulating the functions of the extracellular matrix. To ensure the proper functionality of the transient membrane, the barrier must possess hydrophobic properties to fully separate different cell cultures. Moreover, the membrane must be designed to respond to external activation, enabling it to open and allow interaction between the cell cultures once they reach the desired level of maturation.

With this, the selection of suitable binder materials for encapsulating magnetic particles is also crucial to ensure the stability and functionality of the composite. Natural wax emerges as a promising candidate due to its hydrophobicity and biodegradability. Its hydrophobic properties serve as a non-permeable membrane barrier, preventing water or other substances from passing through. Complex combinations of chemicals, such as fatty acids, anhydrides, long-chain poly- and mono-unsaturated esters, short-chain hydrocarbons, and resins, are commonly found in wax. While increased hydrophobic hydrocarbon content tends to increase hydrophobicity, the inclusion of reactive functional groups like esters, anhydrides, and unsaturated sites is likely to increase the rate of biodegradation of wax materials [50].

2.3. Wax-based Composite

Wax is classified as one of the phase change materials (PCMs), which play a significant role in storing thermal energy for various applications, including thermal energy storage technology, solar applications, and biomaterials in drug delivery systems [51]. Phase change materials involving solid-solid, solid-liquid, solid-gas, and liquid-gas transitions are used to classify PCMs. Because of their low volume fluctuations and high latent heat capacity, solid-liquid PCMs—like wax—are employed extensively [52]. One possibility is that PCMs can absorb heat generated through electrothermal conversion. The process involves the passage of an electric current through a conductive composite. The material absorbs the Joule heat generated by the electric current, storing it as latent heat during its phase transition, thereby converting electrical energy into thermal energy.

In the scope of this master's research, the development of magnetocaloric wax composite for biodegradable membrane serving as a temporary barrier between two cell culture channels is synthesized. The objective of this review of the literature is to evaluate the current advancements in the utilization of wax materials as a binder of electrically conductive particles and to assess their sustainability as transient membranes. This section examines potential wax materials and their fabrication and characterization techniques for examining biodegradable hydrophobic composites composed of wax and functional particles. The current methods for synthesizing and characterizing wax-based composite are mainly reviewed. An overview of composite components, preparation methods, and properties, including conductivity and melting point, is summarized in **Table 2.1**. According to the review articles, it is developed as an electrically conductive composite for biocompatible electronic devices, such as interconnects, conductors, etc., as shown in **Figure 2.19**. Different types of biodegradable wax-based matrices are combined with various types of electrically conductive particles. The particles served as conductive agents, which are in other words used to act as a resistor. Theoretically, when an electric current passes through a resistor, the resistor resists the flow of electricity and converts some of the electrical energy into heat. This process of converting electrical energy to thermal energy is known as Joule heating or resistive heating. The wax can absorb the emitted Joule heat, storing it as latent heat and completing the conversion and storage process from electrical to thermal energy. With this, it has a strong potential to be implemented as Joule heater applications [53].

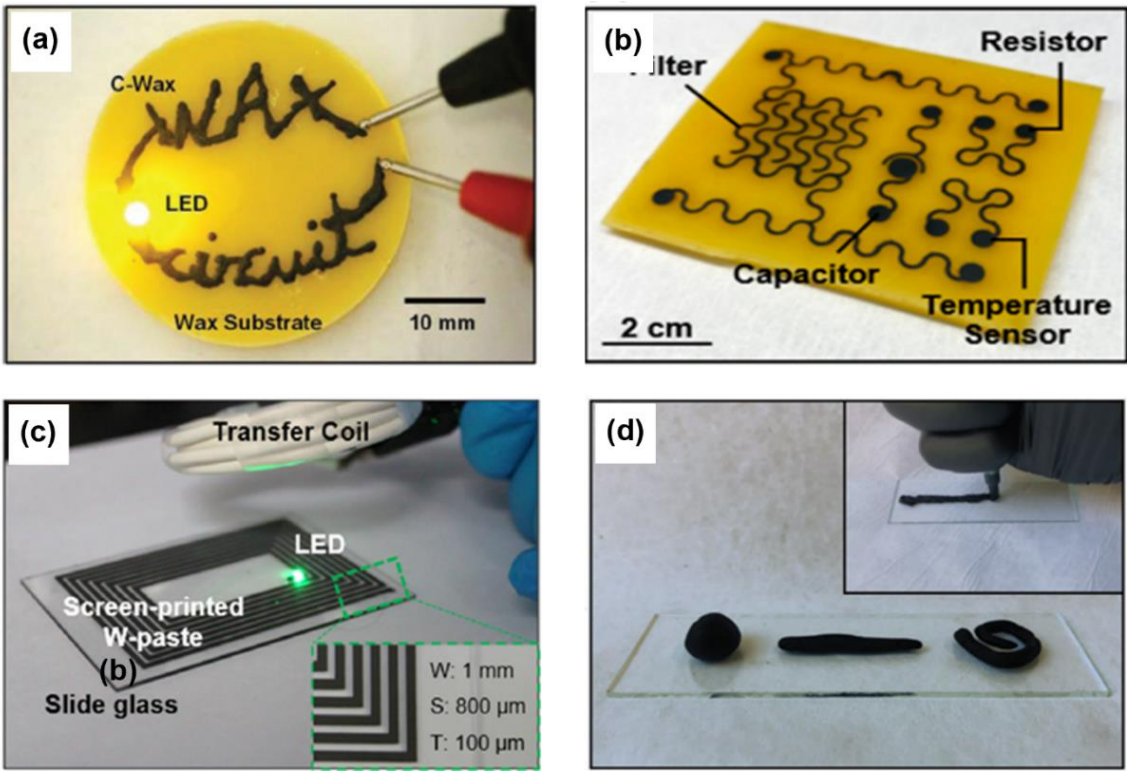

Figure 2.19 Various applications of magnetic wax-based composites reported in the literature: **a)** Candelilla wax composite with W particles used as an electrically conductive paste [50], **b)** Printed electronic components (resistors, capacitors, temperature sensors, and filters) on candelilla wax composite mixed with Mo particles [54], **c)** Printed rectangular W-paste from a beeswax and tungsten composite [55], and **d)** Direct ink writing of edible beeswax paste with activated carbon [56].

Table 2.1 A conclusion table of electrically conductive wax-based composite.

Ref.	Wax composite		Preparation procedures	Conductivity (S/m)	Melting point (°C)
	Type of wax	Conductive agents			
[50]	Candelilla wax	Tungsten (W) (5 µm)	Mechanical mixing of W powders with candelilla wax at 100°C.	3500 (at 35 vol.-% W)	72.3
[54]	Candelilla wax	Molybdenum (Mo) (<5 µm)	Pre-washing Mo particles by ultrasonic and centrifugation, then dried at 70°C. Mechanically mixing with wax at 100 °C and dispersed with ultrasound bath at 80°C.	14000 (at 30 vol.-% Mo)	63-65
		Tungsten (W) (12 µm)		30000 (at 30 vol.-% W)	
[53]	Candelilla wax	Molybdenum (Mo) (25 µm)	Melting candelilla wax at 130°C before mechanical mixing of Mo particles.	130 (at 35 vol.-% Mo)	N.R.
[55]	Beeswax	Tungsten (W) (500 nm)	Mechanical mixing of W particles with beeswax at 100°C. GF was added after the mixture is cooled to 70°C and dispersed with ultrasonication.	6400 (at 27 vol.-% Mo)	65
[56]	Beeswax + Oleogel	Activated carbon (AC) (10-100 µm)	Melting and mixing wax and oil and then adding the desired amount of AC.	1 (at 40 wt.-% AC)	60.8

In summary, the findings from studies focused on biodegradable wax-based composites for biodegradable electrically conductive pastes. It is demonstrated that natural waxes are both biocompatible and biodegradable. Its hydrophobicity allows them to act as effective binders for conductive particles. The articles investigated the performances of the wax-based composite in three critical aspects, including the investigation on the influence of the particle size of the conductive particles on electrical properties, biodegradability, and biocompatibility. The synthesis of wax-based composites typically involves heating the matrix to a liquid state before mechanically mixing in the particles. Some studies have used ultrasonic dispersion to enhance particle homogeneity. The use of vegetable oil, such as sunflower oil (Oleogel), has been shown to ensure adhesion and uniformity between wax matrix and active carbon particles (AC) and minimize micrometric cracks. The tuning of the rheological properties of the sample can be achieved by adjusting the ratio of wax and oil, as shown in SEM images in **Figure 2.20**. Furthermore, adjusting the volume fraction of magnetic microparticles can significantly affect electrical conductivity: higher proportions of magnetic particles result in higher conductivity. However, high-volume fractions can make the composites too dense and sticky, complicating stirring and printing, and leading to cracking. Further investigation showed that conductivity decreases when the particle volume fraction exceeds 30-35% due to diminished polymer quantity and inhomogeneous dispersion. Therefore, an optimal range of particle sizes needs to be determined to balance conductivity. Moreover, the particle size should be small enough, ensuring the particles can degrade or be removed from the body or organ-on-chip (OoC) platform after use.

While certain studies have investigated the melting points of waxes through Differential Scanning Calorimetry (DSC), there remains a gap in understanding the thermal behavior of wax composites, especially the ones with magnetic particles. The core objective behind fabricating wax-based composites in these studies is not to exploit the particles for inducing the melting of the composite. Instead, magnetic particles serve as conductive agents for circuit interconnects and electronic components for bioelectronics rather than heating agents. Consequently, the thermal response of wax composites based on either Joule heating or heating via external stimuli such as infrared light or magnetic fields has not yet been thoroughly investigated, presenting room for further research. Furthermore, while it has been noted in reports that the wax materials employed in these studies possess relatively low melting points, it is crucial to recognize that even these low melting points may still be too high and pose risks to living systems. Additional exploration of other types of wax materials with lower melting points in a therapeutic range is crucial for transient membranes, minimizing the potential for cell damage.

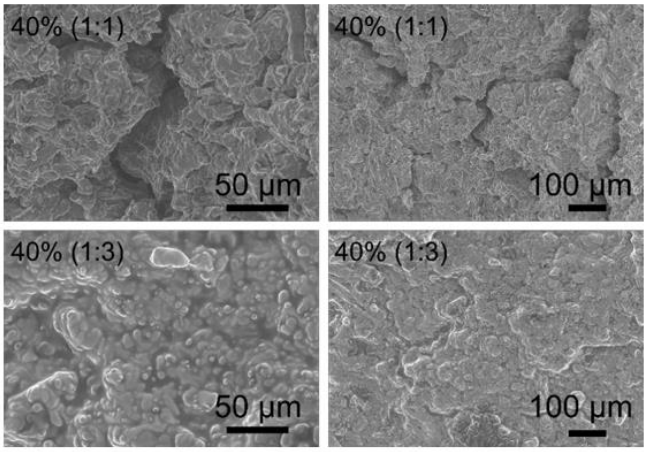

Figure 2.20 SEM of the samples with 40% active carbon (AC) with a matrix made with a wax oil ratio of 1:1 and 1:3 (copied from [56]).

Regarding the degradation assessment of the sample reported in the review studies, it can be observed by monitoring changes in electrical resistance ($\Delta R/R_0$) as a function of time, surface morphology via scanning electron microscopy (SEM), weight changes, and water uptake. The changes in electrical resistance as a function of time were used to track the degradation of composite sample and monitored under phosphate-buffered saline (PBS pH 7.4 at 37°C) [54]. In the study conducted by Won et al. [50], in vitro degradation of

the wax sample is monitored under PBS at both room temperature and 37°C. The resistance tends to increase over time when the sample is immersed in PBS solution, indicating that the sample started to disintegrate and dissolve due to the hydrolysis reaction. The water can penetrate through the wax matrix, lowering the material's performance to conduct electricity, which leads to an increase in resistance. SEM analysis was used to detect microcracks and assess the rheology of the fabricated wax sample at different dissolution stages when immersed in the PBS solution indicating water penetration at different stages. It is reported from the literature that the degradation of candelilla wax composites begins with the hydrolysis of ester and anhydride groups. Moreover, in addition to tracking changes in resistance and SEM images, the degree of hydrophobicity was determined by measuring water uptake and their weight loss. These were observed based on variations in water absorption per sample area (mg/cm^2) over a period time. Initially, the sample weight was recorded, and they were then immersed in deionized (DI) water at 37°C. At various intervals, the samples were removed from the water, weighed to determine the amount of water absorbed, and then returned back to the water.

Biocompatibility of the wax paste was evaluated through cell viability and in vivo biocompatibility tests in the study of Kim et al [55]. They reported using in vitro live/dead and WST1 cytotoxicity kits to evaluate cell viability. In vivo biocompatibility was examined using male mice (6 weeks old) to ensure the safety of the wax sample for bioelectronic device applications. A wax-paste sample measuring 5 mm x 5 mm with a thickness of 100 µm was implanted subcutaneously in the dorsal tissue of the mice for four weeks. Following the implantation period, blood samples were collected from the mice for a complete blood count test, measuring white blood cells (WBCs), neutrophils, lymphocytes, and monocytes to evaluate inflammation. Results showed that the proportion of living cells in all test groups over seven days was comparable to that of the control groups (PLGA and PDMS), indicating negligible cytotoxicity of the wax-paste sample. In vitro cell viability, measured by the WST1 assay, also revealed that mouse fibroblast viability remained above 90% for the wax paste sample compared to control groups. Additionally, the in vivo biocompatibility test, based on blood and tissue analyses, confirmed that the wax paste samples induced a minimal inflammatory response. Moreover, there was no significant inflammation observed in the mice, as evidenced by the thinnest fibrotic tissue among the control groups, indicating negligible chronic inflammation. These findings concluded that the wax paste is biocompatible for potential use in the human body. However, further studies involving human cells are necessary to conclusively determine their biocompatibility with human tissues.

2.4. Concluding Remarks on Literature Study

The insights obtained from the review, involving the theoretical knowledge of magnetic materials, the heat generation mechanisms of magnetic particles, as well as the example of applications regarding the utilization of magnetic particles as heating agents are explored. Subsequently, the vascularized organoid-on-chip platform and the review of the current advancements of fabrication and characterization of wax composite are explained. These have established the foundation for the research scope of this master's thesis. Certain magnetocaloric compounds, specifically $(Mn,Fe)_2(P,Si)$ has been introduced, highlighting its potential use as magnetic heating agents for biodegradable membranes due to their distinctive non-toxicity and critical temperature (T_c) tunability characteristics. Regarding the literature search, there have been several studies reporting the potential use of $(Mn,Fe)_2(P,Si)$-based compounds in biomedical applications, but there has not been any research regarding its specific fabrication for the use in medical applications. Therefore, it still leaves room for further investigation to specifically explore wax-based composite using magnetocaloric materials for the OoC platform.

2.5. Research Question

This research project is mainly focused on the fabrication and development of magnetocaloric wax composite for biodegradable membranes. The central research question of the master's thesis is:

"How can a magnetocaloric wax composite be fabricated for a biodegradable membrane to facilitate the temporary separation of organoids and perfusable vascular networks in a microfluidic platform?"

The research project is structured into two primary sections:

(1) Fabrication and Characterization of Magnetocaloric Material.

The $(Mn,Fe)_2(P,Si)$-based compound is investigated regarding its potential to be used as heating agent for biodegradable membranes. The $(Mn,Fe)_2(P,Si)$ particles synthesized in this master's project should meet the following requirements:

- The magnetocaloric particles should exhibit a distinct transition point (T_c) at approximately 43-44°C.
- The magnetocaloric particles should achieve a particle size in the range of 1-10 µm.

(2) The fabrication and characterization of a magnetocaloric wax-based composite.

The synthesized composite should meet the following requirements:

- The wax matrix should exhibit a melting point within the therapeutic range and below the T_c.
- The magnetocaloric wax composite should efficiently melt under an applied magnetic field.
- The composite must be biocompatible and biodegradable.

2.6. Research Scope

Part 1: Synthesis of Magnetocaloric Particles

The initial phase of the project involves synthesizing magnetocaloric particles. The $(Mn, Fe)_2(P, Si)$-based compound will be developed to exhibit the desired critical temperature (T_c) and appropriate particle size for compatibility with living cell cultures. Several fabrication techniques will be employed, including the ball milling process, melting spinning technique, and heat treatment. These methods will be used to fine-tune the magnetocaloric particles to meet the specified requirements. Following the synthesis, the particles will be characterized in terms of magnetization properties, structural analysis, and thermal properties.

Part 2: Development of Magnetocaloric Wax-Based Composite

The second phase focuses on developing a suitable wax matrix. The literature review indicated that common waxes like candelilla wax and beeswax have melting points higher than the therapeutic range (higher than 47°C). Therefore, identifying and synthesizing a proper wax material with an appropriate melting point is crucial for transient membranes. Once an appropriate wax material is selected, the magnetocaloric particles will be integrated into the wax matrix through mechanical mixing. The resulting composite will undergo characterization to study its thermal behavior under a magnetic field, using both alternating magnetic fields (AMF) and permanent magnets. The performance of the magnetocaloric wax composite will be compared against composites mixed with commercial magnetic particles such as carbonyl-iron and iron-oxide particles.

Part 3: Biocompatibility and Biodegradability Assessment

The final focus will be on evaluating the biocompatibility and biodegradability of the composite. Although the $(Mn, Fe)_2(P, Si)$-based compound has been reported as non-toxic in the literature, there is a lack of biocompatibility tests. Therefore, it is essential to assess its biocompatibility to ensure its suitability for use in transient membranes that separate cell cultures. Additionally, biodegradability tests will be conducted to determine the degradation behavior of the composite over time.

3

Materials and Experimental Methods

This section outlines the materials selected for the study, detailing both the magnetocaloric compound's composition and the wax-based components used. Initially, the synthesis and characterization techniques for optimizing magnetocaloric particles are described. Next, the process for fabricating and characterizing the wax matrix is explained. After characterizing the magnetocaloric materials and wax matrix, the methods for synthesizing the magnetocaloric wax-based composite for a biodegradable membrane are outlined. The section then discusses the characterization procedures and testing experiments, concluding with an explanation of the biocompatibility tests.

3.1. Part 1: Synthesis of Magnetocaloric Materials (MCM)

Magnetocaloric particles were prepared and subjected to characterization. The preparation involved the utilization of various syntheses, including high-energy ball milling, melt spinning, and heat treatment. Different characterization techniques were employed to evaluate the sample's structure as well as its magnetic and thermal properties. A schematic overview of the synthesis methods applied throughout the project is demonstrated in **Figure 3.1**.

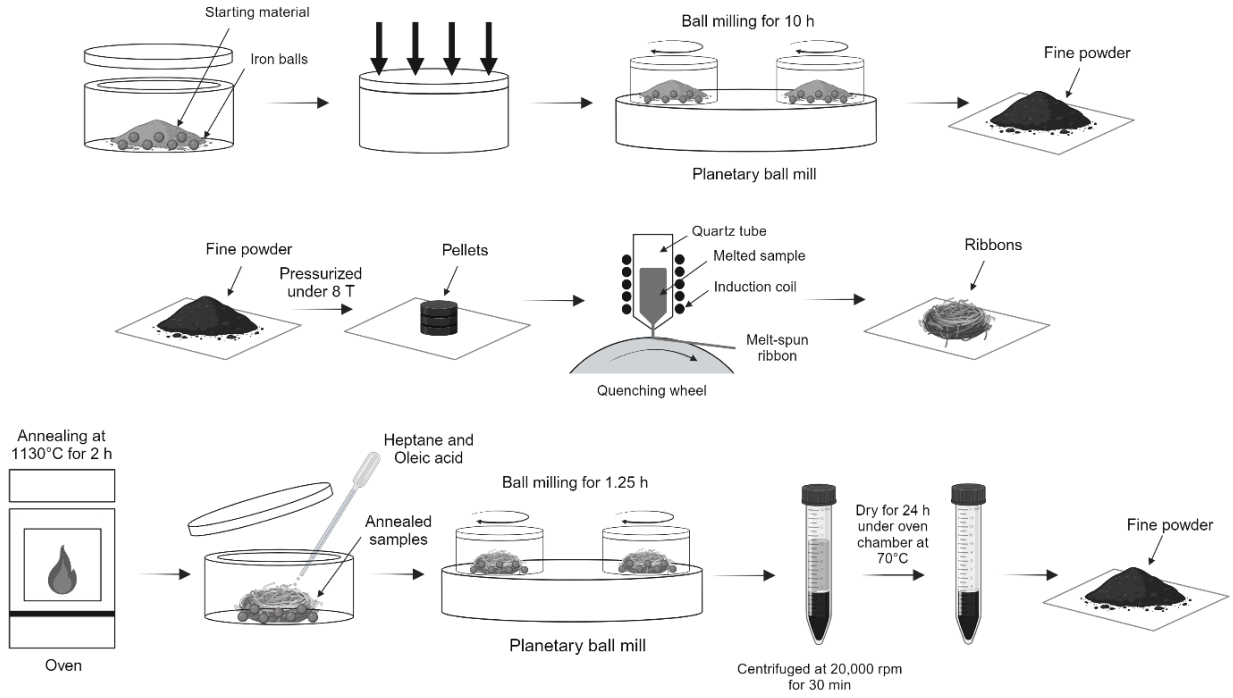

Figure 3.1 A schematic overview of the fabrication process of $Mn_{0.65}Fe_{1.30}P_{0.65}Si_{0.37}$ samples.

Choice of Magnetocaloric Materials

The $(Mn,Fe)_2(P,Si)$-based compound was selected for fabrication in this master's project. This compound exhibits a first-order sharp phase transition. It has gained significant attention due to its remarkable giant magnetocaloric effect (GMCE) near room temperature with a small applied magnetic field, cost-effectiveness, and lack of toxic elements [24], [25], [26]. Notably, it exhibits tunability of the Curie temperature over a broad range, which is crucial for precise temperature control to prevent overheating that may cause severe damage to living cells. Although its Curie temperature can be easily tuned by adjusting the composition of the material, the remaining drawbacks of such material are the brittleness and the relatively low thermal conductivity [26].

From a fundamental perspective of crystal structure, $(Mn,Fe)_2(P,Si)$ alloys exhibit four potential lattice structures. One of these is a single hexagonal structure of Fe_2P-type, with a space group of P-62m. This structure contains two metallic sites (3f and 3g) and two non-metallic sites (2c and 1b). The hexagonal unit cell of the $(Mn, Fe)_2(P, Si)$ compound is depicted in **Figure 3.2**. Mn atoms preferentially occupy the 3g site, forming a square pyramid with five non-metals as nearest neighbors, while Fe atoms occupy the 3f site, surrounded by four non-metal atoms forming a tetrahedron. P/Si atoms are randomly distributed on the 1b or 2c sites.

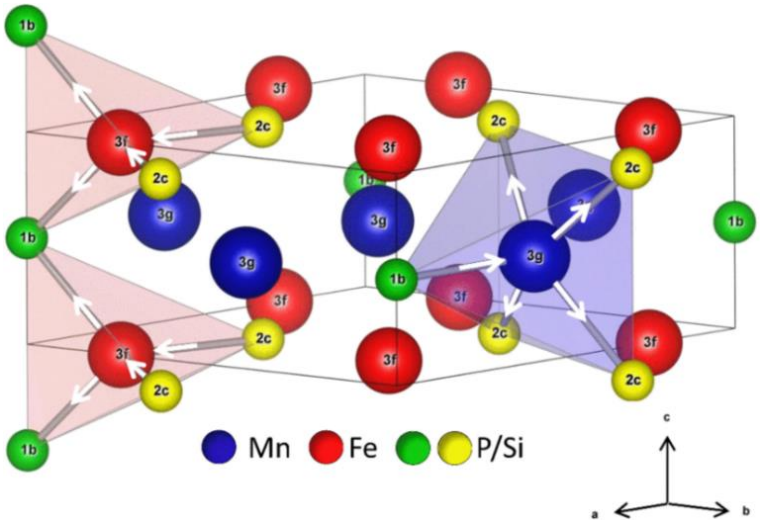

Figure 3.2 A schematic diagram of the crystal structure for the $(Mn,Fe)_2(P,Si)$-based compound [57].

Phase Diagram of $Mn_xFe_{2-x}P_{1-y}Si_y$ System

Regarding the lattice structure of the $Mn_xFe_{2-x}P_{1-y}Si_y$ compound, to maintain a hexagonal Fe_2P-type structure as the main phase, it requires limiting the Si concentration to the range of $0.24 \leq y \leq 0.5$ [25]. This restriction is critical to prevent the formation of impurity phases, which could reduce the phase fraction of the main phase and lead to sample instability. Potential impurity phases include Fe_3Si and Mn_5Si_3. The selection of suitable starting material compositions to achieve the desired Curie temperature (T_c) was based on the phase diagram of the $Mn_xFe_{2-x}P_{1-y}Si_y$ system developed by X. You et al., as shown in **Figure 3.3**. The phase diagram illustrates the composition dependence of the Curie temperature T_c (K) for $Mn_xFe_{2-x}P_{1-y}Si_y$ compound. Additionally, it has been reported that increasing the Mn:Fe and P:Si ratios lead to a decrease in T_c [25]. According to the phase diagram, the Si composition (y) in the range of 0.33 to 0.6 was chosen to synthesize $Mn_xFe_{2-x}P_{1-y}Si_y$ samples with a hexagonal Fe_2P-type lattice structure. The $Mn_{0.65}Fe_{1.30}Si_{0.37}P_{0.65}$ compound was primarily chosen for this project to achieve the desired Curie temperature of approximately 317 K (~43°C).

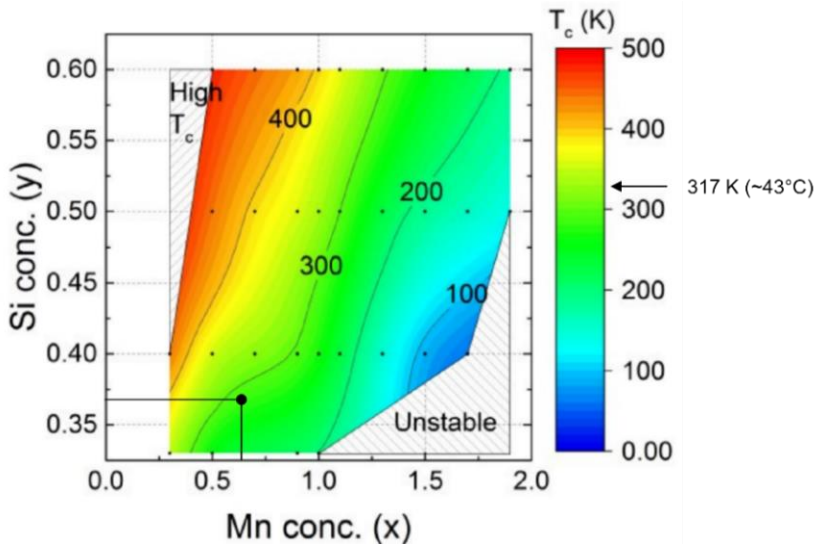

Figure 3.3 The phase diagram of the $Mn_xFe_{2-x}P_{1-y}Si_y$ system shows the composition dependence of the ferromagnetic transition temperature (T_c) (copied from [25]).

3.1.1. Fabrication Methods of Magnetocaloric Compound

The most commonly used methods in this project and also for lab-scale alloy synthesis are ball milling, melt spinning, and heat treatment.

3.1.1.1. High-energy Ball Milling

Within the scope of the investigation, once the appropriate chemical composition of the $(Fe,Mn)_2(P,Si)$ sample was established, each component of the beginning materials, including Mn (99.7%), Fe (99.8%), Fe_2P, and Si (99.6%), were weighed and combined in the ball-milling jars. The number of milling balls varies directly with the quantity of 10 g of sample when 7 milling balls are used, as represented in **Table 3.1**. Consequently, a quantity of 25 grams of initial substances was placed into each ball-milling container, along with the inclusion of 17 iron balls.

Amount of sample per milling jar (g)	The number of milling balls per jar
10	7
25	17
5	4

Table 3.1 A summary of the amount of sample per milling jar and the number of milling balls per jar.

Afterward, the samples and milling balls were enclosed in the grinding jar and sealed in an argon (Ar) atmosphere to avoid surface oxidation during the production process and prevent any moisture or oxygen from entering. The ball-milling process was then set for a duration of 10 h at a constant rotation speed of 380 rpm. The sample obtained after the milling process is represented in **Figure 3.4a**. As a result, the number of particles obtained after the process of high-energy ball milling for 10 h is approximately 8.85 g. Following this, the fine powder obtained was compacted into small tablets using a hydraulic press, exerting a pressure of 8 tons, for future utilization in melt spinning (**Figure 3.4b**).

After the heat treatment, a subsequent round of ball milling is conducted to achieve the appropriate particle size within the specified range. Again, the number of ball milling varies proportionally with the quantity of 10 g of sample, while using 7 milling balls. Each jar was given around 5 grams of the chemical, along with

30% by weight of oleic acid and 60% by weight of heptane. Finally, the jars were thereafter enclosed under argon gas. Furthermore, these jars were subjected to milling for a duration of 1.25 h at a consistent rotational speed of 380 rpm. After milling, the slurry mixture was then dispersed into heptane solvent by ultrasonic vibration and transferred to centrifugal tubes to remove excess surfactant and dried in a vacuum oven at 70°C before they were ready to be analyzed. **Figure 3.4c** depicts a sample including the solvent and surfactant that were collected following the second ball milling process.

(a) **(b)** **(c)**

Figure 3.4 The samples obtained from fabrication process **a)** fine powder after the process of the 1st ball milling, **b)** pellets, and **c)** slurry mixture obtained from the 2nd ball milling.

3.1.1.2. Melt Spinning

Melt spinning is a rapid solidification technique used to produce alloys in the form of strips (ribbons). As illustrated in **Figure 3.4b**, the pellet-like samples produced after the first ball-milling process are inserted into a quartz tube, which is positioned above a copper wheel inside a chamber. The process initiates as the induction coils heat the sample, causing it to completely melt. As shown in **Figure 3.5**, once the entire pellets are in the molten state, gas pressure then propels the liquid metal through a small nozzle of the crucible onto a rotating copper wheel. The copper wheel is maintained at a low temperature, which rapidly cools down the molten pellets, forming them into solid ribbons. **Figure 3.6** depicts the ribbon samples acquired by the technique of melt spinning.

Figure 3.5 A schematic diagram of the melt spinning method.

This method is essential for eliminating oxide impurities within the compound, ensuring cleanliness to be able to be implemented in medical applications, and also resulting in a higher purity of the obtained compound [58]. Due to the rapid solidification at a high cooling rate (up to 10^{-6} K/s), such ultrafast cooling

suppresses the growth of oxide phases. Moreover, the melt spinning process is typically carried under an inert gas atmosphere (e.g., helium or argon) or vacuum. The inert gas environment prevents oxidation of the molten material before it solidifies. The rapid solidification upon contact with the cooled wheel surface "freezes" the atomic structure, inhibiting the formation of crystalline oxides. Moreover, it is reported that the melt spinning process before heat treatment reduces the annealing duration [59], [60]. Additionally, the melt-spinning process produces a homogeneous microstructure in the horizontal direction and therefore improved functional properties [61].

Figure 3.6 Some solid ribbons of $Mn_{0.65}Fe_{1.30}Si_{0.37}P_{0.65}$ compound.

3.1.1.3. Heat Treatment

It is reported that $(Mn,Fe)_2(P,Si)$-based materials are usually prepared by the double solid-state sintering, which takes about three days to achieve a homogeneous composition and consumes a lot of energy [60]. A heat treatment process (annealing) is employed on the sample obtained from the melt-spinning procedure to ensure the homogeneity of the sample and eliminate the formation of the impurity phase. Moreover, the magnetocaloric response of the $(Mn,Fe)_2(P,Si)$ system is particularly sensitive to the synthesis method, especially the heat treatment process [59]. The impact of the annealing temperature and the optimal duration for annealing were observed by Kiecana et al. in the $(Mn,Fe)_2(P,Si)$ compound. Samples were annealed for 2 h at different temperatures: 1313 K (1040°C), 1373 K (1100°C), and 1433 K (1160°C). Results showed a slight decrease in the $(Mn,Fe)_3Si$ impurity phase with increasing annealing temperatures, possibly due to grain growth and a reduction in grain boundaries. Another study identified 1373 K as the optimal annealing temperature for melt-spun ribbons [60]. In this study, the samples are carefully sealed in quartz ampoules within an argon atmosphere. The sample is annealed at 1100°C for a duration of 2 h. The oven is preheated to the desired temperature before the quartz ampoules are inserted for sintering. Once the oven reaches 1100°C, the quartz tube containing the samples is placed directly inside. At the end of the annealing process, the quartz tube is quickly quenched in water at room temperature. The annealed sample is depicted in **Figure 3.7**.

Figure 3.7 Samples obtained after the annealing process (left) the sample inside and (right) outside the quartz tube.

3.1.2. Characterization Methods of Magnetocaloric Compound

In this project, different fabrication techniques were employed to synthesize samples. This section provides a broad overview of how each technique functions and subsequently outlines its specific application and setup within the context of this project.

3.1.2.1. Structural Analysis

3.1.2.1.1. X-ray Powder Diffraction (XRD)

X-ray diffraction (XRD) serves as a standard experimental technique for the characterization of a material's crystal structure. It is used to identify phases and their fractions, lattice parameters, and atom occupancies which can be derived by refining the measurement patterns with a crystal lattice model. The XRD process begins with a collimated monochromatic X-ray beam directly introduced onto the sample, leading to diffraction, as illustrated in **Figure 3.8**. The angle at which occurs, known as the diffraction angle (θ), can be used to calculate the difference between atomic planes (d) using Bragg's law, as depicted in **Eq. 3.1**.

$$N\lambda = 2d\sin(\theta) \quad \textbf{(Eq. 3.1)}$$

According to the formula, *λ* denotes the wavelength of the incident X-ray, *d* signifies the distance between atomic planes, *θ* represents the diffraction angle, and *N* is an integer known as the order of diffraction peak. This spacing between atomic planes can be utilized to determine a sample's composition and crystalline structure

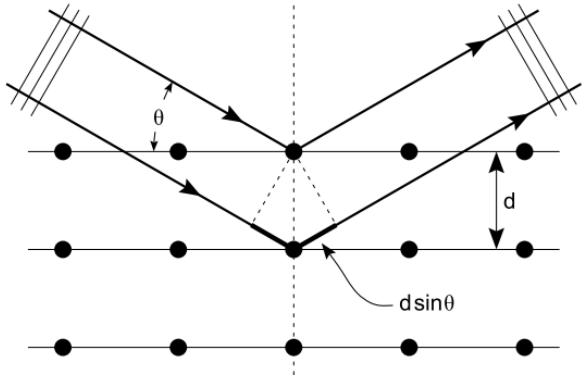

Figure 3.8 A schematic diagram of an X-ray diffraction system.

In this work, the XRD data are acquired with a PANalytical X-Pert Pro using diffractometer with Cu - K_α radiation (λ = 1.54 Å) and an Anton Paar TTK 450 temperature chamber at 80°C. The XRD patterns were recorded within a 2θ range spanning from 20° to 90°. Using the Rietveld refinement technique used with the Fullprof program, an analysis of all acquired XRD data was done in order to determine the crystal structure. The average crystallite size of ball-milled samples is estimated based on Sherrer equation (**Eq. 3.2**), where D_{hkl} is the average crystallite size, hkl are Miller indices of the crystal planes, K is the crystallite-shape factor (0.9), λ is the wavelength of the X-ray (0.154 nm for Cu-Kα radiation), B_{hkl} is the full-width at half-maximum (FWHM) of the diffraction peak in radians and θ is the Bragg angle.

$$D_{hkl} = \frac{K\lambda}{B_{hkl}\cos(\theta)} \quad \textbf{(Eq. 3.2)}$$

Moreover, before calculating the crystallite size using the Scherrer equation, the full width at half-maximum (FWHM) was determined based on **Eq. 3.3**. U, V, and W parameters of the magnetic compound can be determined based on the Rietveld refinement of the XRD data. The FWHM value used in the Scherrer equation is obtained by subtracting the FWHM of the instrument from that of the compound.

$$FWHM^2 = Utan^2\theta + Vtan\theta + W \quad \textbf{(Eq. 3.3)}$$

3.1.2.1.2. Scanning Electron Microscope (SEM)

The microstructure analysis of $(Mn,Fe)_2(P,Si)$-compound, with a focus on particle size, was conducted using a scanning electron microscope (SEM). Electron microscopes use a beam of electrons instead of light to create images, resulting in much higher resolution and magnifications of up to 2 million times [24]. For this project, the particle size and morphology of the $(Mn,Fe)_2(P,Si)$ particles were investigated using a JSM-IT100 scanning electron microscope. SEM images were captured at multiple locations for each sample. **Figure 3.9** shows the SEM machine utilized in this project.

Figure 3.9 Scanning electron microscope (JSM-IT100 model) (copied from [62]).

3.1.2.2. Magnetic Properties

3.1.2.2.1. Superconducting Quantum Interference Device (SQUID)

A superconducting quantum interference device (SQUID) was used to measure the magnetization of magnetic particles. The device is used to measure very small magnetic moments with an extremely high degree of sensitivity. It generates an output voltage that is proportional to a change in the magnetic flux, therefore acting as a flux-to-voltage converter. This is a fundamental idea underlying their remarkable sensitivity as magnetic field sensors.

As shown in **Figure 3.10**, the SQUID sensor is a ring, comprising two superconducting halves separated by two insulating barriers in the middle to create two parallel Josephson junctions. When a constant biasing current is maintained in the SQUID ring, the measured voltage across the SQUID oscillates in response to

phase changes at the two Josephson junctions. These phase changes depend on the change in magnetic flux through the SQUID ring. By counting the oscillations in the measured voltage, the corresponding change in magnetic flux can be evaluated. This makes the SQUID function as an extremely sensitive current-to-voltage converter, where the measured voltage is proportional to the sample magnetization or magnetic field being measured.

In the context of this study, approximately 1-2 mg of powdered sample were enclosed in a gelatin capsule and secured within a plastic straw. Automated positioning of the samples to the SQUID's pickup coil was executed using the reciprocating sample option (RSO), ensuring a positioning distance of 1.5 cm. A SQUID magnetometer is used to determine the magnetization (M) of the sample as a function of temperature (T) and applied magnetic field ($\mu_0 H$). According to the setting sequence in the SQUID measurements, the magnetization as a function of the applied magnetic field (MB-curve) was examined by gradually increasing the magnetic field from 0 to 5 T by keeping the temperature constant at 5 K. Subsequently, the applied magnetic field was kept constant at 0.01 T and 1 T, respectively, to record magnetization as a function of temperature (MT-curve). The magnetic properties of the sample were assessed across temperatures ranging from 5 K to 370 K. The Curie temperatures and the thermal hysteresis were derived from the measurements at 0.01 T. These measurements were performed by using the SQUID model MPMS-XL magnetometer and the data has been visualized and analyzed by using Origin Pro software.

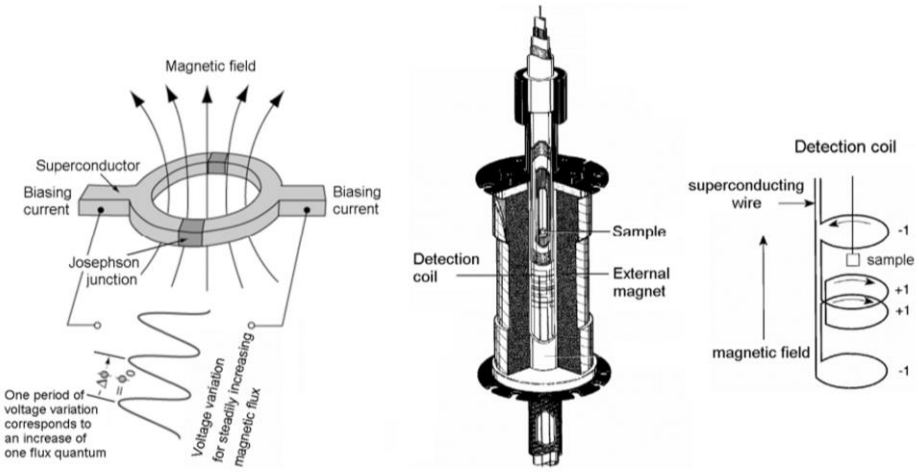

Figure 3.10 Two Josephson contacts forming a SQUID loop [43].

3.2. Part 2: Development of Magnetocaloric Composite

The material used to fabricate the transient membrane is selected based on the criteria of the membrane to ensure its effectiveness. It includes biodegradability, biocompatibility, and hydrophobicity. Biodegradability and biocompatibility are crucial to prevent any adverse effects on cell cultures from either the materials themselves or their by-products. Furthermore, the transient nature of the membrane is required to facilitate interaction between different cell cultures and enable organoid vascularization. Control over the membrane's opening mechanism is achieved through external activation, as in this project, the membrane composite is heated up by using an externally applied magnetic field within a specific period. Additionally, ensuring the hydrophobic nature of the material is also vital for preventing water permeability, preserving media separation, and reducing the likelihood of cell penetration before its appropriate maturation has reached. This composite comprises two primary components: (1) wax matrix which is responsible for the structural integrity of the membrane, and (2) magnetocaloric particles, which serve as the heating agents.

3.2.1. Choice of Composite Material: Wax Matrix

Prior to the introduction of selected wax materials used in this project, in compliance with safety and functionality requirements, the composite materials must possess a melting point within the physiological tolerable range to prevent overheating and consequent damage to cell cultures. According to the literature, the amount of cell death significantly depends on exposure time under a magnetic field and temperature [63]. To establish a maximum permissible temperature and exposure duration, guidelines have been developed, particularly for tissue subjected to magnetic field heating.

The main concept of the guidelines is called Cumulative Equivalent Minutes at 43°C (CEM43), which quantifies thermal stress induced by time-temperature exposure. CEM43 serves as a normalization method to convert diverse time-temperature profiles into an equivalent exposure time at 43°C as given in **Eq. 3.4**, where t_0 signifies the onset beginning and t_{final} denotes the end of the heating period. $T(t)$is the tissue temperature at time t, and R is a constant: 0.5 for $T(t)$> 43°C, 0.25 for 39 < $T(t)$< 43°C, and R is 0 for $T(t)$< 39°C [64]. According to the equation, thermal doses were derived by integrating a temperature-weighed function over time. Notably, sensitive structures like the blood-brain barrier exhibit adverse effects at CEM43 = 2 min [64], which means that at 43°C, tissue can endure exposure for 2 minutes.

$$CEM43\ (t) = \int_{t_0}^{t_{final}} R^{(43-T(t))}\, dt \qquad \textbf{(Eq. 3.4)}$$

According to the wax material selected for this project, lanolin wax and bayberry wax (BBW) are used, as represented in **Figure 3.11**. Their selection was based on their advantageous melting point range, which aligns with the therapeutic temperature range. Lanolin, commonly referred to as wool wax, is a natural wax produced by the sebaceous glands of sheep, imparting waterproofing properties to their coats. Chemically, it is classified as a wax ester which is comprised of lanolin acid (a complex mixture of 170 fatty acids), covalently bound to lanolin alcohol (i.e., sterol) [65]. Its applications span across cosmetics and pharmaceuticals. It has been reported for its properties, including anti-corrosive, non-toxic, biodegradable, and lubricating capabilities [66]. The principal mechanism underlying its degradation involves the hydrolysis of wax ester, resulting in the formation of lanolin alcohols and lanolin fatty acids [67]. Lanolin alcohols extracted through the hydrolysis process are abundant in cholesterol [68], which is normally presented in the cellular membranes and cell structures in the human body. Lanolin fatty acids obtained through hydrolysis can be considered as free fatty acids, which are the important component as energy sources for most body tissues. Therefore, they pose no adverse effects on cell cultures.

In this study, 100% pure lanolin wax purchased from Prounol was utilized. The manufacturer claims that the melting point of the product is approximately 36°C. Although its melting point is slightly lower than the body temperature at 37°C, lanolin wax was selected as one of the wax-based components for experimentation due to its favorable melting point and soft texture.

On the other hand, bayberry wax (BBW), also known as Myrica wax, is primarily composed of glycerolipids, predominantly including triacylglycerols (TAG), esterified exclusively with saturated fatty acids [69]. The saturated nature and elongated hydrocarbon chain of fatty acids contribute significantly to the waxes' high hydrophobicity. While the biodegradation mechanism of bayberry wax remains unexplored, its chemical composition suggests its decomposition via hydrolysis. Hydrolysis reaction breaks down the wax into its original constituent parts, which are glycerol and fatty acids. Glycerol is presented in the human body and is crucial for energy storage and cell membrane structure [70]. On the other hand, similar to lanolin wax, free fatty acids serve as energy sources in the human body. Therefore, they also do not pose any risks to human health and cell cultures.

In this project, commercially available bayberry wax from Natural Heroes was employed as a raw material. Typically, its melting point falls within the range of 39-49°C [71]. Due to its favorable melting point range,

the bayberry wax was combined with lanolin wax to assess its suitability in terms of its melting point as a component in the fabrication of the wax matrix for transient membranes.

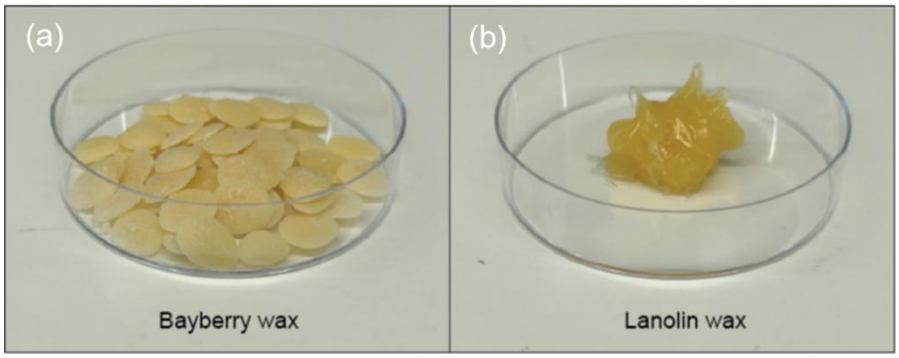

Figure 3.11 Two types of wax materials that were employed in fabricating the transient membrane for this project. **a)** Bayberry wax is presented in the form of solid pellets and **b)** Lanolin wax is characterized by its stickier and softer consistency.

3.2.2. Choice of Composite Material: Magnetic Particles

On the other hand, in this project, the magnetic particles, specifically $(Mn,Fe)_2(P,Si)$-based compound and carbonyl iron powder (CIP), as well as magnetite, iron (II,III) oxide (Fe_3O_4) were chosen to investigate their performances as active/heating agents for transient membranes. This allows for a comparative analysis between the magnetocaloric materials developed in this project and the commercial CIP and iron (II,III) oxide, which are already well-established as magnetic materials in various biomedical applications, especially in hyperthermia treatment. $(Mn,Fe)_2(P,Si)$ magnetocaloric particles were fabricated based on the synthesis procedures mentioned earlier in **Section 3.1**. CIP used in this project was purchased from Sigma-Aldrich with cat.no. 44890 and its particle size is in the range of 1-10 μm. Similar to iron (II,III) oxide (Fe_3O_4), it was also purchased from Sigma-Aldrich with cat.no. 310069 and its particle size is approximately 5 μm.

Carbonyl iron powder (CIP) is renowned for its biocompatibility, making it highly suited for medical purposes. Its widespread commercial use is attributed to its cost-effectiveness, high specific saturated magnetization, and remarkable absorption properties [72]. It has been reported that CIP-filled polymers are commonly used in magneto-hyperthermia for heating treatment of deep-seated tumors due to their exceptional electromagnetic energy absorption capability within the radio frequency (RF) band [73]. Furthermore, CIP demonstrates a high Curie temperature, making it suitable for induction heating applications [74]. Nevertheless, it is important to note that its high Curie temperature may lead to overheating concerns if the cells are exposed to an applied magnetic field for a defined duration. Following the degradation mechanism of CIP, carbonyl iron is a highly pure form of iron, thus it undergoes an oxidation process. The corrosion behavior of metallic samples occurs because of electrochemical dissolution when the sample is in contact with the human body fluids [75]. Within a physiological environment, electrochemical corrosion occurs through oxygen absorption, which can be represented by the following **Eq. 3.5**. According to the equation, the iron material is oxidized into iron ions. Subsequently, dissolved oxygen consumes the electrons generated by the hydroxide. Ferrous hydroxide forms ferric hydroxide with the dissolved oxygen from the solution because of its unstable characteristics.

Anodic reaction: $Fe \longrightarrow Fe^{2+} + 2e^{-}$ (1)

Cathodic reaction: $O_2 + 2H_2O + 4e^{-} \longrightarrow 4OH^{-}$ (2) **(Eq. 3.5)**

Product of the reaction: $Fe^{2+} + 2OH^{-} \longrightarrow Fe(OH)_2$ (3)

$Fe(OH)_2 + 1/4O_2 + 1/2H_2O \longrightarrow Fe(OH)_3$ (4)

Since the instability of ferrous hydroxide, $Fe(OH)_2$, it was easy to be oxidized into ferric hydroxide by dissolved oxygen. The reaction can be expressed as **Eq. 3.5(4)**. Moreover, it is observed that the degradation product results in the formation of an oxide layer on its surface which is composed of iron and oxygen, resulting in iron oxides [76]. It is worth noting that the oxidation of CIP generally leads to a loss of their magnetic properties since iron oxides possess significantly lower saturation magnetization than the CIP [77], and thus, this may lower the mechanical performance of the intended applications.

On the other hand, iron (II,III) oxide (Fe_3O_4) has attracted significant attention for use as heating agents in hyperthermia due to its magnetic properties. Magnetic iron oxides are cost-effective, abundant in nature, exhibit low toxicity, possess physical and chemical stability, are biocompatible, and are environmentally friendly [22]. The magnetism in Fe_3O_4 is primarily attributed to the super exchange interactions between the metal ions (Fe^{2+}/Fe^{3+}) and oxygen ions [78]. Similar to CIP, the degradation process of iron (II,III) oxide involves the oxidation of the metal. As an iron species, it follows the degradation mechanism described in **Eq. 3.6**, with its dissolution involving contributions from both Fe^{2+} and Fe^{3+} ions. Additionally, Fe_3O_4 is least likely to cause any health hazard side effects since Fe^{3+} ions are already found in the human body [79].

$$Fe_3O_4 + 4H_2O \longrightarrow Fe^{2+} + Fe^{3+} + 8OH^- + 4e^- \quad (1)$$

$$Fe^{2+} + 2OH^- \longrightarrow Fe(OH)_2 \quad (2) \qquad \textbf{(Eq. 3.6)}$$

$$Fe^{3+} + 3OH^- \longrightarrow Fe(OH)_3 \quad (3)$$

The metal particles obtained from $(Mn,Fe)_2(P,Si)$-based compound, which is developed in this project, has been introduced and research regarding its potential to be utilized as a heater agent. However, compared to the CIP and Fe_3O_4 that has been commercially used for medical and pharmaceutical purposes, there has been no report regarding the use of $(Mn,Fe)_2(P,Si)$-based compound and its degradation mechanism study particular in medical applications. Considering each element of this compound (i.e., pure Fe, Mn, P, and Si), they are non-toxic and biocompatible since they all have been widely implemented into biomedical applications, especially as biomaterials in implants. Moreover, they are also a part of consumable mineral elements.

According to non-metallic particles (i.e., Si and P), phosphorous is an essential element in biological systems, playing a crucial role in the formation of DNA, RNA, and ATP, the primary energy carrier in cells. It is also significant in various biomedical applications, particularly in bone repair and regeneration, due to its involvement in the formation of bone mineral (apatite). After ingestion, phosphorus typically binds with oxygen and exists as phosphate in the body. Over 80% of total phosphate is present in bones and teeth as apatite, ensuring no severe adverse effects on human living cells [80]. Silicon (Si) has been extensively used in MEMS-based sensors [81] and in various biomedical applications. Silicon dioxide (SiO_2), in particular, is commonly used in medical implants and drug delivery systems [82]. These applications demonstrate the biocompatibility of silicon content with living cells, supporting its safe use in biomedical contexts.

For metallic components, Fe and Mn have shown a promising result in terms of biocompatibility. These elements are commonly used for the production of temporary implant materials such as Fe-Mn alloy stents [83]. For metal degradation, similar to the degradation mechanism of iron mentioned above, iron particles of this compound can be degraded through corrosion and oxidation processes. The degradation process of manganese is also similar to that described before for iron degradation, as described in **Eq. 3.7**. Mn is a biocompatible element in the body and its presence is a vital necessity for many reactions and metabolisms such as nucleic acid synthesis; thus, it can be excreted through natural metabolic processes [84].

Anodic reaction: $Mn \longrightarrow Mn^{2+} + 2e^-$ (1)

Cathodic reaction: $O_2 + 2H_2O + 4e^- \longrightarrow 4OH^-$ (2) **(Eq. 3.7)**

Product of the reaction: $Mn^{2+} + 2OH^- \longrightarrow Mn(OH)_2$ (3)

In the human body, the clearance of the magnetic particles depends on their particle size. For small iron particles (< 6 nm), the particles can be filtered by renal infiltration and excreted in urine. For medium to large particles (10 nm to 8 μm), the particles are taken up by the MPS immune system (mononuclear phagocyte system) [85]. One concern is the hydroxyl radical (HO•), the obtained product from the iron degradation process. While the use of CIP has generally shown no adverse effects on biological systems, hydroxyl radicals have a high potential to harm the biological body since they highly react with all biological macromolecules, possess significant pro-inflammatory properties, and cause damage to cells. Therefore, limiting the amount of iron is crucial to control the quantity of hydroxyl radicals in an appropriate range to control the adverse effects that may be caused due to its action. Due to the brief culture duration employed in this study, the biocompatibility of metallic particles is expected to have a minimal effect on the cell cultures.

3.2.3. Fabrication Methods of Wax Matrix and Magnetocaloric Composite

The fabrication process of the magnetocaloric transient membrane involved two primary stages. First, a mixture of bayberry wax and lanolin wax was prepared to form a wax matrix, as illustrated in **Figure 3.12**. The ideal melting point range should be lower than the transition temperature Tc to guarantee that the heat produced by magnetic particles can melt completely before the particles lose their magnetization after going beyond their Tc. To further avoid any damage to living cells, the melting point should be within the therapeutic range, which is not higher than 47°C. With this, the desired melting point of the wax matrix should be around 41-42°C.

Various volume fractions of the two wax components were blended to investigate their melting point. The total volume (V_{total}), the volume of component 1 and component 2 (V_1, V_2), and their respective masses (m_1, m_2) were determined based on **Eq. 3.8**. The wax components were then weighed according to the equation, and the average density of the resulting matrix (ρ_{total}) was calculated using **Eq. 3.8**. **Table 3.2**. illustrates the quantities of bayberry and lanolin wax required to produce a 1 ml wax matrix with different volume fractions of bayberry wax, starting from 30, 32, 34, 36, 38, and 40 vol.-% BBW, until the desired melting point is achieved.

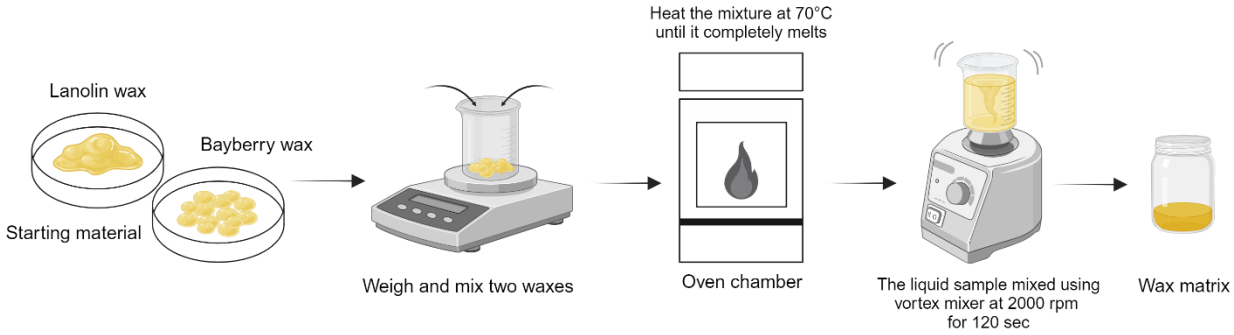

Figure 3.12 A schematic illustration of the wax matrix fabrication process.

$$V_{total} = V_1 + V_2$$

$$V_1 = XV_{total} = \frac{m_1}{\rho_1} \qquad V_2 = (1 - X)V_{total} = \frac{m_2}{\rho_2}$$

$$\therefore m_1 = \rho_1 X V_{total} \qquad \therefore m_2 = \rho_2(1 - x)V_{total}$$

$$\rho_{total} = \frac{(m_1 + m_2)\rho_1\rho_2}{m_1\rho_2 + m_2\rho_1}$$

(Eq. 3.8)

Table 3.2 Quantities of wax materials required to fabricate 1 ml of the wax matrices with different volume fractions of bayberry wax (BBW).

Process	Volume fraction of component 1 (X)	Component 1 Bayberry wax		Component 2 Lanolin wax		Average density (g/ml)
		ρ_1 (g/ml)	m_1(g)	ρ_2 (g/ml)	m_2 (g)	
Wax matrix (1 ml)	0.30	0.985	0.296	0.940	0.658	0.9535
	0.32		0.315		0.639	0.9544
	0.34		0.335		0.620	0.9553
	0.36		0.355		0.602	0.9562
	0.38		0.374		0.583	0.9571
	0.40		0.394		0.564	0.9580

In the second stage, the magnetic composite was prepared by blending the wax matrix with magnetic particles, specifically $(Mn,Fe)_2(P,Si)$ magnetocaloric particles, Carbonyl Iron Powder (CIP), and iron (II, III) oxide as detailed previously. Again, to achieve the desired total volume of magnetic composite, the mass of each component was calculated analogously to the wax matrix using **Eq 3.7**. For example, **Table 3.3** presents the calculated masses of magnetic particles and wax matrix required to produce 1 ml of magnetic composite with different $(Mn,Fe)_2(P,Si)$ particles, CIP, and iron (II, III) oxide volume fraction, respectively. The density of the $(Mn,Fe)_2(P,Si)$ compound, utilized for determining the quantity of the compound in composite fabrication, was derived from the XRD refinement of the $(Mn,Fe)_2(P,Si)$ compound.

The schematic illustration of the fabrication process of magnetic composite is demonstrated in **Figure 3.13**. The wax matrix and magnetic particles were combined in a glass vial and heated to around 70°C until fully liquefied within the oven chamber. The resulting liquid composite was mixed using a vortex mixer for at least 120 seconds at 2000 rpm to ensure even dispersion of the particles.

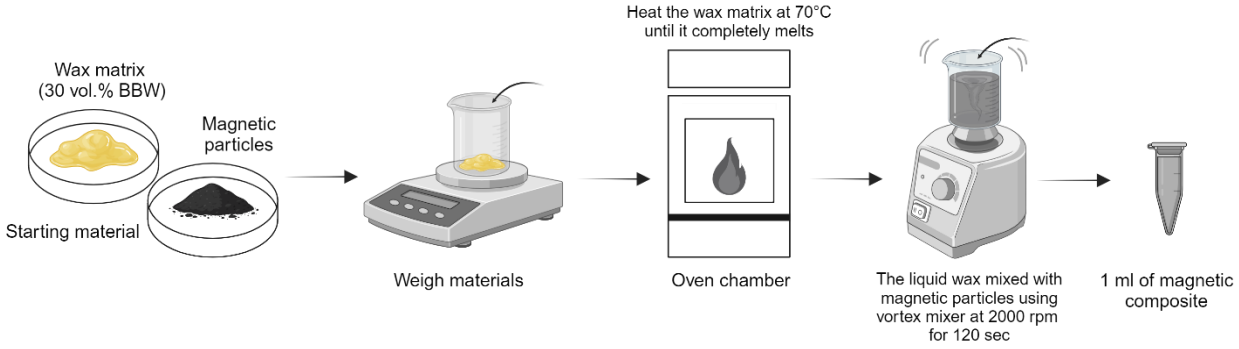

Figure 3.13 An overview of the magnetic wax composites fabrication process.

Table 3.3 The starting materials used to fabricate 1 ml of the magnetic wax composites with different volume fractions.

Process Composite	Volume fraction of component 1 (X)	Component 1 $(Mn,Fe)_2(P,Si)$ particles		Component 2 Wax matrix (30 vol.-% BBW)	
		ρ_1 (g/ml)	m_1(g)	ρ_2 (g/ml)	m_2 (g)
Magnetocaloric Composite (1 ml)	0.05	6.994	0.350	0.9535	0.906
	0.1		0.699		0.858
	0.15		1.049		0.810
	0.2		1.399		0.763
	0.25		1.749		0.715
Process Composite	**Volume fraction of component 1 (X)**	**Component 1 CIP**		**Component 2 Wax matrix (30 vol.-% BBW)**	
		ρ_1 (g/ml)	m_1(g)	ρ_2 (g/ml)	m_2 (g)
CIP Composite (1 ml)	0.05	7.86	0.393	0.9535	0.906
	0.1		0.786		0.858
	0.15		1.179		0.810
	0.2		1.572		0.763
	0.25		1.965		0.715
Process Composite	**Volume fraction of component 1 (X)**	**Component 1 Fe_3O_4 particles**		**Component 2 Wax matrix (30 vol.-% BBW)**	
		ρ_1 (g/ml)	m_1(g)	ρ_2 (g/ml)	m_2 (g)
Fe_3O_4 Composite (1 ml)	0.05	5.1	0.255	0.9535	0.906
	0.1		0.510		0.858
	0.15		0.765		0.810
	0.2		1.020		0.763
	0.25		1.275		0.715

3.2.4. Characterization Methods of Wax Matrix and Magnetocaloric Composite

The fabrication and characterization of the magnetic composite involved different methods and techniques to assess its suitability as the membrane barrier to separate two cell cultures. In this section, we outline the experiments conducted within the scope of this study, detailing both the theoretical aspects and experimental designs. The section starts with explaining the theoretical aspects of each characterization technique and the preparation process employed in this study. While some theoretical aspects, such as magnetization measurement, are already discussed in the section on magnetocaloric material in **Section 3.1**, this section focuses on the specific preparation procedures for characterizing the magnetization of the magnetic composite. Overall, the characterization methods are categorized into two main objectives: magnetization properties and thermal behavior analysis.

3.2.4.1. Magnetic Properties

The magnetic hysteresis of magnetic samples was measured using the MPMS 5XL SQUID (Quantum Design MPMS) at 310 K (36.85°C). An automated reciprocating sample option (RSO) ensured precise positioning of the sample in the pickup coil of the SQUID at a targeted position of 1.5 cm before each measurement. Magnetic powder samples weighing approximately 1.5-2 mg were used for all measurements. Each sample (i.e., CIP, Fe_3O_4, and $(Mn,Fe)_2(P,Si)$ particles) was encapsulated within a gelatin capsule, which was then inserted into a plastic straw. Field-dependent magnetization measurements

(M-B curve) were conducted at 310 K with the magnetic field ranging from -1 T to 1 T. The measurement sequence involved scanning the field from 0 T to 1 T in 100 steps (101.01 Oe/step), then from 1 T to -1 T in 100 steps (202.02 Oe/step), and finally from -1 T to 1 T in 100 steps (202.02 Oe/step). The remanent magnetization and coercivity field of each magnetic particle were analyzed, and the hysteresis area (**Eq. 2.6**) was calculated using Origin Pro software.

3.2.4.2. Thermal Properties

3.2.4.2.1. Differential Scanning Calorimetry (DSC)

The thermal properties of the wax matrix were investigated using differential scanning calorimetry (DSC). The technique involves measuring the difference in heat flow between the studied material and a reference as a function of temperature in response to heating and cooling. As shown in **Figure 3.14**, the sample enclosed in a pan and empty reference pan are placed on a thermoelectric disk within a furnace. Then, the two are heated up and cooled down as a cycle, resulting in a temperature change in the furnace. The differential heat flow to the sample and reference is then measured.

Because of the heat capacity (C_p) of the sample, the reference side, typically represented by an empty pan, heats faster than the sample side during the heating cycle. **Figure 3.15** illustrates the temperature profiles of the reference pan (green line) and the sample pan (red line) as functions of time. Initially, the reference temperature increases more rapidly than the sample temperature. Both temperature curves follow parallel trends under constant heating until a sample phase transition, such as solid-liquid phase (melting), occurs. Whereas the reference temperature keeps its linear increase, the sample temperature stays constant during the melting process. Once melting is complete, the sample temperature resumes its linear increase. The use of a reference material helps differentiate the heat flow associated with the sample's phase transition from other effects, allowing measurement of the absorption of heat or release of heat by the sample. Due to this, it is commonly used to determine physical properties such as melting temperature and enthalpy [86]. As a result, the differential temperature signal (ΔT) between the two curves is also analyzed. During the middle section of the curve, the difference calculation produces a peak (blue), which signifies the endothermic melting process. The melting enthalpy or the enthalpy of fusion which is the amount of energy required to melt 1 g of the solid sample to liquid phase, is determined as an area between the melting peak and the base line is directly related to the transition's heat content (enthalpy, J/g).

A standard DSC heat-cool-heat method [87] was employed to evaluate the thermal properties of phase change materials in all samples. The initial heating cycle is used to eliminate the thermal history of the materials. DSC measurements were conducted using a TA-Q2000 DSC instrument with the use of a liquid nitrogen cooling system. The temperature range for this analysis spanned from -20°C to 60°C, with a sweep rate of 20 K/min for samples weighing approximately 16-18 mg. The sample was encapsulated in a Tzero™ aluminum pan with punctured lid to facilitate water evaporation and the release of gases generated during the heating and cooling cycles. During the experiment, both the sample and reference pans were maintained at the same temperature. The resulting data were utilized to determine the melting temperature and enthalpy of fusion for each wax matrix sample with varying bayberry wax (BBW) content, ranging from 30 to 38 vol.% BBW. The analysis of the data was performed using TA Universal Analysis and Origin Pro software.

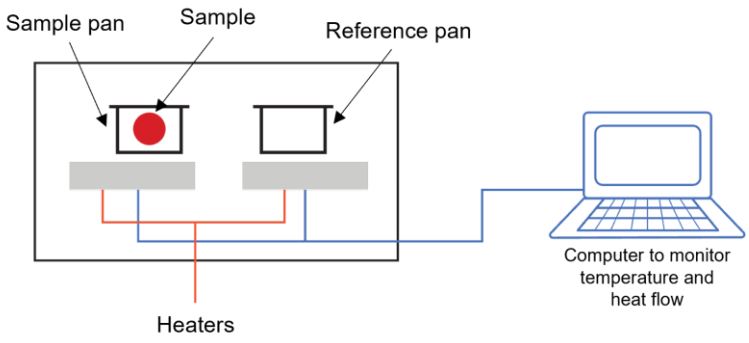

Figure 3.14 A schematic diagram of the Differential Scanning Calorimetry (DSC) system.

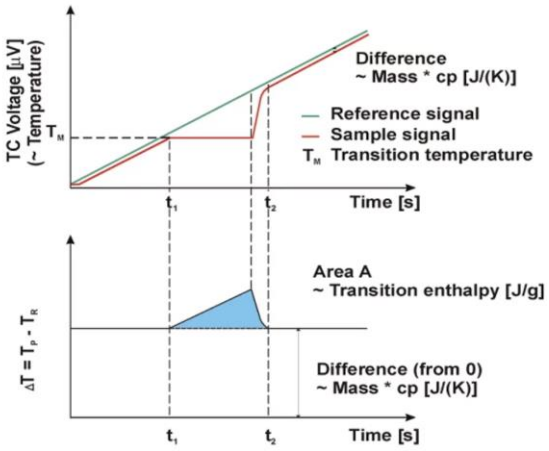

Figure 3.15 An illustration of the DSC measurement showing the temperatures of the reference and sample pans measured as a function of time.

3.2.4.2.2. Inductive Heating under Magnetic Field

The heating behavior of the fabricated magnetic composite when subjected to either an alternating magnetic field or a static magnetic field (SMF) was experimentally investigated. The experimental setups for these investigations are illustrated in **Figure 3.16** for the alternating magnetic field and **Figure 3.17** for the static magnetic field (SMF).

Inductive Heating under Alternating Magnetic Field (AMF)

The heating behavior of the magnetic composite was investigated under an alternating magnetic field (AMF). The heating properties of the magnetic particles were tested using an alternating magnetic field source (Magnetherm, nanoTherics Ltd.), equipped with an optical temperature probe, as shown in **Figure 3.16**. This device contains a coil that generates an alternating magnetic field in its core when an alternating current is applied. The experimental setup included three parameters: type of magnetic particles, magnetic particle volume fraction, frequency, and magnetic field strength, detailed in **Table 3.4**. To examine the effects of these parameters, specifically magnetic particle concentrations and magnetic field strength, the temperature of 1 ml samples of the magnetic composite (with 10, 15, 20, and 25 vol.% of magnetic particles) was monitored over time. The alternating magnetic field strengths used were 2.5 mT, 10 mT, and 15 mT at a fixed frequency of 244 kHz.

For sample preparation, each approximately 1 ml sample of the composite was placed in an Eppendorf tube, as illustrated in **Figure 3.17**. The tube was positioned at the center of the coil using a sample holder.

Two glass fiber optic thermometers were inserted into the sample to measure the temperature at the core and bottom of the sample, ensuring homogeneity of heating throughout the sample volume.

A custom user interface was programmed to manage the measurements for each experimental condition. This interface allowed users to set field parameters (strength and frequency), duration of AMF exposure, recording time before and after exposure, and the number of repetitions for each parameter set. Temperature equilibration was achieved when the variation between probe A and probe B was less than 0.5°C/sec. The water-cooling system was maintained at room temperature. Temperature recording began 60 seconds before activating the AMF and continued until either the set duration (10-15 min) was reached or one of the temperature values exceeded 90°C. Each field strength (2.5, 10, and 15 mT) was applied to all five magnetic particle fractions. Three types of magnetic particles were investigated: carbonyl iron powder (CIP), Fe_3O_4, and magnetocaloric (MCM) particles. The efficiency of heat generation was compared across these particles, with the expectation that MCM particles would cease heating or maintain a constant temperature upon exceeding their Curie temperature (43 °C). Repeated measurements were conducted to ensure consistent heating behavior across repetitions.

The experimental data produced two temperature values. The temperature measured at the center of the sample was used to evaluate the heating rate (HR) and specific loss power (SLP) of the sample. The heating rate (HR) was calculated using **Eq. 3.9**, where T denotes temperature and t denotes time in seconds.

$$HR = \frac{\Delta T}{\Delta t} = \frac{T_{off} - T_{on}}{t_{off} - t_{on}} \quad \textbf{(Eq. 3.9)}$$

Table 3.4 Experiment parameters of inductive heating characterization.

Experiment parameter	
Type of magnetic particle	CIP, Fe_3O_4, and Magnetocaloric (MCM) particles
Magnetic particle concentration	5, 10, 15, 20, and 25 vol.% of magnetic particles
Magnetic field strength	2.5, 10, and 15 mT

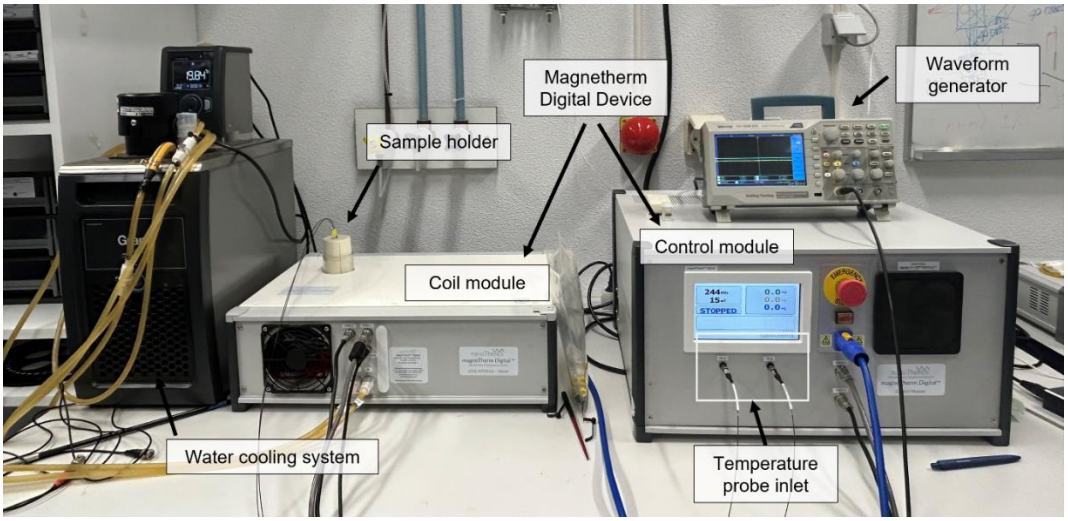

Figure 3.16 Experiment set-up for inductive heating testing under alternating magnetic field (AMF). The sample is placed in the sample holder, which is then inserted into the coil module equipped with a water-cooling system.

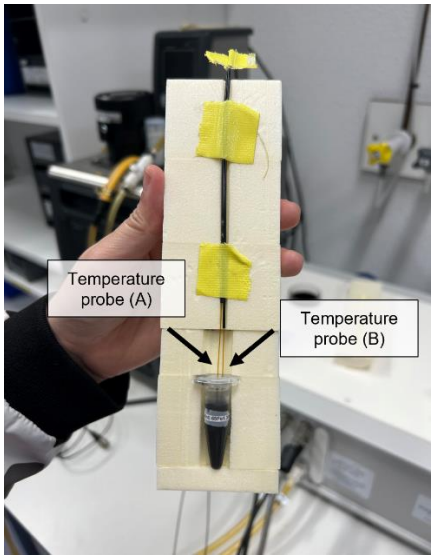

Figure 3.17 The experimental setup where the sample is inserted into the sample holder inside the coil module. Two temperature probes are inserted into the sample: probe A is positioned at the center, and probe B is located at the bottom part of the sample. These probes are used to record the temperature change over time.

Inductive Heating under Static Magnetic Field (SMF)

An investigation of the thermal behavior of magnetic composites under a static magnetic field (SMF) was conducted using two NdFeB permanent magnets placed symmetrically on either side of a sample holder, as shown in **Figure 3.18**. A 1 ml magnetic composite sample, containing 25 vol.% concentration of magnetic particles, was positioned between the two magnets. The distance between each magnet and the sample was maintained at 2.5 cm. The magnetic field of each NdFeB magnet and at the sample holder was measured before performing the experiment using a WT10A Gauss meter. The temperature change of the sample was captured for 10 min after placement in between the magnetic field using a precision infrared thermal camera (VarioCAM, JENOPTIK).

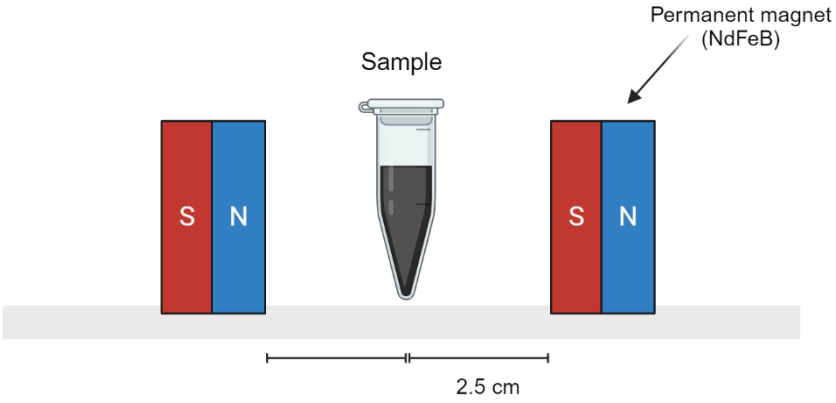

Figure 3.18 A schematic of the experimental setup for heating magnetic particles under a static magnetic field.

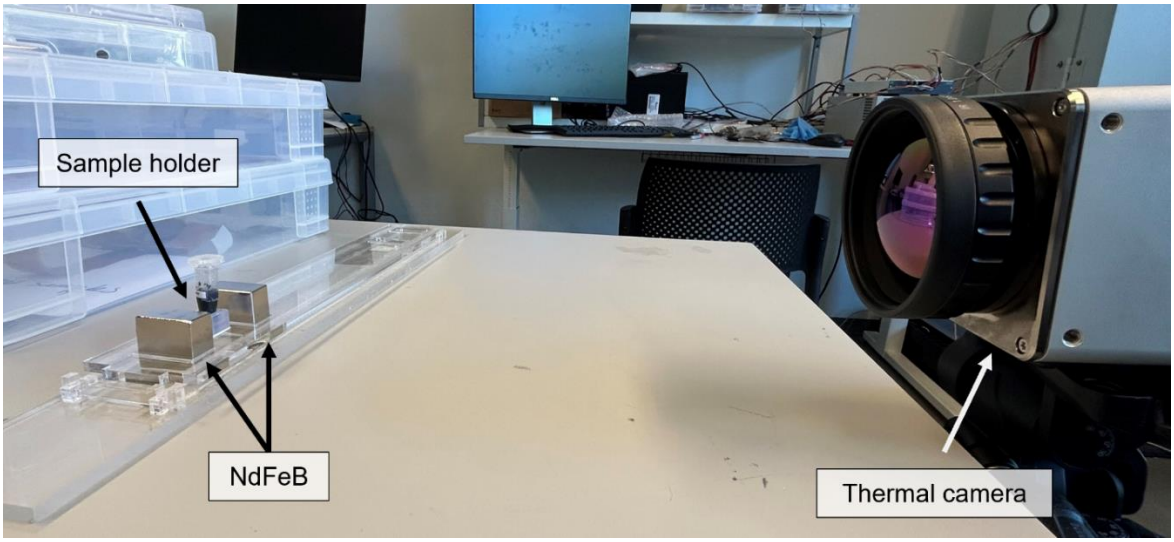

Figure 3.19 Experiment set-up for inductive heating testing under static magnetic field (SMF).

3.3. Part 3: Biodegradability Assessment

The magnetocaloric wax-based composite was fabricated, characterized, and evaluated for its biodegradability and biocompatibility. Ensuring these properties is crucial to prevent adverse effects on cell cultures from the materials or their by-products. Additionally, maintaining the hydrophobic nature of the material is important to prevent water permeability, preserve media separation, and reduce cell penetration before appropriate maturation is reached. This section describes the biodegradation test used in this project.

3.3.1. Biodegradability Test

The biodegradation behavior of the magnetic wax composite was investigated by monitoring three parameters: wet mass, water uptake, and structural change. Samples of the pure wax matrix (bayberry and lanolin wax) and magnetic composite (wax matrix mixed with 5 vol.% magnetocaloric particles) were assessed for degradability. The samples, measuring 1 cm x 1 cm x 0.25 cm, were prepared by injecting the melted composite into 3D-printed molds. The samples were taken out of the molds after they solidified. The fabricated samples are displayed in **Figure 3.20**. To mimic application conditions, the samples were immersed in glass vials containing PBS (pH 7) and incubated at 37°C, as shown in **Figure 3.21**. Initial parameters of the samples were recorded on day 0 and then monitored every 7 days.

For the measurement, samples were taken out of the incubator and allowed to cool to room temperature in the glass vial. The wet mass was recorded after removing the sample from the vial and flushing it with compressed air to remove surface water. This measured weight was then used to evaluate water absorption. The water absorption percentage was determined by calculating the ratio of the weight reduction of the sample after degradation to the original weight of the sample before degradation. This was calculated using **Eq. 3.10**, where W_h refers to the hydrated weight of the sample and W_i refers to the dry weight of the sample before degradation.

$$Water\ absorption\ (\%) = \frac{W_h - W_i}{W_i} \times 100 \qquad \textbf{(Eq. 3.10)}$$

Additionally, before returning the samples to the solution, microcracks and the rheological properties of the wax samples at different stages of dissolution were examined using SEM.

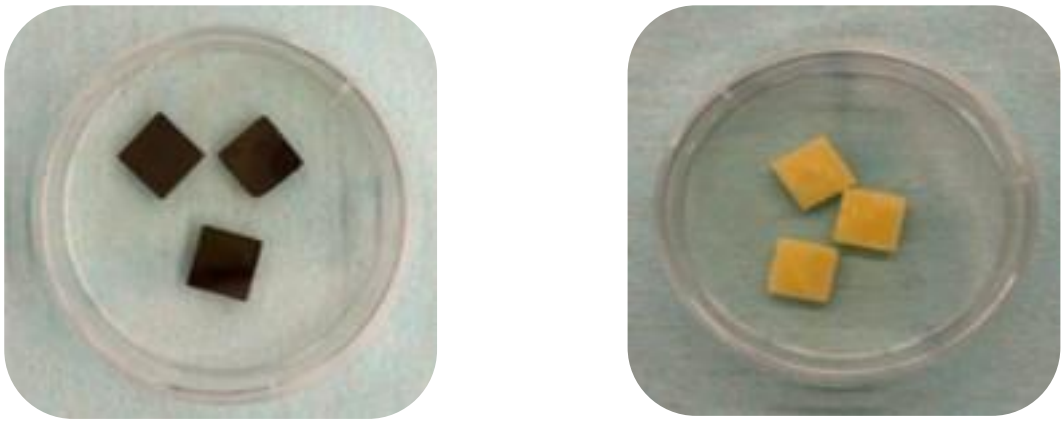

Figure 3.20 Fabricated samples for the biodegradability test of wax composite with 5 vol.% magnetocaloric particles (MCM) (left) and wax matrix composed of lanolin and bayberry wax (right) prepared by using 3D-printed mold.

Figure 3.21 Samples of wax composite with 5 vol.% magnetocaloric particles (MCM) and wax matrix immersed in PBS were placed inside an incubator set at 37°C.

4

Results and Discussion

In this chapter, the results of the experiments outlined in **Section 3** are presented. Firstly, the results obtained from the characterization of magnetocaloric particles are presented and discussed. Following this, the results related to the synthesis and characterization of magnetocaloric wax-based composite are explained. Finally, the results of the biodegradability test are reported.

4.1. Part 1: Characterization of Magnetocaloric Particles (MCM)

4.1.1. Crytal Structure Analysis: X-ray Diffraction (XRD)

4.1.1.1. Crystal Structure Analysis of $Mn_{0.65}Fe_{1.30}P_{0.65}Si_{0.37}$ Compound

The X-ray diffraction (XRD) patterns of $Mn_{0.65}Fe_{1.30}P_{0.65}Si_{0.37}$ samples were collected at 80°C to ensure that measured lattice parameters were derived for the same magnetic state. **Figure 4.1** shows a Rietveld refinement of the XRD data of bulk $Mn_{0.65}Fe_{1.30}P_{0.65}Si_{0.37}$ material in the paramagnetic (PM) state. The hexagonal Fe_2P-type phase was identified as the main phase. The only impurity phase present in the compound is a cubic $(Mn,Fe)_3Si$-type impurity phase with a weight fraction of 31.76(2.81) wt.%. The presence of this impurity phase results in a reduction in the phase fraction of the main phase, which may contribute to the instability and inhomogeneity of the sample. After melt spinning, a short heat treatment is conducted to achieve a more homogeneous composition and fine-grained microstructure [88]. **Figure 4.2a** and **Figure 4.2b** display the XRD patterns of the $Mn_{0.65}Fe_{1.30}P_{0.65}Si_{0.37}$ sample before and after annealing. The main phase remains the hexagonal Fe_2P-type phase. Notably, the XRD pattern of the annealed sample lacks peaks associated with impurity phases (indicated by the red arrow), suggesting that the annealing process effectively eliminates the impurity phase from the sample.

Before incorporating the synthesized $Mn_{0.65}Fe_{1.30}P_{0.65}Si_{0.37}$ particles into the fabrication of a magnetic wax composite for transient membranes, the sample underwent a high-energy ball milling (HEBM) process for 1.25 h. This step ensures that the particle size is reduced to the desired range of 1-10 µm. **Figure 4.3** shows the XRD pattern of $Mn_{0.65}Fe_{1.30}P_{0.65}Si_{0.37}$ powders after milling for 1.25 hours in the PM state, along with the XRD patterns of the sample collected after melt spinning and annealing. The three strongest reflections (111), (201), and (210) of the structure observed in the ball milled powders show that the overall structure remains at the same positions. The XRD peaks broaden after the milling process. This indicates a decrease in particle size. The broadening suggests that micro-strains during the ball-milling process may contribute to peak broadening [24], [89].

The average crystallite size of the samples from each fabrication process was estimated based on the Scherr equation (**Eq. 3.2**). The strongest XRD peak, which is the (111) reflection, was selected to estimate the crystallite size. As shown in **Table 4.1**, the average crystallite size initially increases from 0.046 to 0.496 µm after the annealing process. This increase may result from microstructure evolution, such as grain growth, during annealing. The increase in grain size plays an important role in enhancing the saturation magnetization [90]. After the milling process, the crystallite size of the particles is then reduced to 0.029 µm.

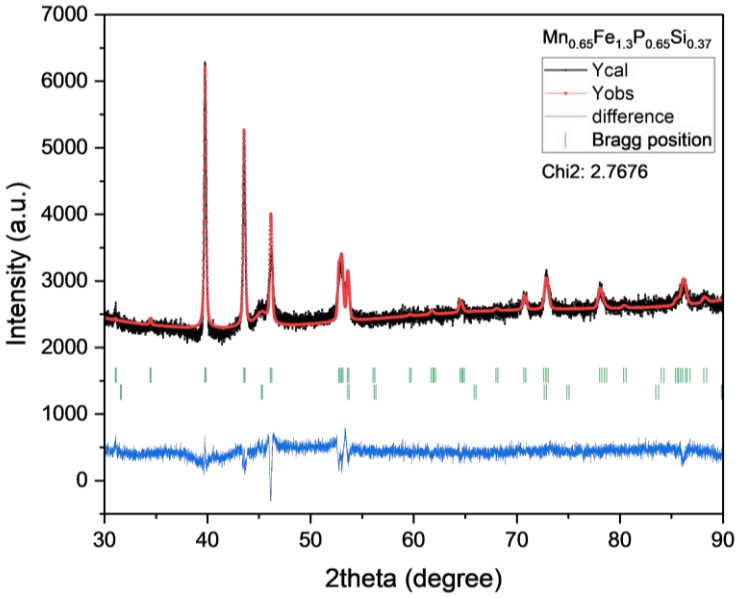

Figure 4.1 High-temperature XRD patterns of bulk $Mn_{0.65}Fe_{1.30}P_{0.65}Si_{0.37}$ sample after melt spinning in the paramagnetic (PM) state. The bottom blue line shows the difference between the observed and calculated intensities, whereas the redline represents the calculated intensities. The green vertical lines denote the Bragg peak position for the Fe_2P (top) and $(Mn,Fe)_3Si$ (bottom) structures.

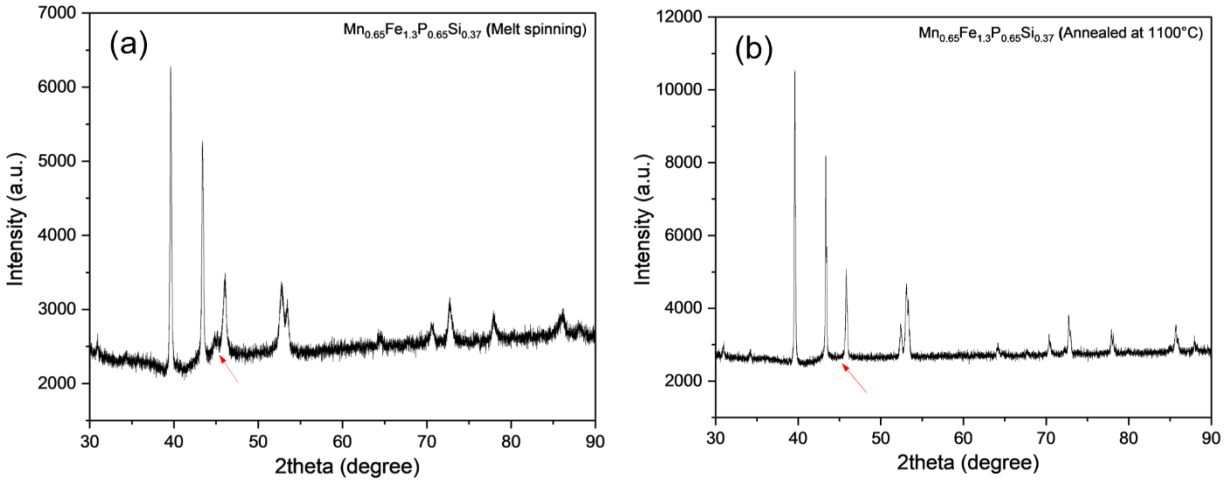

Figure 4.2 a) High-temperature XRD patterns of bulk $Mn_{0.65}Fe_{1.30}P_{0.65}Si_{0.37}$ sample in the PM state obtained after melt spinning and **b)** High-temperature XRD patterns of bulk $Mn_{0.65}Fe_{1.30}P_{0.65}Si_{0.37}$ sample in the PM state obtained after annealing at 1100°C (heat treatment).

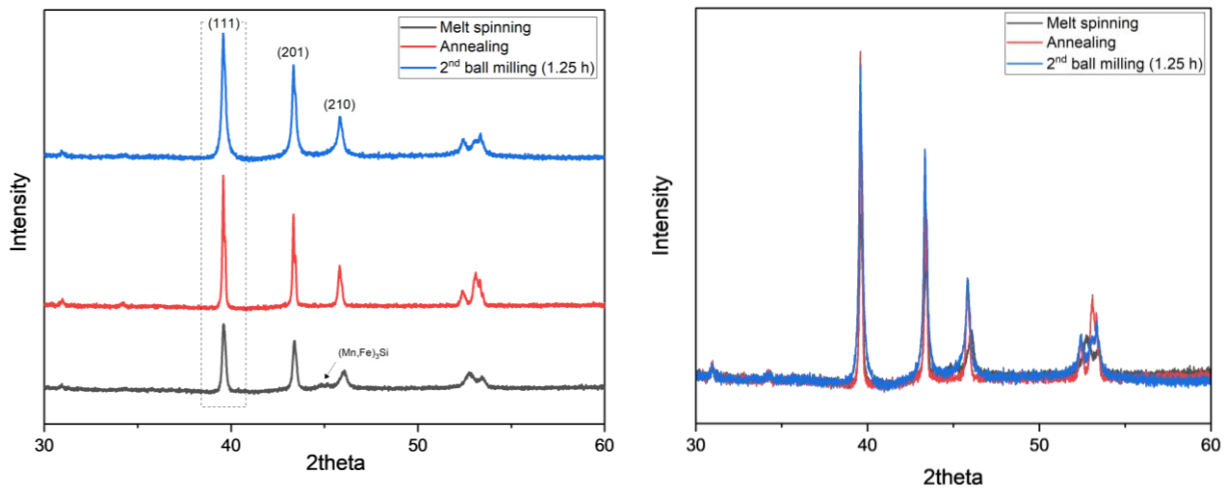

Figure 4.3 High-temperature XRD patterns of $Mn_{0.65}Fe_{1.30}P_{0.65}Si_{0.37}$ samples obtained from different synthesis procedures.

Table 4.1 Variation of crystallite size for $Mn_{0.65}Fe_{1.30}P_{0.65}Si_{0.37}$ samples from different synthesis procedures.

$Mn_{0.65}Fe_{1.30}P_{0.65}Si_{0.37}$ samples	**Crystallite size (μm)**
Melt spinning	0.046
Annealing at 1100°C	0.496
2nd ball milling for 1.25 h	0.029

4.1.1.2. $Mn_{0.65}Fe_{1.30}P_{0.65}Si_{0.37}$ Compound at Different Ball Milling Time

The effect of the ball-milling time on the structural properties was investigated further, the powder obtained after melt spinning was ball-milled for second time under an argon gas atmosphere with 60 wt.% of heptane and 10 wt.% of oleic acid for 1.25, 2.5, and 5.0 h. It is important to note that the $Mn_{0.65}Fe_{1.30}P_{0.65}Si_{0.37}$ compound used in this section is not the same batch as the one presented in **Section 4.1.1.1**. The XRD patterns were collected at room temperature. Similar to the previous XRD pattern results, the main phase was the hexagonal Fe_2P-type phase with three strongest reflections, which are (111), (201) and (210) of the hexagonal structure. As shown in **Figure 4.4**, the XRD peak intensities decrease while the peaks broaden as the milling time increases. This reduction is likely due to the intense plastic deformation and continuous fracturing occurring during the high-energy ball milling (HEBM) process. As shown in **Table 4.2**, the average crystallite size gradually decreases from 0.039 μm (ball-milled for 1.25 h) to 0.027 μm (ball-milled for 5.0 h) after the annealing process.

Table 4.2 Variation of crystallite size for $Mn_{0.65}Fe_{1.30}P_{0.65}Si_{0.37}$ samples from different ball-milling times.

Ball-milling time (h)	**Crystallite size (μm)**
0 (annealing at 1100°C)	0.484
1.25	0.039
2.5	0.031
5	0.027

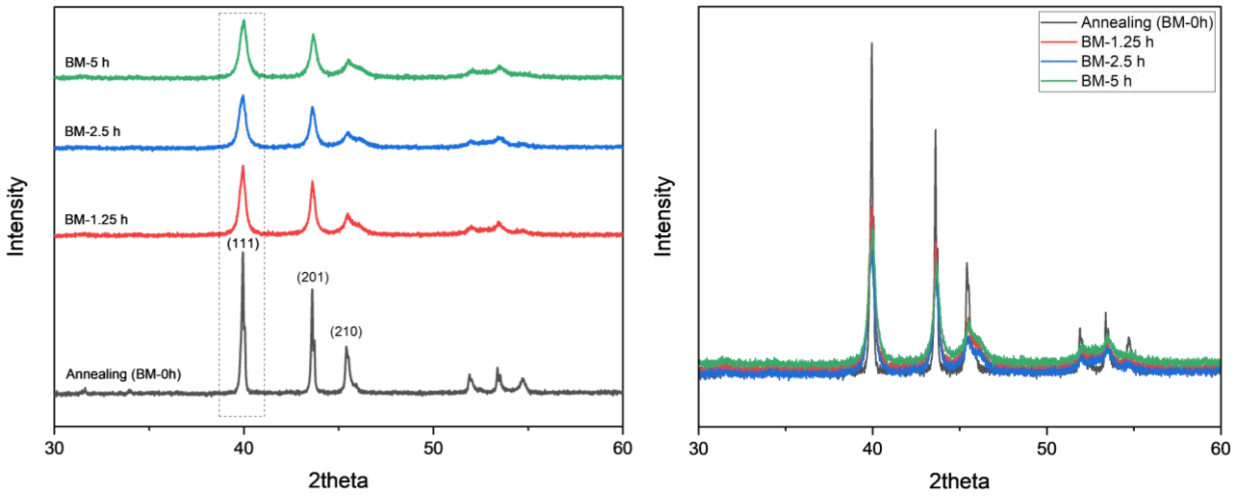

Figure 4.4 XRD patterns of $Mn_{0.65}Fe_{1.30}P_{0.65}Si_{0.37}$ samples obtained from different ball-milling times.

4.1.2. Particle Size Evaluation: SEM Images

The SEM images of the obtained $Mn_{0.65}Fe_{1.30}P_{0.65}Si_{0.37}$ particles used in **Section 4.1.1.1** are shown in **Figure 4.5**. **Figure 4.5a** and **Figure 4.5b** display the SEM images of the sample after annealing process, while **Figure 4.5c** and **Figure 4.5d** show the SEM images of the sample obtained after milling for 1.25 h. It is clearly seen that the sample before ball milling is broad in size distribution ranging from 10 to 30 µm. Due to the sample's inhomogeneity in shape and size, it is challenging to clearly define the exact particle size range of annealed sample. In contrast, the ball milled sample, with the surfactant and solvent, is more homogeneous in shape and size. The size distribution ranges between 1 to 5 µm, which aligns well with the expected particle size range required for further use in the fabrication of biodegradable membranes.

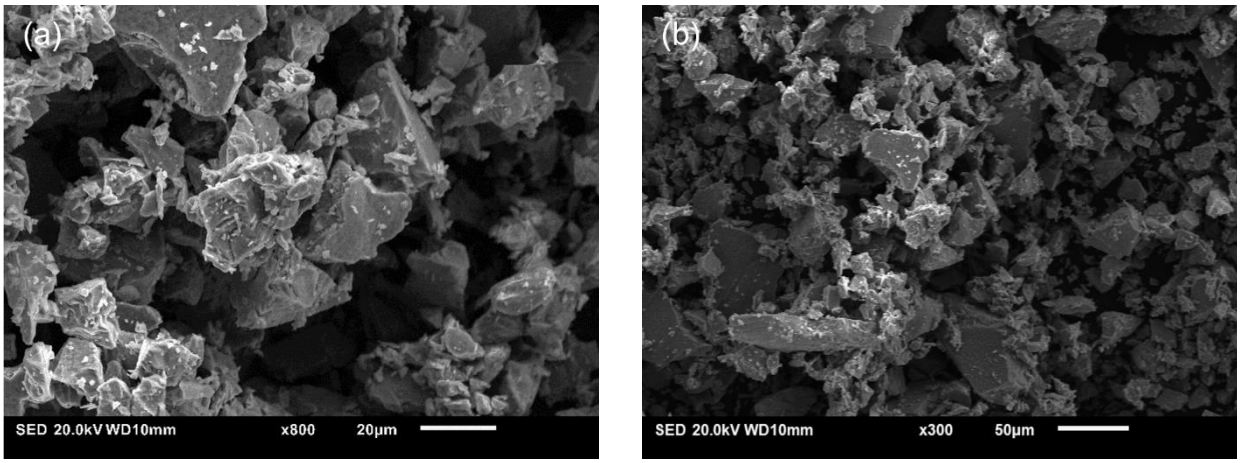

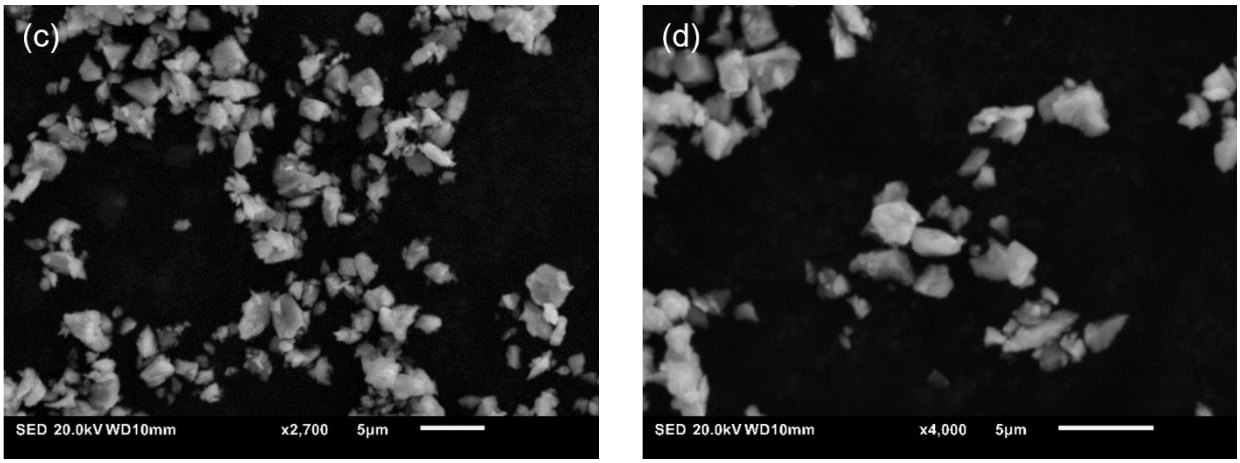

Figure 4.5 SEM images of $Mn_{0.65}Fe_{1.30}P_{0.65}Si_{0.37}$ compound **a-b)** before and **c-d)** after milling for 1.25 h.

4.1.3. Magnetic Properties: SQUID Measurement

4.1.3.1. Magnetic properties of $Mn_{0.65}Fe_{1.30}P_{0.65}Si_{0.37}$ Compound

Figure 4.6 shows the magnetic field dependence of the magnetization (M-H curve) of the $Mn_{0.65}Fe_{1.30}P_{0.65}Si_{0.37}$ samples before and after milling for 1.25 h at 5 K. For the sample obtained after melt spinning, the magnetization (M_s) reaches an approximate value of 103.16 Am^2/kg. The graph reveals a rapid initial increase in magnetization, which continues to rise gradually when exposed to magnetic fields greater than 1 T. However, the magnetization does not completely saturate, as it continues to increase slightly with higher magnetic fields. As mentioned earlier, grain size growth in magnetic particles after annealing improves magnetic properties, leading to an increase in saturation magnetization. The magnetization behavior of the sample after annealing at 1130°C for 2 h reaches its peak value of 148.74 Am^2/kg. It is evident from the graph that the sample's magnetization becomes saturated beyond a magnetic field greater than 1 T, indicating that further increases in the external magnetic field do not induce significant changes in the material's magnetization because all available magnetic domains have already aligned in the direction of the applied field. Additionally, **Figure 4.6** shows that the magnetization of the sample obtained after 2^{nd} ball-milling decreases to 137.65 Am^2/kg, which is lower than the magnetization of the sample obtained after annealing. This decrease is due to the gradual loss in long-range ferromagnetic order for smaller crystallite size [18].

Figure 4.7 displays the temperature dependence of the magnetization (M-T curve) for $Mn_{0.65}Fe_{1.30}P_{0.65}Si_{0.37}$ compounds obtained before and after milling with the solvent and surfactant for 1.25 h, measured at the high field of applied magnetic field at 1 T. The magnetization of the sample after melt spinning shows a ferromagnetic-to-paramagnetic transition, with the magnetization gradually diminishing as the temperature exceeds the Curie temperature (T_c). However, the curve does not exhibit a very sharp phase transition. In contrast, the sample obtained after the annealing process shows a sharp phase transition, resulting in a distinct decrease in magnetization once it exceeds T_c. The M-T curve becomes slightly less sharp after the second ball milling process compared to the sample obtained after annealing, likely due to the sample's sensitivity to strain and mechanical stress, which can affect its crystal structure or alignment of magnetic domains, leading to changes in magnetic behavior such as reduced magnetization.

Figure 4.8a shows the low field measurement (0.01 T) of $Mn_{0.65}Fe_{1.30}P_{0.65}Si_{0.37}$ compounds obtained before and after milling with the solvent and surfactant for 1.25 h. According to the Knee method, the Curie temperature (T_c) can be calculated by identifying where the temperature derivative of magnetization (dM/dT) slope is minimum [91]. In this project, T_c for each sample is determined using the M-T curve at low field (0.01 T) during the heating process. For the melt-spinning sample, the M-T curve does not exhibit a distinctive and sharp ferromagnetic-to-paramagnetic transition, making it challenging to precisely determine the Curie temperature. This may be due to the presence of impurity phases found in the XRD data and

inhomogeneous composition. **Figure 4.8b** presents the calculation of T_c for the samples obtained before (annealing) and after the second ball milling. The T_c values for the samples are in the same range, around 316-317 K (~43-44°C), which falls into the desired range for fabricating biodegradable membranes. A summary of the magnetic and structural properties of $Mn_{0.65}Fe_{1.30}P_{0.65}Si_{0.37}$ compound is presented in **Table 4.3**. It is noted that the thermal hysteresis (ΔT_{hys}) is estimated based on the difference between the maximum in the first derivative of the heating and cooling curves in an applied magnetic field of 0.01 T.

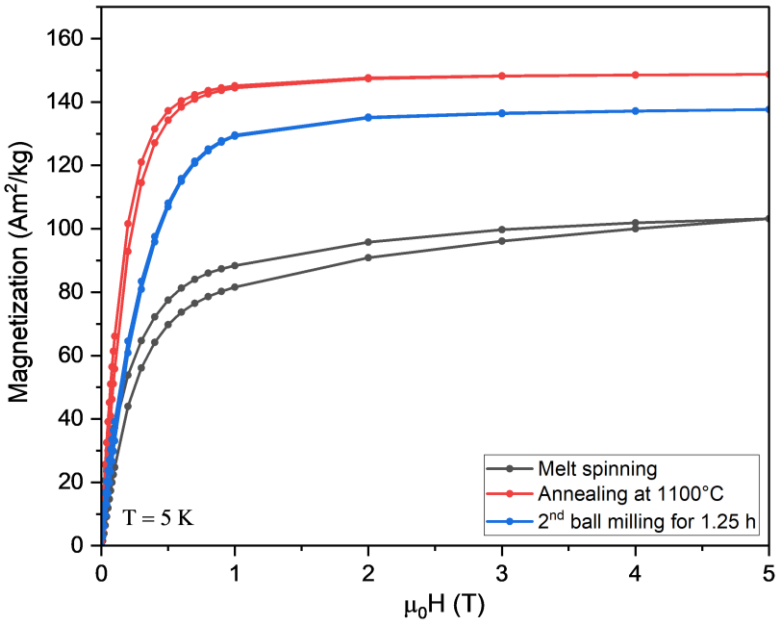

Figure 4.6 Isothermal field-dependent magnetization (M-H) curves at 5 K for $Mn_{0.65}Fe_{1.30}P_{0.65}Si_{0.37}$ sample obtained from different fabrication processes.

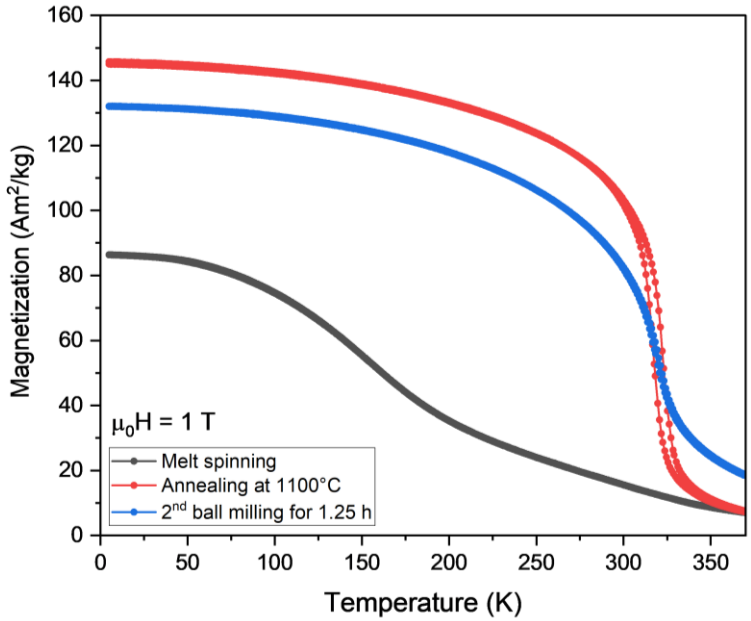

Figure 4.7 Temperature-dependent magnetization (M-T) curves at high field measurement (1 T) of $Mn_{0.65}Fe_{1.30}P_{0.65}Si_{0.37}$ sample obtained from different fabrication processes.

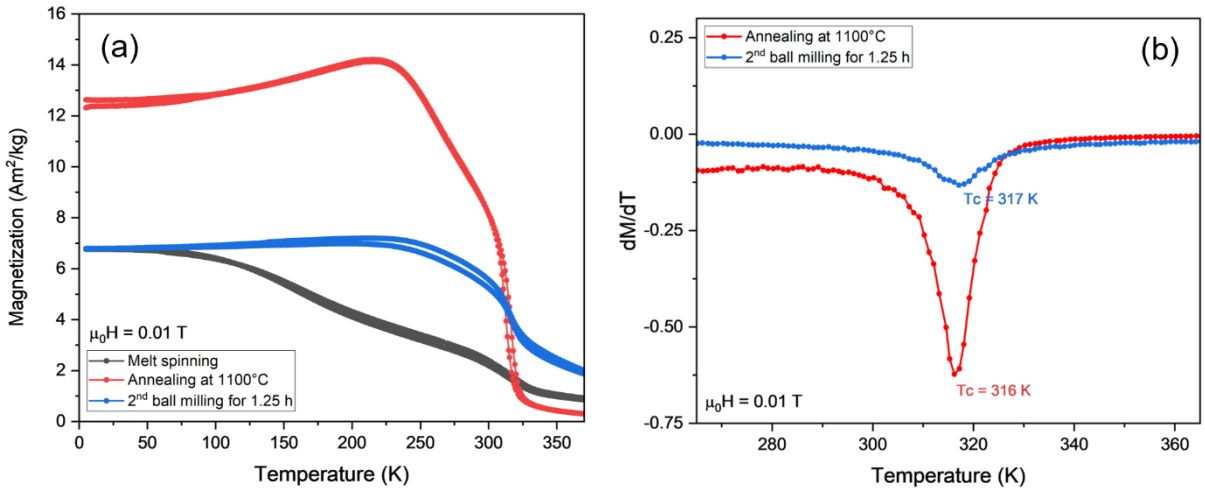

Figure 4.8 a) Temperature-dependent magnetization (M-T) curves at low field measurement (0.01 T) of $Mn_{0.65}Fe_{1.30}P_{0.65}Si_{0.37}$ sample with different fabrication processes and **b)** The derivative of magnetization (dM/dT) of $Mn_{0.65}Fe_{1.30}P_{0.65}Si_{0.37}$ sample obtained after annealing and 2nd ball-milling as a function of temperature.

Table 4.3 Properties of $Mn_{0.65}Fe_{1.30}P_{0.65}Si_{0.37}$ samples with different fabrication processes.

BM time (h)	M_s (Am^2/kg)	Tc (K)	$Tc_{(Cooling)}$ (K)	$Tc_{(Heating)}$ (K)	ΔT_{hys} (K)	Main phase (%)	Fe_3Si phase (%)
0-melt spinning	103.16	-	-	-	-	68.24 ± 1.83	31.76 ± 2.81
0 h-annealing	148.74	316	311	316	5	-	-
1.25	137.65	317	315	317	2	-	-

4.1.3.2. Reproduction of $Mn_{0.65}Fe_{1.30}P_{0.65}Si_{0.37}$ Compound

During the melt-spinning process, the magnetic compound is divided into two batches. It is essential to analyze the magnetic properties of each batch before implementing them with wax matrix to ensure that the magnetic properties are consistent across batches. The first batch of $Mn_{0.65}Fe_{1.30}P_{0.65}Si_{0.37}$ sample obtained after 2nd ball milling in this section is the same as the one described in **Section 4.1.3.1**. **Figure 4.9** shows the temperature dependence of the magnetization (M-T curve) for $Mn_{0.65}Fe_{1.30}P_{0.65}Si_{0.37}$ compounds obtained from the first and second batch at a high field of applied magnetic field at 1 T. The saturation magnetizations of the two batches are consistent, displaying similar magnetization behavior. Likewise, the phase transition behaviors observed in the M-T curve (**Figure 4.10**) show the same trend for both samples. As shown in **Figure 4.11**, although the two samples from different batches exhibit similar behavior in saturation magnetization and FM-PM phase transition, their Curie temperatures (T_c) differ slightly, decreasing from 317 K to 313 K. This variation may result from differences in the ribbon form of the samples obtained after melt spinning, which impacts the T_c values. The ribbon structures from the first batch appear to be smoother and more homogeneously formed than those from the second batch, which may have influenced the change in Curie temperature between the two samples. This observation indicates that magnetic particles in the $(Mn,Fe)_2(P,Si)$-based system are sensitive to the fabrication process. The procedures for creating ribbon samples during the melt-spinning process used in this project are manual. There is no precise timing for pressurizing the melted sample inside the quartz tube against the cold copper wheel to produce ribbons; this step is estimated based on user experience. Consequently, maintaining consistency in the magnetic particles is challenging, necessitating a check of the sample's properties before using it to fabricate biodegradable membranes.

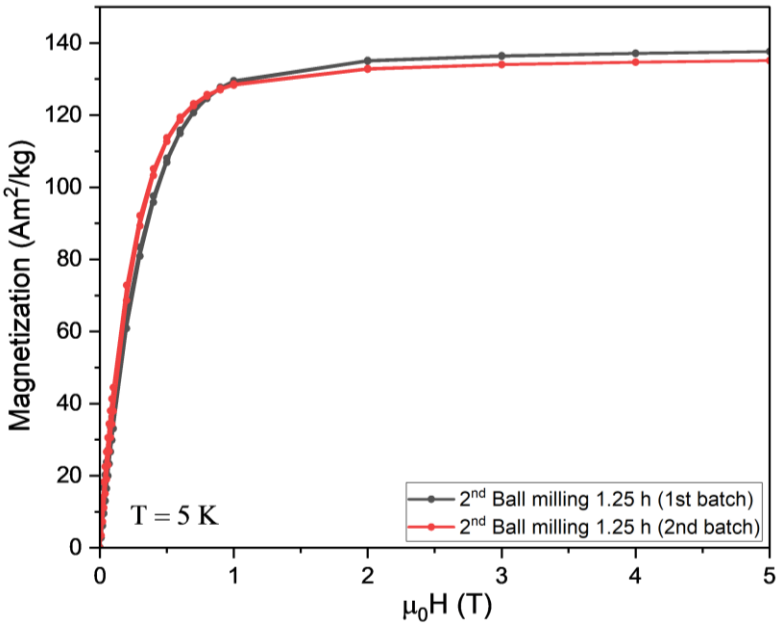

Figure 4.9 Field-dependent magnetization (M-H) curves at 5 K of 2nd ball-milling $Mn_{0.65}Fe_{1.30}P_{0.65}Si_{0.37}$ samples obtained from 1st and 2nd synthesis.

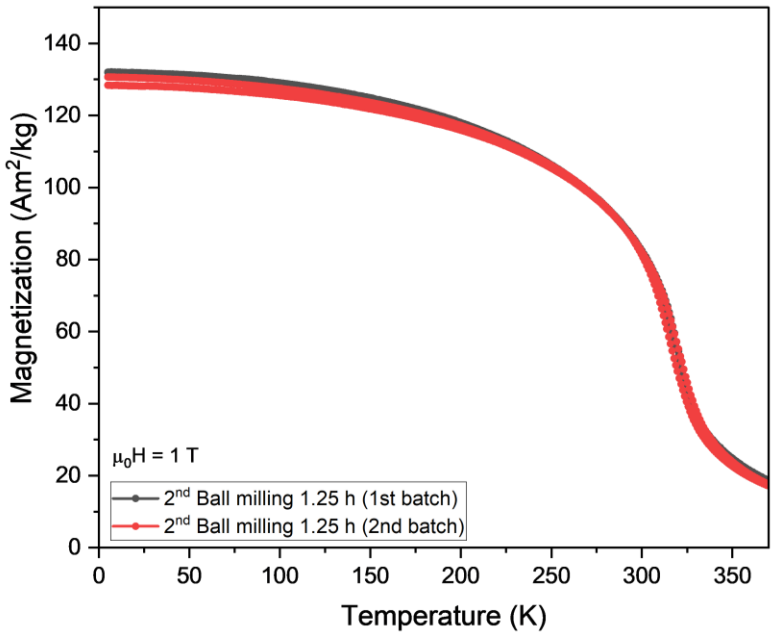

Figure 4.10 Temperature-dependent magnetization (M-T) curves at 1 T of 2nd ball-milling $Mn_{0.65}Fe_{1.30}P_{0.65}Si_{0.37}$ samples obtained from 1st and 2nd synthesis.

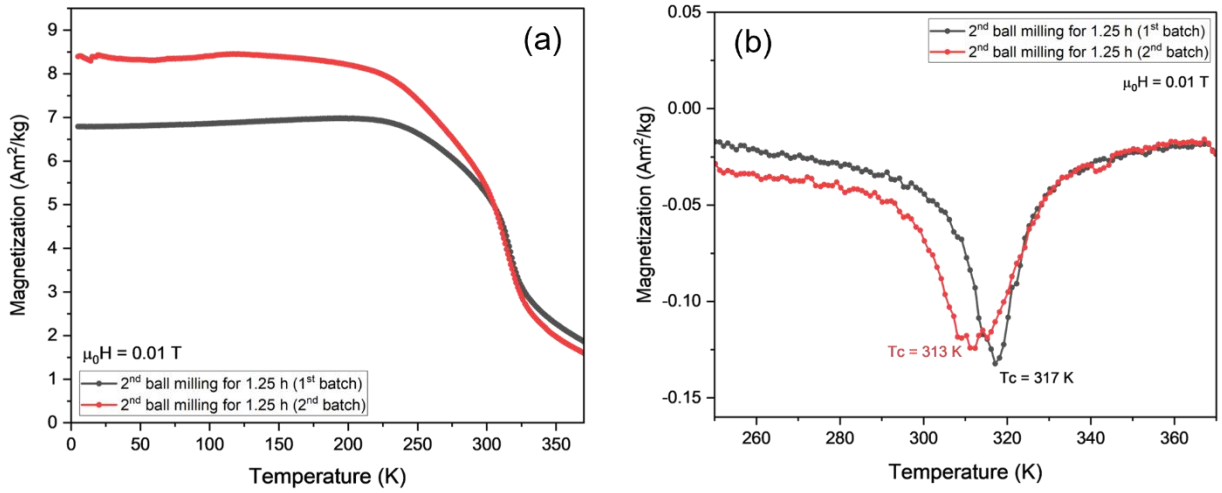

Figure 4.11 a) Temperature-dependent magnetization (M-T) curves at 0.01 T of the 2nd ball milling samples obtained from 1st and 2nd synthesis, and **b)** The derivative of its magnetization (dM/dT) as a function of temperature.

Figure 4.12 The structural form of ribbon samples obtained from **a)** the first and **b)** the second syntheses.

4.1.2.3. Magnetic Properties of $Mn_{0.65}Fe_{1.30}P_{0.65}Si_{0.37}$ at Different Ball Milling Time

The powder acquired in the first stage (annealing) was ball-milled once more with surfactant for 1.25, 2.5, and 5.0 h in order to investigate the effect of ball-milling time on the magnetic characteristics. The influence of the applied magnetic field on the magnetization of $Mn_{0.65}Fe_{1.30}P_{0.65}Si_{0.37}$ compound before and after the ball-milling process at different milling times (M-H curve) at 5 K is shown in **Figure 4.13**. The change in microstructure upon nano-sizing can also alter the magnetic properties compared to the bulk behavior [18]. The saturation magnetization of the sample decreases from 145.81 Am^2/kg to 77.38 Am^2/kg as the ball milling time increases from 0 to 5 h, respectively. Notably, the saturation magnetization declines with increasing ball milling times.

On the other hand, the temperature-dependent magnetization behavior (M-T curve) of the $Mn_{0.65}Fe_{1.30}P_{0.65}Si_{0.37}$ compound at 1 T, both pre-milling and post-milling with solvent and surfactant for varying ball milling durations, is illustrated in **Figure 4.14**. The M-T curve of the unmilled (0.0 h) distinctly exhibits a sharp transition from ferromagnetic to paramagnetic states. However, as the compounds were subjected to milling for different durations, the magnetization notably decreased over time. Consequently, the sharp

transition characteristic observed in the bulk sample gradually diminishes, resulting in a conserderable broadening of the transition zone. This phenomenon is likely linked to changes in the particle size distribution. According to the calculation of the Curie temperature based on the derivative dM/dT under a low magnetic field (0.01 T) shown in **Figure 4.15b**, the gradual reduction in magnetizations with increasing milling times also influences a slight decrease in the Curie temperature from 317 K (~44°C) to 316 K (~43°C).

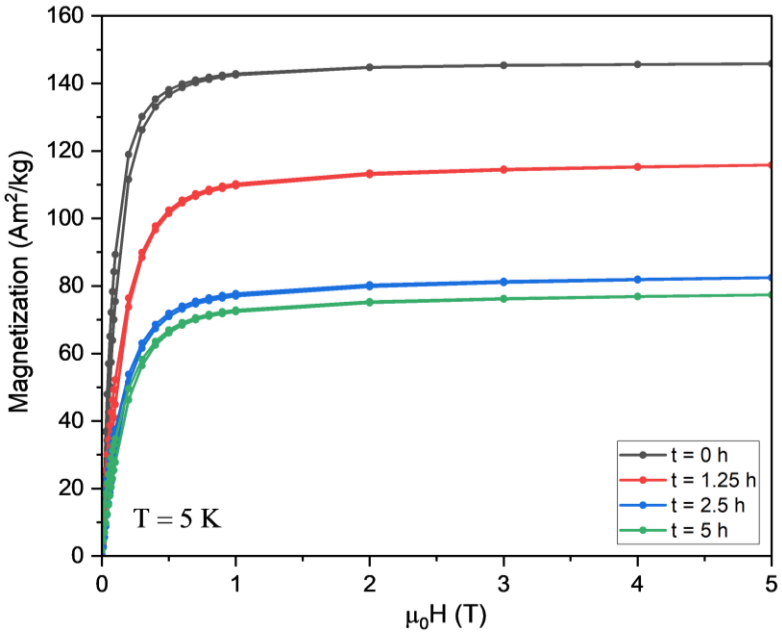

Figure 4.13 Field-dependent magnetization (M-H) curves at 5 K for $Mn_{0.65}Fe_{1.30}P_{0.65}Si_{0.37}$ samples with different ball-milling times.

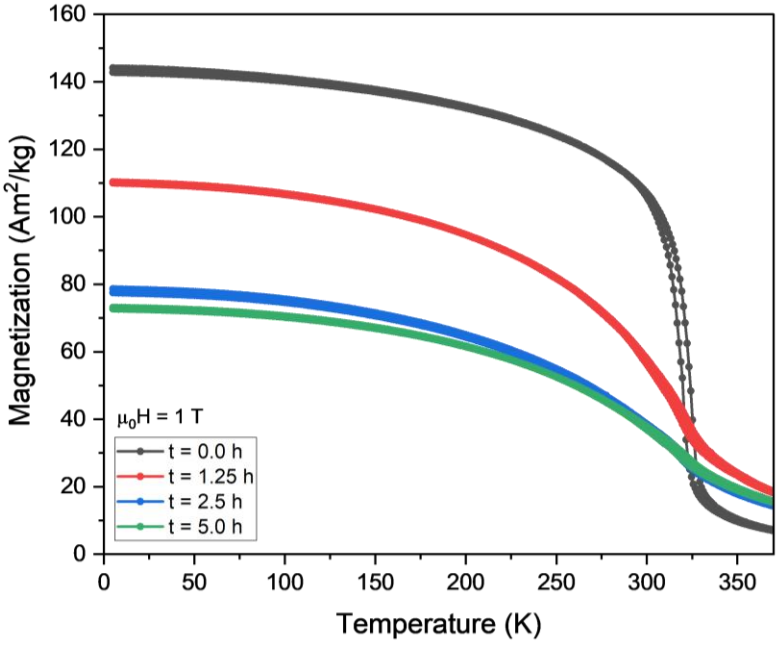

Figure 4.14 Temperature-dependent magnetization (M-T) curves at high field measurement (1 T) of $Mn_{0.65}Fe_{1.30}P_{0.65}Si_{0.37}$ sample with different ball-milling times.

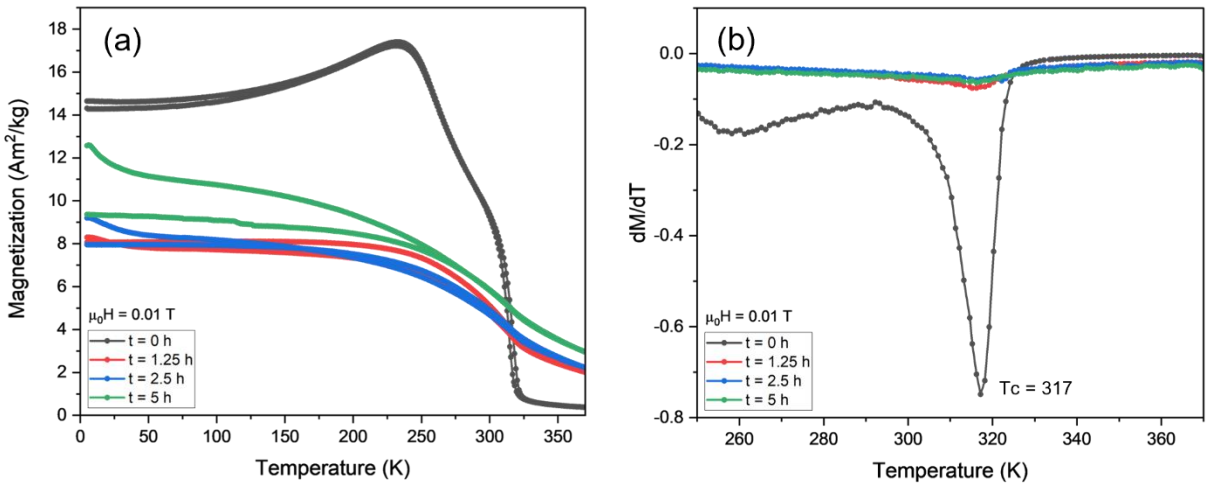

Figure 4.15 a) Temperature-dependent magnetization (M-T) curves at 0.01 T of $Mn_{0.65}Fe_{1.30}P_{0.65}Si_{0.37}$ sample with different ball-milling times, and **b)** The derivative of its magnetization (dM/dT) as a function of temperature.

Table 4.4 Properties of $Mn_{0.65}Fe_{1.30}P_{0.65}Si_{0.37}$ compounds with different ball-milling times.

BM time (h)	M_s (Am^2/kg)	Tc (K)	$Tc_{(Cooling)}$ (K)	$Tc_{(Heating)}$ (K)	ΔT_{hys} (K)
0	145.81	317	314	317	4
1.25	115.83	316	314	316	2
2.5	82.47	316	314	316	2
5	77.38	316	314	316	2

4.1.3.4. Magnetic Properties of $(Mn,Fe)_2(P,Si)$-based Compound at Different Compositions

According to the phase diagram of $Mn_xFe_{2-x}P_{1-y}Si_y$ system (**Figure 3.3**), which is used to determine the Curie temperature (T_c) of the synthesized magnetocaloric compound, further investigations were conducted on various $Mn_xFe_{2-x}P_{1-y}Si_y$ compositions to understand their dependence on the Curie temperature and thermal hysteresis (ΔT_{hys}). **Figure 4.16b** shows the temperature dependence of the magnetization (M-T curve) for $Mn_xFe_{2-x}P_{1-y}Si_y$ compounds with different compositions. While $Mn_{0.65}Fe_{1.30}P_{0.65}Si_{0.37}$ and $Mn_{0.75}Fe_{1.20}P_{0.60}Si_{0.39}$ exhibit slightly similar saturation magnetization at approximately 150 Am^2/kg, $Mn_{0.75}Fe_{1.20}P_{0.60}Si_{0.42}$ shows a lower saturation magnetization, approximately 121.88 Am^2/kg. This reduction is due to the higher Si content in this compound (Si content = 0.42) compared to the other compounds. It has been reported by Xinmin You that if the Si content is too high, it results in an increase in impurity phase and decrease in the phase fraction of the main phase, which negatively influences the magnetic properties [25]. All samples were fabricated using the same procedures but with different compositions and the summary of their magnetic properties are presented in **Table 4.5**. Among these, $Mn_{0.65}Fe_{1.30}P_{0.65}Si_{0.37}$ was found to have the most suitable composition, exhibiting a T_c of 316 K. $Mn_{0.75}Fe_{1.20}P_{0.60}Si_{0.39}$ shows the lowest ferromagnetic transition temperature at T_c = 307 K (34°C). Whereas the highest ferromagnetic transition temperature was observed in $Mn_{0.75}Fe_{1.20}P_{0.60}Si_{0.42}$, with a T_c of 355 K (82°C), which is too high for biomedical applications.

In addition, the Curie temperature (T_c) tends to increase with higher Si content. However, the obtained results indicate that the composition $Mn_{0.75}Fe_{1.20}P_{0.60}Si_{0.39}$, which has a higher Si content compared to $Mn_{0.65}Fe_{1.30}P_{0.65}Si_{0.37}$, exhibits a lower T_c. This may be attributed to the higher Mn:Fe atomic ratio which

may lead to a reduction in T_c [25]. Based on the results, $Mn_{0.75}Fe_{1.20}P_{0.60}Si_{0.39}$ (Mn:Fe ≈ 0.625) indeed has a higher in Mn:Fe atomic ratio in comparison to $Mn_{0.65}Fe_{1.30}P_{0.65}Si_{0.37}$ (Mn:Fe ≈ 0.5). However, with only three compositions studied, this trend cannot be conclusively proven. Furthermore, the hysteresis measurements revealed that $Mn_{0.75}Fe_{1.20}P_{0.60}Si_{0.39}$ exhibited the largest hysteresis (ΔThys = 17 K), followed by $Mn_{0.75}Fe_{1.20}P_{0.60}Si_{0.42}$ (ΔT_{hys} = 10 K) and $Mn_{0.65}Fe_{1.30}P_{0.65}Si_{0.37}$ (ΔT_{hys} = 5 K), respectively.

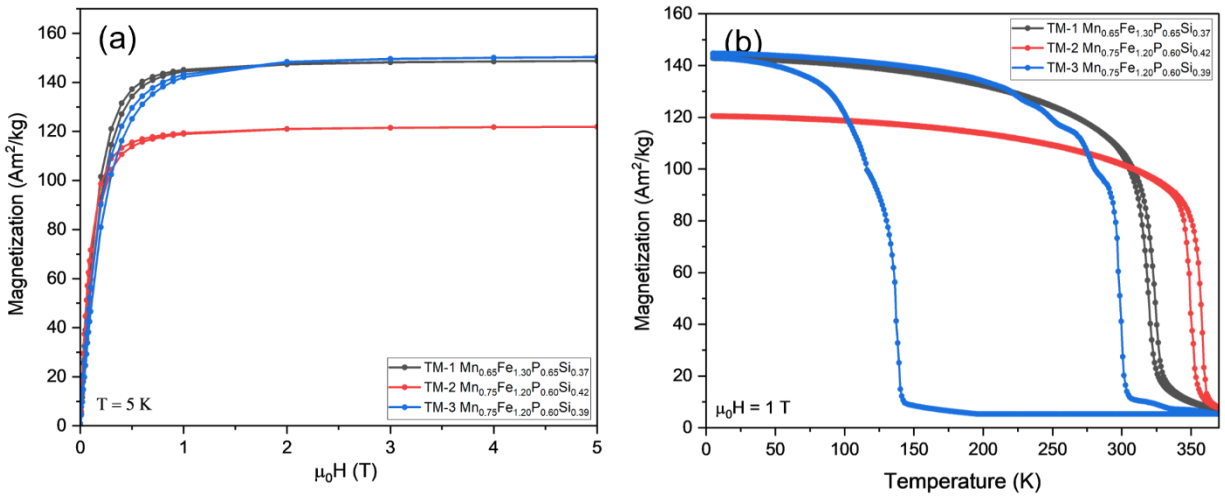

Figure 4.16 a) Isothermal field-dependent magnetization (M-H) curves at 5 K and **b)** Temperature-dependent magnetization (M-T) curves at 1 T of $(Mn,Fe)_2(P,Si)$-based compounds with different compositions.

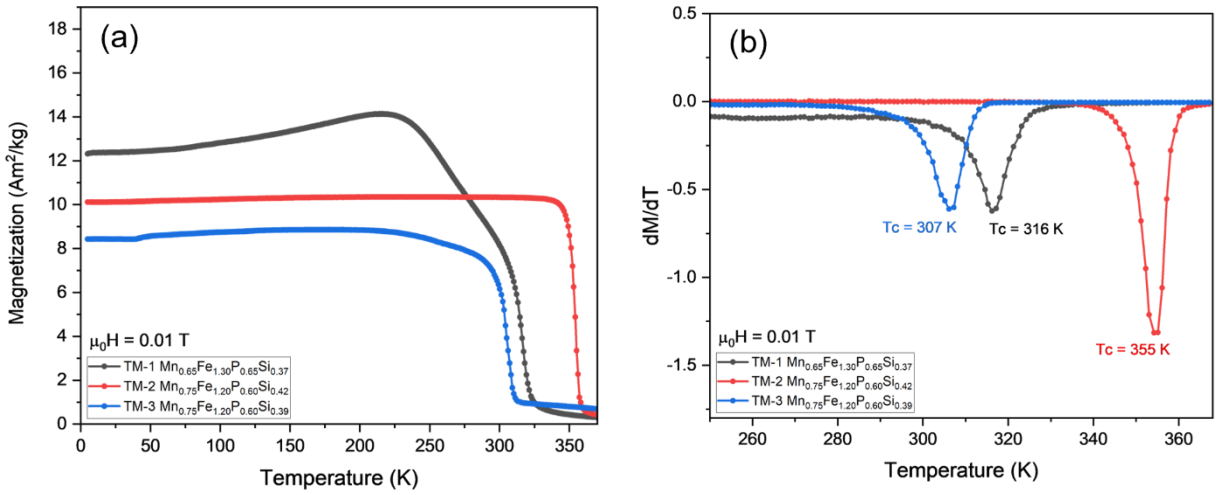

Figure 4.17 a) Temperature-dependent magnetization (M-T) curves at 0.01 T of $(Mn,Fe)_2(P,Si)$-based samples with different compositions, and **b)** The derivative of its magnetization (dM/dT) as a function of temperature.

Table 4.5 Properties of compounds from different compositions based on the phase diagram of $Mn_xFe_{2-x}P_{1-y}Si_y$ system.

No.	Mn Conc. (x)	Si Conc. (y)	M_s (Am^2/kg)	Tc (K)	$Tc_{(Cooling)}$ (K)	$Tc_{(Heating)}$ (K)	ΔT_{hys} (K)
TM-1	0.65	0.37	148.74	316	311	316	5
TM-2	0.75	0.42	121.88	355	345	355	10
TM-3	0.75	0.39	150.33	307	290	307	17

4.2. Part 2: Development and Characterization of Magnetocaloric Wax-based Composite

Before mixing the wax matrix with the magnetic particles, the melting point of each wax matrix with different bayberry wax (BBW) volume fractions was investigated. This step was necessary to select the composition of wax matrix with a melting point below the transition temperature of the magnetocaloric particles, ensuring that the wax matrix fully melts before the magnetocaloric particles reach their Curie temperature (T_c). The fabrication process for the wax matrix followed the procedure presented in **Figure 3.12**. The thermal behavior of the wax matrix was determined using Differential Scanning Calorimetry (DSC) measurements. The DSC curves, which plotted normalized heat flow (Q) as a function of temperature (°C), were used to determine the thermal parameters of the wax matrix. The second heating cycle was used for analysis, as the first heating cycle was eliminated to remove any thermal history effects.

4.2.1. Investigation of Melting Point of Wax Matrix: DSC Measurement

Figure 4.18 shows the DSC curves of pure bayberry wax and lanolin wax, providing reference data to evaluate the changes in thermal properties depending on the bayberry wax volume fraction. The DSC data for bayberry wax, shown in **Figure 4.18a**, clearly displays two endothermic peaks. These peaks indicate phase changes where the sample absorbs energy, causing it to melt. The multiple peaks observed may be due to the melting of different molar mass fractions of various chemical compositions within the wax, such as alcohols, fatty acids, and wax esters. The last peak at the end of the temperature range, where the wax is completely melted, represents the solid-liquid phase change of bayberry wax, with a melting temperature (T_m) of 55.90°C. The minor peak on the left side of the main peak may correspond to the initial melting of some components within the wax. In contrast, the DSC data for lanolin wax, shown in **Figure 4.18b**, exhibits non-pronounced peaks. This could be because lanolin wax has a low melting point and low enthalpy of fusion, or it could be due to an error during the DSC measurement process, as there are no reported thermal behaviors of pure lanolin wax. Therefore, the observed data for lanolin wax cannot be conclusively interpreted.

Figure 4.19 depicts the normalized heat flow of the second heating for all wax matrix samples fabricated in this project, ranging from 30, 32, 34, to 36 vol.% of bayberry wax. The thermal behaviors regarding their melting point, onset point, and enthalpy of fusion of wax matrices are summarized in **Table 4.6**. The enthalpy of fusion is a value measuring the energy input, typically heat, necessary to convert a substance from solid to liquid state. Each wax matrix was determined by integrating the area of the reaction peak and the interpolated baseline between the beginning and end of the reaction.

The melting point increases with the BBW fraction. The highest melting point was determined for the 36 vol.% BBW at 46.41°C, while the lowest melting point was observed for the matrix with 30 vol.% BBW at 42.51°C. Regarding the application of the wax matrix as a biodegradable membrane, the matrix with 30 vol.% BBW yielded the most favorable properties, with a melting point of 42.51°C. In addition to investigating the melting point of wax matrices with different bayberry wax volume fractions, the thermal behavior over time was also observed. The DSC curves shift towards higher temperatures with increasing BBW volume fraction, as shown in **Figure 4.19**. Multiple endothermic peaks were recorded for all samples.

These multiple peaks likely represent the melting of distinct phases, each of which can be single or multi-component, as the fabricated wax matrix is a combination of two different waxes. The existence of several peaks results from different chemical components within the wax melting at different temperatures. Mixture substances often show several peaks, and the endpoints of the melting transitions encompass the melting points of many major components, such as fatty acids and wax esters found in natural waxes [92]. With this reason, it is important to note that only a single temperature does not fully describe the thermal behavior.

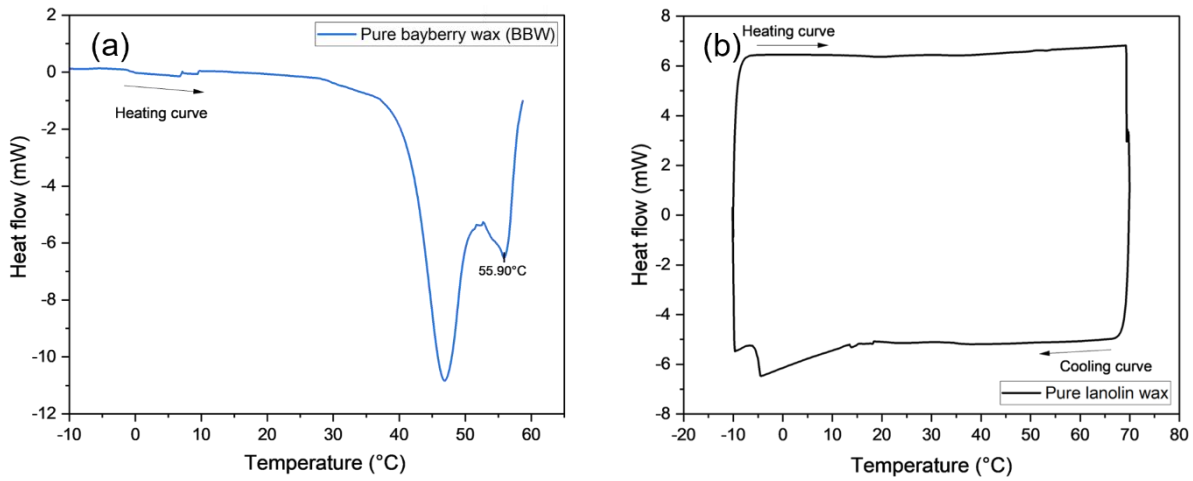

Figure 4.18 DSC measurement of **a)** pure bayberry wax and **b)** lanolin wax.

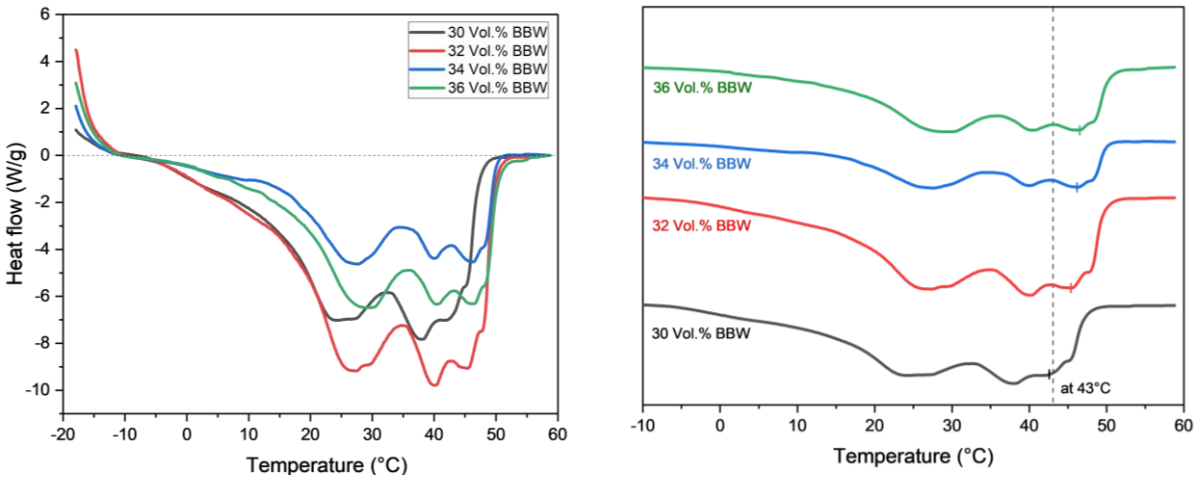

Figure 4.19 DSC curves for all max matrices of the second heat cycle. The normalized heat flow was investigated over the temperature range dependence of the BBW volume percentage, starting from 30 to 36 vol.-%.

Table 4.6 Thermal parameters of the different wax matrix composition varied in the volume of bayberry wax obtained from the DSC analysis.

BBW fraction (vol.-%)	Melting temperature (°C)	Enthalpy of fusion (J/g)
30	42.51	34.44
32	45.21	39.82
34	46.23	24.11
36	46.41	25.25
100 (pure BBW)	55.90	60.61

4.2.2. Characterization of Magnetocaloric Wax Composite

Before further investigating the thermal behavior of $Mn_{0.65}Fe_{1.30}P_{0.65}Si_{0.37}$ under an alternating magnetic field (AMF), the synthesized $Mn_{0.65}Fe_{1.30}P_{0.65}Si_{0.37}$ and other magnetic particles, namely CIP and Fe_3O_4, are initially mixed with water to serve as reference data. This step ensures that no exaggerated or abnormal changes in thermal effect occur when the magnetic particles are fabricated with the wax matrix. It is important to note that two batches of synthesized $Mn_{0.65}Fe_{1.30}P_{0.65}Si_{0.37}$ particles were used to fabricate the composite. The first batch, exhibiting a T_c of 317 K, was mixed with the wax matrix, with the magnetocaloric particles (MCM) volume percentage ranging from 10, 15, 20, and 25 vol.%. The second batch, exhibiting a T_c of 313 K, was dispersed with strong water, also with varying MCM volume percentages. The strong water is made by mixing water with starch, making it more viscous than normal water and facilitating better magnetic particle dispersion.

The transition temperature of the 2nd batch was investigated to ensure that, after mixing with wax and water to create the composite, their T_c remained unchanged. The transition temperature, based on the derivative dM/dT under a low magnetic field (0.01 T), is shown in **Figures 4.20b**. The transition temperatures of the magnetocaloric dispersed in water is 313 K, indicating that its T_c remains the same as that obtained from pure magnetocaloric particles examined in **Section 4.1**.

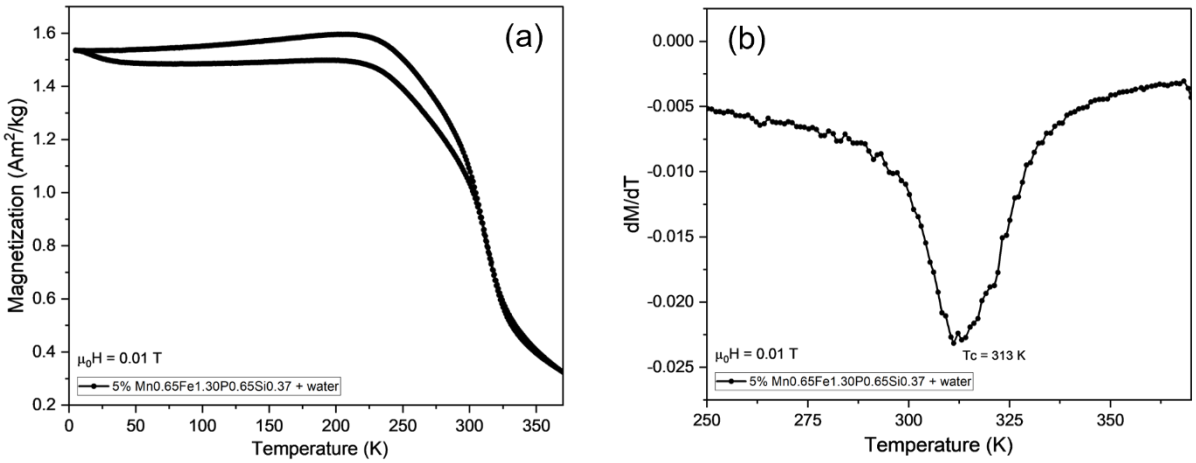

Figure 4.20 a) Temperature-dependent magnetization (M-T) curve at 0.01 T of the sample with 5 vol.% of $Mn_{0.65}Fe_{1.30}P_{0.65}Si_{0.37}$ particles (MCM) dispersed with water, and **b)** The derivative of its magnetization (dM/dT) as a function of temperature.

4.2.2.1. Inductive Heating under Alternating Applied Magnetic Field (AMF)

The desired properties of magnetic composite for biodegradable membranes are that it should serve as a heating agent to efficiently melt the wax matrix, enable cross-interaction between cell cultures on the chip at the appropriate time, and also stop heating within the therapeutic range of 42-47°C to prevent overheating issues. In this study, transition temperature (T_c) is used as the threshold temperature to stabilize and maintain the temperature within a safe range, as once the magnetic particle exceeds its T_c, the magnetization will decrease to near zero, decreasing the heating efficiency to approximately zero.

The inductive heating experiment was conducted to assess the heating behavior of the composite, considering three types of magnetic particles ($Mn_{0.65}Fe_{1.30}P_{0.65}Si_{0.37}$ (MCM), CIP, and Fe_3O_4) with 4 values of particle volume percentage (10, 15, 20, and 25 vol.%). Three values of the applied field amplitudes (2.5, 10, and 15 mT) and the frequency at 244 kHz were used for all conditions.

All recordings included a temperature equilibration period prior to recording, an exposure time before turning on the field strength (60 s), and a between-exposure time when starting to turn on the field strength. There was no consistent exposure profile that could be defined for all experimental conditions. Due to safety concerns with the machine, to prevent overheating, which may occur if the temperature reaches over 100°C, the field strength was turned off when either (1) the set exposure time period had been reached (10-15 min) or (2) the temperature increased over 90°C.

Heating Behavior of Magnetic Particles Dispersed in Water under Different AMF Fields

Figure 4.22 displays the effect of different magnetic field strengths (2.5, 10, and 15 mT) on the temperature variations of three distinct magnetic composites ($Mn_{0.65}Fe_{1.30}P_{0.65}Si_{0.37}$ (MCM), CIP, and Fe_3O_4). Each sample with a 15 vol.% of magnetic particles was dispersed in strong water. It was found that magnetic field amplitudes have a strong influence on the increase in temperature change. When exposed to a magnetic field of 2.5 mT, none of the three types of magnetic particles exhibited a significant temperature rise. This indicates that a magnetic field strength of 2.5 mT is too low to induce sufficient magnetic hysteresis losses in the particles to generate heat. In contrast, when all three magnetic samples were subjected to an AMF at 15 mT, the temperature of all samples continued to rise uncontrollably over the exposure time.

Focusing on subjected magnetic samples under a magnetic field of 10 mT, the MCM and Fe_3O_4 samples exhibited more gradual temperature increases compared to the CIP sample. The temperature evolution of the samples during AMF exposure can be divided into three main stages: (I) a significant increase in temperature at the initial stage, (II) a slight increase in temperature before reaching a consistent level, and (III) maintaining a consistent temperature until the end of AMF exposure. The change in temperature over the AMF exposure time of the 15 vol.% MCM sample is presented in **Figure 4.21**. It is clearly seen that the MCM sample showed an initial linear temperature rise, reaching over its T_c at 40°C within 5 min. Once it reached its transition temperature (T_c) at 40°C (indicated by a black dashed line), it started to stabilize at approximately 45°C and maintained this temperature until the end of the 15-min exposure period. It is expected that, even with the AMF continuously turned on, the temperature will be able to remain stabilized around 44-45°C. This is because the heating rate is relatively slow; the temperature rises from 40°C to the endpoint of the exposure time at 44°C, the rate is only 0.014°C/min. This observed result aligns with the heating rate (dT/dt) during the temperature rise. As shown in **Figure 4.22a**, the heating rate of the MCM sample began to decrease after surpassing its T_c when subjected under 10 mT field. This trend is also observed in **Figure 4.22b**, where a 15 mT magnetic field was used. However, the heating rate under the 15 mT magnetic field is higher than that under the 10 mT field. This gradual decrease in heating rate is due to the phase transition that occurs at the Curie point, where ferromagnetic materials become paramagnetic. This transition results in a reduction in magnetic susceptibility, making the magnetic sample less responsive to the applied magnetic field.

Moreover, considering the exposure time required for the samples to reach the melting point of the wax matrix at 42°C (T_m, marked by a red dashed line), the MCM sample required 6 min when subjected to a magnetic field of 10 mT and only 0.98 min under 15 mT to reach this temperature and completely liquefy

the wax composite. In contrast, the Fe_3O_4 sample barely reached 40°C even after 15-min exposure to a 10 mT magnetic field and took 2 min under 15 mT, which is longer than the MCM sample. The CIP sample exhibited the fastest heating rate in reaching the wax melting point. It can reach 42°C within 3 min under a 10 mT and only 0.73 min under a 15 mT field. Although the CIP sample exhibited higher heat efficiency, its inconsistent temperature rise makes it difficult to control within the therapeutic range (42-47°C).

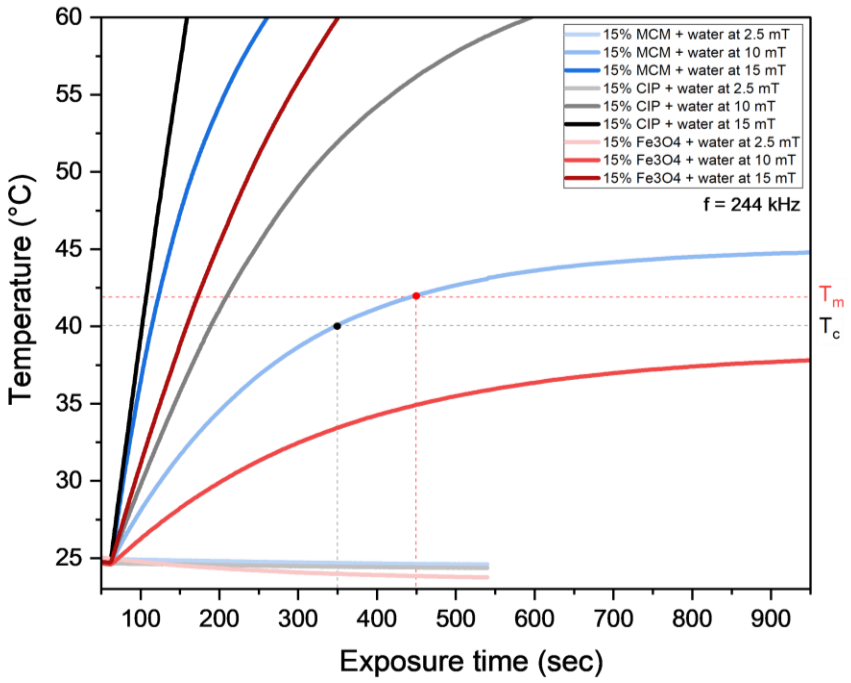

Figure 4.21 Evolution of the temperature observed in three types of magnetic samples dispersed in water, each with 15 vol.% of different magnetic particles ($Mn_{0.65}Fe_{1.30}P_{0.65}Si_{0.37}$ (MCM), CIP, and Fe_3O_4).

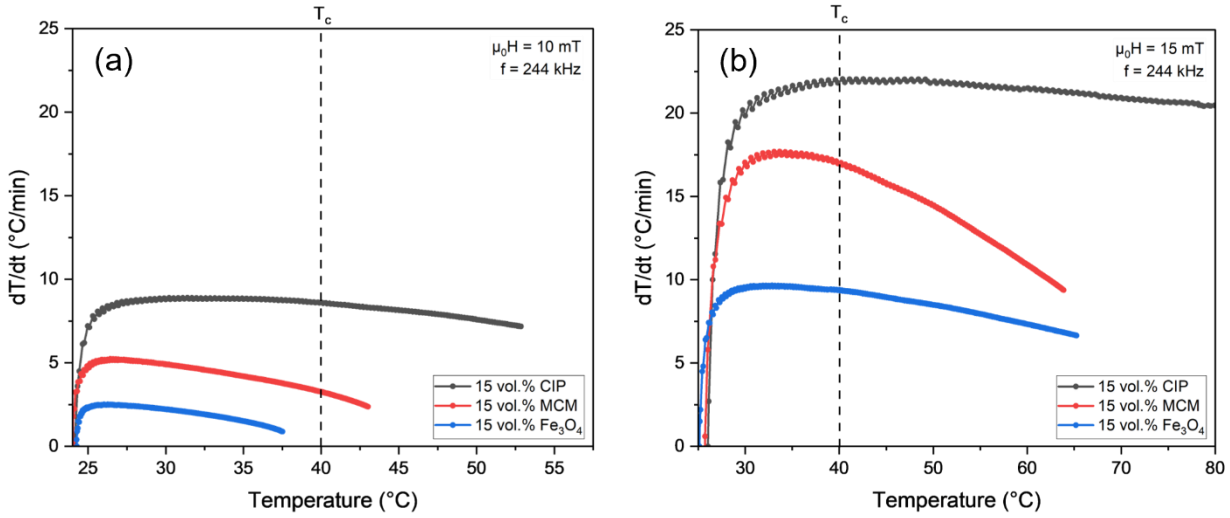

Figure 4.22 The heating rate (dT/dt) observed in three types of magnetic samples dispersed in water, each with 15 vol.% of different magnetic particles ($Mn_{0.65}Fe_{1.30}P_{0.65}Si_{0.37}$ (MCM), CIP, and Fe_3O_4) under a magnetic field of **a)** 10 mT and **b)** 15 mT.

Specific Loss Power (SLP) Value Analysis

Under a 10 mT field, it is observed that the Fe_3O_4 sample exhibits lower temperature rise compared to MCM sample. This phenomenon may be attributed to the lower heat-generating efficiency of Fe_3O_4 particles compared to the MCM and CIP samples. This can be confirmed by Specific Loss Power (SLP) value, which is the ability of magnetic particles to dissipate the energy of an external alternating magnetic field. In other words, SLP represents the capacity of magnetic particles to release heat to the surrounding environment when exposed to an AMF. The formula used to calculate SLP (W/kg) is given in **Eq. 4.1**, Where C_s is the specific heat capacity of the fluid in which magnetic particles are suspended [93] (for water, C_s = 4186 J/kg °C), m_s is the mass of the sample, m_p is the mass of magnetic particles in the 1 ml composite, and dT/dt (°C/s) is the initial temperature rising rate, defined as the moment of a few seconds (30 s) after starting the heating.

$$SLP = C_s \frac{\Delta T}{\Delta t} \frac{m_s}{m_p} \quad \textbf{(Eq. 4.1)}$$

The SLP values of different magnetic samples with 15 vol.% of magnetic particle when subjected under a magnetic field of 10 and 15 mT were estimated and presented in **Table 4.7**. Higher SLP indicates that magnetic particles can generate more heat per unit mass when exposed to an alternating magnetic field. Based on the calculation, the estimated SLP value of the Fe_3O_4 sample is low compared to the CIP and MCM samples.

Table 4.7 Summary of parameters obtained from the temperature rise of the samples with 15 vol.% of magnetic particles dispersed in the strong water when subjected under the magnetic field of 10 and 15 mT at fixed frequency = 244 kHz.

Experimental condition	Time needed to reach melting temperature 42°C (min)	dT/dt (°C/s)	m_s/m_p	SLP (W/kg)
At μ_0H = 10 mT				
CIP $_{15\ vol.\%}$	1.87	0.13	1.85	967
MCM $_{15\ vol.\%}$	6.4	0.08	1.95	663
Fe_3O_4 $_{15\ vol\%}$	-	0.04	2.31	397
At μ_0H = 15 mT				
CIP $_{15\ vol.\%}$	0.73	0.16	1.85	2786
MCM $_{15\ vol.\%}$	0.98	0.30	1.95	2432
Fe_3O_4 $_{15\ vol\%}$	2.05	0.36	2.31	1542

Overall, it has been found that with the same magnetic concentration (15 vol.% of magnetic particles), increasing the magnetic field amplitudes results in a faster temperature rise and an increased heating rate. Among the three types of magnetic samples, the MCM sample holds promise as a heating agent for biodegradable membranes. The MCM sample's ability to maintain a controlled temperature within the therapeutic range, combined with its heat efficiency, ensures that it can efficiently melt the wax composite without causing any damage to living cells, even with the magnetic field turned on.

Heating Behavior of Magnetic Wax Composite under AMF Field of 2.5 mT

To characterize the heating efficiency of the magnetic wax composites, induction heating tests were conducted to investigate the effect of varying concentrations of magnetic particles (10, 15, 20, and 25 vol.%) on the temperature rise under different AMF intensities (2.5, 10, and 15 mT). The initial magnetic heating experiments were performed under an AMF intensity of 2.5 mT at a fixed frequency of 244 kHz, as shown in **Figure 4.23**. Similar to the results obtained with magnetic particles dispersed in strong water, none of the three types of magnetic particles ($Mn_{0.65}Fe_{1.30}P_{0.65}Si_{0.37}$ (MCM), CIP, and Fe_3O_4) exhibited a significant

temperature rise. A closer observation of the temperature range between 60 to 200 s revealed that while Fe_3O_4 samples showed no change in temperature rise, even with increased concentration from 10 to 25 vol.%, MCM and CIP samples exhibited a slight increase in temperature over exposure time as the concentration of magnetic particles increased. It is evident that a magnetic field strength of 2.5 mT is insufficient to induce significant hysteresis losses in the particles to generate substantial heat. Therefore, further investigations will focus on higher field strengths, and the 2.5 mT intensity will be excluded from the scope of interest.

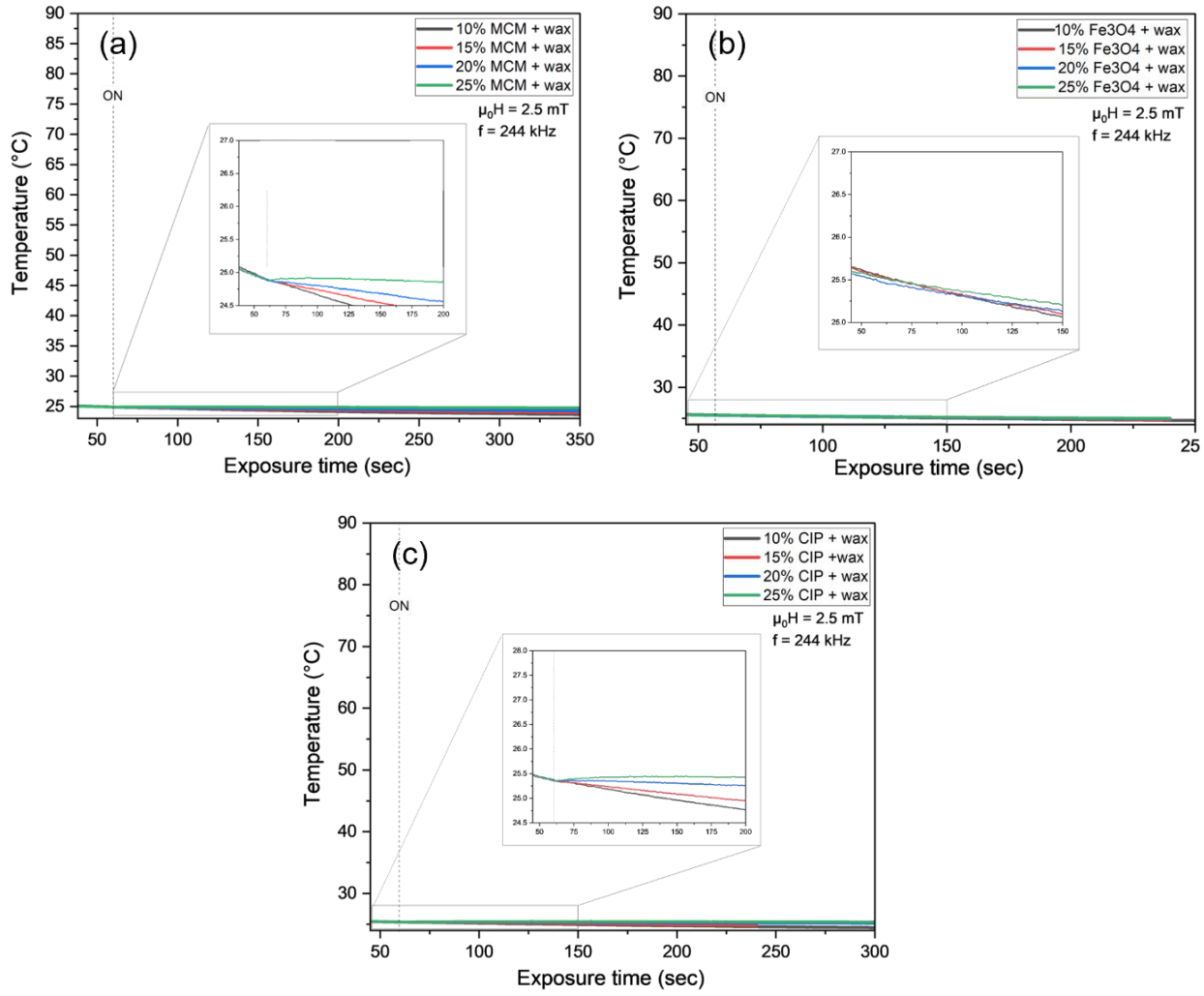

Figure 4.23 Heating behavior of **a)** $Mn_{0.65}Fe_{1.30}P_{0.65}Si_{0.37}$ particles, **b)** Fe_3O_4, and **c)** CIP with different volume percentage (10, 15, 20, and 25 vol.%) when subjected under magnetic field of 2.5 mT.

Heating Behavior of Magnetic Wax Composite under AMF Field of 10 and 15 mT

The induction heating tests of different magnetic samples conducted under AMF at 10 and 15 mT and their heating behaviors over exposure time were presented in **Figure 4.24**. Overall, the results indicate a clear trend where the rise in temperature is significantly larger when magnetic concentrations and magnetic field amplitude increase.

The results of the MCM samples with various magnetic particle concentrations when subjected to a magnetic field of 10 and 15 mT are presented in **Figure 4.24a** and **Figure 4.24b**, respectively. These results illustrate how different concentrations of magnetic particles influence the heating behavior and heating

efficiency of the samples. Under 10 mT field, the MCM sample with 10 vol.% particles exhibited a gradual increase in temperature and stabilized around 35°C, suggesting that this concentration may be insufficient to generate and dissipate enough heat. When the MCM concentration was increased to 15 vol.%, the temperature reached over its T_c at 43°C within 6 min. After surpassing T_c, it remained constant at 47°C until the end of the 15-min exposure period. The heating rate of the MCM samples, starting from 43°C onwards to the saturated temperature at the end of the exposure period, was 0.511°C/min. However, at higher concentrations of MCM particles (20 and 25 vol.%), the samples quickly exceeded the transition temperature within 3 and 2 min, respectively, before stabilizing at 55°C and 58°C. The observed trend of higher temperature rise with increasing particle concentration may be attributed to increased particle-particle interactions. As the concentration of magnetic particles increases, the exchange coupling energy also rises, thereby enhancing the efficiency of the induction heating test [13]. Therefore, even if the samples already exceeded their T_c, they may require more time for the magnetic particles to relax back or stop responding to the magnetic field. Overall, the results demonstrate that utilizing the Curie temperature (T_c) allows magnetic particles to self-regulate their temperature effectively. The MCM sample started to maintain a stable temperature once it exceeded their Tc, highlighting their suitability for applications requiring precise thermal control. This self-regulation is critical for maintaining controlled temperature changes, ensuring the safe and efficient use of MCM particles in applications requiring precise thermal management.

Under a magnetic field of 10 mT (**Figure 4.24c**), Fe_3O_4 samples exhibited a consistent temperature rise but required more exposure time and higher particle concentrations (up to 20-25 vol.%) compared to MCM samples to fully melt the wax matrix. It took over 10 min for the sample with 20 vol.% Fe_3O_4 particles and 6 min for the 25 vol.% Fe_3O_4 sample to reach 42°C. In contrast, under a 10 mT magnetic field (**Figure 4.24e**), the CIP samples reached the melting point of wax within only 60 s for all magnetic particle concentrations (10-25 vol.%), demonstrating the highest heating efficiency to melt the wax. However, their rapid and uncontrolled temperature rise made it difficult to stabilize the temperature within the therapeutic range. These findings highlight the challenges of using Fe_3O_4 and CIP samples for applications requiring precise thermal management. While Fe_3O_4 requires longer exposure times and higher particle concentrations, CIP exhibits rapid heating but lacks control over temperature stabilization.

The investigation regarding the influence of magnetic field amplitudes on the heating behavior of the samples showed that, for all magnetic samples, although an increase in the magnetic field from 10 mT to 15 mT resulted in greater heat-generating performance, it was difficult to maintain a controlled and safe temperature range. This makes the 15 mT field too high as a setting parameter for heating biodegradable membranes, where precise thermal management is crucial for safe and effective operation. These findings emphasize the need to optimize magnetic field amplitudes to achieve a balance between heating efficiency and temperature control, particularly in applications requiring strict thermal control.

Heating Rate Analysis

The heating rate (dT/dt) over temperature rise for magnetic samples with 15 vol.% particles under 10 mT field are shown in **Figure 4.25a**. The MCM sample shows a similar decrease in heating rate once it surpasses its transition temperature at 43°C, corresponding to the consistency of temperature evolution after exceeding the transition temperature demonstrated in **Figure 4.24a**. While the Fe_3O_4 sample also exhibits a gradual decrease in heating rate similar to what observed in the MCM sample, the CIP sample exhibits an initial slight decrease in heating rate followed by a fluctuating increase in heating rate. This fluctuation appears to occur when the temperature surpasses the melting point of the wax composite at 42°C. Due to the structural properties of the wax, during its phase change transition from solid to liquid, the wax absorbs a significant amount of thermal energy from its surroundings, which is produced by the magnetic particles. This energy is used to break the molecular bonds that hold the solid structure together. The absorption of energy at the melting point may slow down the rate of temperature increase. Once the wax is fully liquefied, the absence of the need to absorb latent heat leads to a more rapid increase in temperature. This phase change behavior explains the initial slight decrease in heating rate followed by a fluctuating increase observed in the CIP sample. This phenomenon was also observed with the Fe_3O_4 and MCM samples under a magnetic field of 15 mT (**Figure 4.25b**), resulting in a slight increase in heating rate before stabilizing.

The heating rate (dT/dt) for magnetic samples with 15 vol.% particles under 15 mT field is studied and presented in **Figure 4.25b**, it is clearly seen that the heating rate of the magnetic samples increases with the magnetic field amplitude, resulting in faster heating generation. Under a magnetic field of 15 mT, the Fe_3O_4 sample exhibits a slight drop in heating rate around the temperature where the phase change of wax occurs and then starts to increase after passing that range before maintaining a constant change in heating rate until the end of the exposure time. This means that the temperature will consistently increase over exposure time, which is confirmed by the significant temperature rise observed in **Figure 4.24d**.

The MCM sample also shows an increase in heating rate after the melting point. However, due to the effect of the transition temperature, the heating rate starts to drop gradually once T_c is reached. Therefore, the temperature rise over exposure time observed in **Figure 4.24b** appears to be slower in comparison with the Fe_3O_4 sample once it surpasses the melting point. In contrast, the CIP sample exhibits an uncontrollably sharp and fluctuating heating rate once it reaches the melting temperature of the wax matrix.

In addition, it is observed that by being given the same amount of magnetic particles and the same applied magnetic field, the wax composite's heating rate (dT/dt) is larger than that when dispersed in strong water. This may be due to the specific heat capacity of wax, calculated based on DSC data (approximately 560 J/(kg °C) at 25°C), is lower than that of water (4186 J/(kg °C) at 25°C).

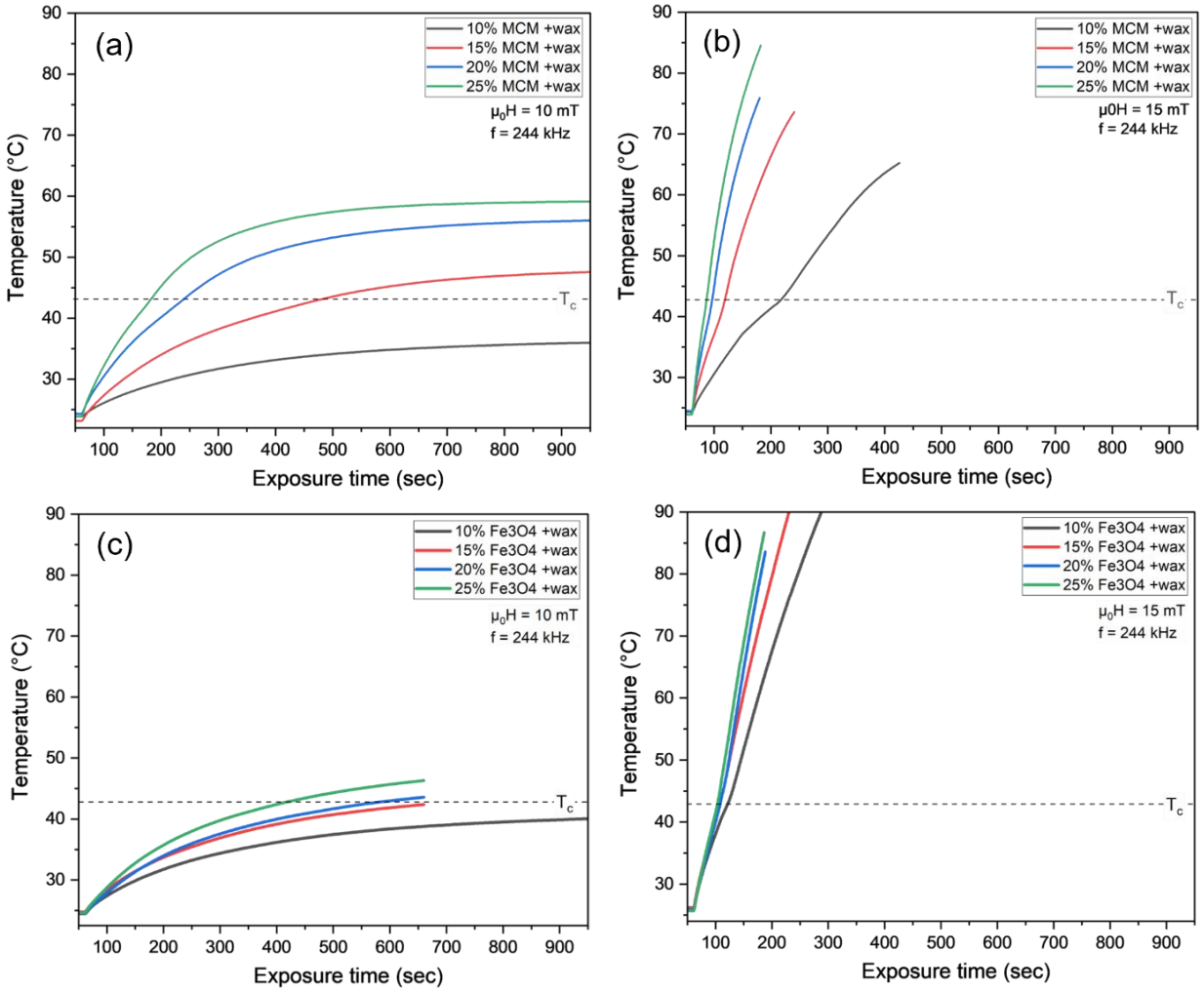

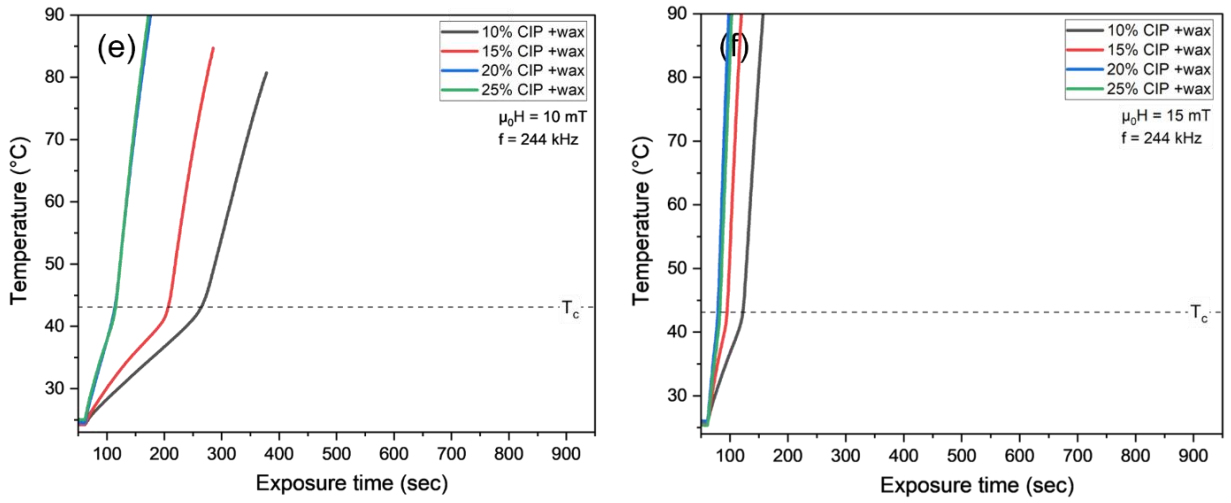

Figure 4.24 Heating behavior of a-b) $Mn_{0.65}Fe_{1.30}P_{0.65}Si_{0.37}$ particles, c-d) Fe_3O_4, and e-f) CIP with different volume percentage (10, 15, 20, and 25 vol.%) when subjected to magnetic field strength of 10 and 15 mT.

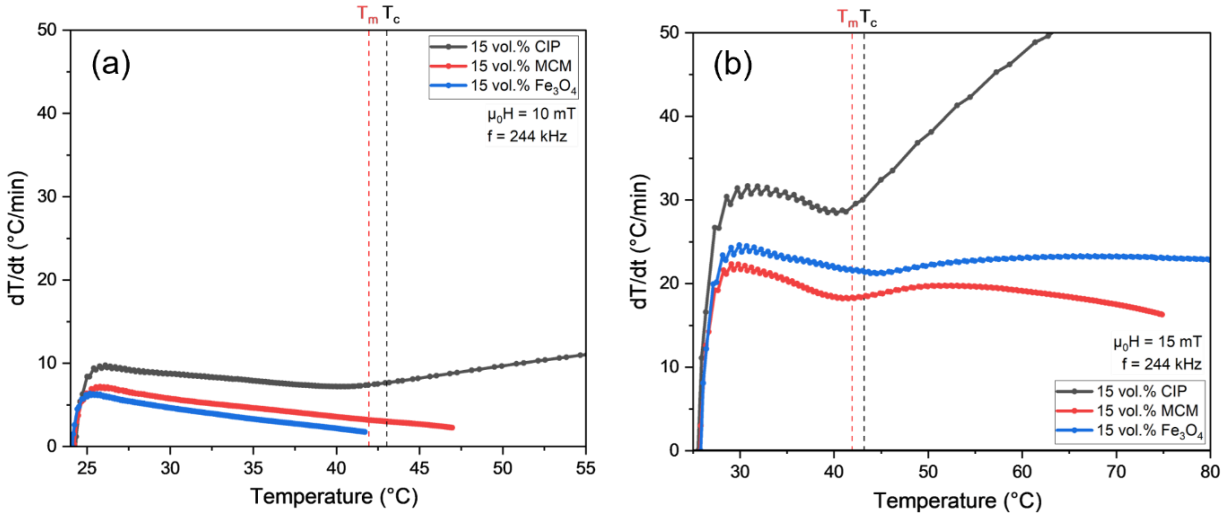

Figure 4.25 The heating rate (dT/dt) estimated from magnetic samples with 15 vol.% particles dispersed in wax, each with 15 vol.% of different magnetic particles ($Mn_{0.65}Fe_{1.30}P_{0.65}Si_{0.37}$ (MCM), CIP, and Fe_3O_4) under a magnetic field of **a)** 10 mT and **b)** 15 mT.

Heating Capabilities of Magnetocaloric Wax Composite in Melting Wax Matrix

Regarding the heating capabilities of magnetic particles to melt the wax, based on the DSC data observed in the 30 vol.% BBW wax matrix used in this study, it begins to melt at 30°C and is fully liquefied at 42°C. The duration required to reach melting temperature of wax for all experiment conditions is summarized in **Table 4.8**. Concerning the MCM sample, the time required for the 15 vol.% MCM sample to fully melt the wax matrix under 10 mT field was 6 min, while the 20 and 25 vol.% MCM samples took only 3 and 2 min, respectively. This confirms that higher concentrations of magnetic MCM particles demonstrate higher heat generation efficiency, resulting in faster melting of the wax. When subjected to a magnetic field of 15 mT, the 15 vol.% MCM sample exhibits strong heating efficiency and begins to liquefy the wax faster within 0.87 min, which is 7 times higher than under 10 mT field, indicating that increasing the magnetic field strength significantly enhances the heat generation and efficiency of the MCM samples, leading to quicker melting of the wax matrix.

Although the MCM samples with higher magnetic particle concentrations (20 and 25 vol.%) exhibited greater heat-generating efficiency compared to the 15 vol.% MCM sample and showed the capability to stabilize their temperature upon reaching T_c, it might be difficult to control and stabilize the temperature within the safety range (<47°C), thereby increasing the risk of damaging living cells. Additionally, with higher magnetic particle concentrations, they also make the composites denser and stickier, complicating mixing and potentially leading to cracking and poor injectability of the membrane to the chip platform.

Specific Loss Power (SLP) Value Analysis

The SLP values of different magnetic samples with varying particle concentrations (10, 15, 20, and 25 vol.%) under a magnetic field of 10 and 15 mT at a frequency of 244 kHz are estimated and presented in **Figure 4.26**. The specific heat capacity of the wax matrix was calculated based on DSC data, C_s = 560 J/(kg °C). The initial temperature rising rate (dT/dt) was defined °C/s for 30 s after starting the heating. Overall, it was found that increasing the magnetic field strength from 10 mT to 15 mT results in an increase in SLP values for all samples. A summary of parameters used to determine SLP values is presented in **Table 4.8**.

The estimated SLP values of the Fe_3O_4 sample show a gradual slight decrease over the particle concentration. This trend is similar to that observed in other studies [94], where the SLP of Fe_3O_4 particles tends to decrease at higher concentrations for experiments conducted at a frequency of 210 kHz. A decrease in SLP with increasing concentrations indicates that the magnetic particles are generating less heat per unit mass. It was observed that heating rate (dT/dt) has a strong influence on the SLP values. For example, the SLP values of the Fe_3O_4 sample under a 10 mT field shows that even with increased amounts of magnetic particles at higher concentrations, the heating rates do not increase proportionally, remaining constant at only around 0.1°C/s. This suggests that in practice, beyond a certain concentration, adding more particles does not significantly enhance heating efficiency, which is why the sample with 10 vol.% Fe_3O_4 particles shows the highest SLP value, indicating this is the optimal concentration for maximizing heating efficiency for this specific experimental condition.

On the other hand, as shown in **Figure 4.26**, although the SLP value of CIP samples significantly increases from 10 vol.% to 20 vol.%, the SLP starts to drop at 25 vol.% of magnetic particles. Considering its heating rate (dT/dt), it was found that when the heating rates remain more or less the same as the concentrations increase, the SLP values do not show a significant increase and may even decrease with higher magnetic concentrations. However, when there is a significant increase in heating rate, as observed in the CIP sample under a 10 mT magnetic field from 0.15°C/s for the 15 vol.% CIP sample to 0.33°C/s for the 25 vol.% CIP sample, there is also a corresponding significant increase in SLP values. The SLP values of MCM samples also reflect the strong influence of heating rate, as with the increase in magnetic concentrations, the heating rate increases proportionally, resulting in a constant increase in SLP values over magnetic particle concentrations. This trend could be beneficial for applications requiring sustained and efficient heating.

It is important to note that the purpose of the SLP values is to determine magnetic particles with higher heating efficiency at low concentrations. They serve as a measure of heating efficiency for magnetic particles in hyperthermia treatments [95]. Therefore, it is crucial to minimize the amount of magnetic particles used in the human body to easily extract after post-treatment, prevent overheating issues that could arise from high particle concentrations and reduce potential side effects or toxicity. However, at the same time, the particles must generate sufficient heat to efficiently kill cancer cells. Thus, further research into the optimal concentration of developed magnetocaloric (MCM) particles is valuable. Its insights may show the potential advantages of $(Mn,Fe)_2(P,Si)$-based particles in not only achieving tunable self-regulation but also exhibiting high heating efficiency at proper particle concentrations. This could be particularly beneficial in developing new therapeutic techniques and other applications requiring precise temperature control.

In summary, the 15 vol.% MCM sample holds promise as a heating agent for biodegradable membranes due to its consistent and controllable temperature rise. The MCM sample's ability to maintain a controlled temperature within the therapeutic range, combined with its heat efficiency, ensures that it can efficiently melt the wax composite without causing any damage to living cells, even with the magnetic field turned on.

It is important to note that although the 15 vol.% MCM sample under 15 mT exhibited higher heat efficiency, its inconsistent temperature rise makes it difficult to control within the therapeutic range (42-47°C). Therefore, the 15 vol.% MCM sample will be further investigated regarding the influence of magnetic field strengths in the range of 5-10 mT.

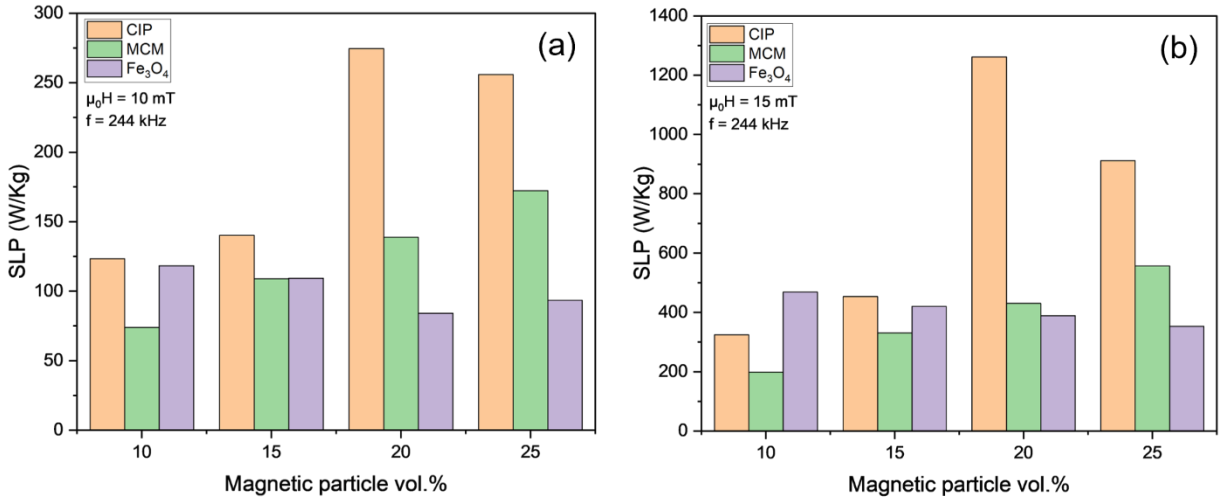

Figure 4.26 The SLP values calculated from three distinct types of magnetic samples dispersed in wax, each with volume fraction of different magnetic particles ($Mn_{0.65}Fe_{1.30}P_{0.65}Si_{0.37}$ (MCM), CIP, and Fe_3O_4) when subjected under a magnetic field of **a)** 10 mT and **b)** 15 mT.

Table 4.8 Summary of parameters obtained from the temperature variations of magnetic wax composites when subjected to the magnetic field of 10 mT and 15 mT at fixed frequency = 244 kHz.

Experimental condition	Time needed to reach melting temperature 42°C (min)	dT/dt (°C/s)	m_s/m_p	SLP (W/kg)
At μ_0H = 10 mT				
CIP $_{10\ vol.\%}$	3.28	0.11	2.09	123.37
CIP $_{15\ vol\%}$	2.40	0.15	1.69	140.25
CIP $_{20\ vol.\%}$	0.87	0.33	1.48	274.60
CIP $_{25\ vol.\%}$	0.86	0.34	1.36	255.86
MCM $_{10\ vol.\%}$	-	0.06	2.23	73.96
MCM $_{15\ vol.\%}$	6.23	0.11	1.77	108.94
MCM $_{20\ vol.\%}$	2.75	0.16	1.55	138.79
MCM $_{25\ vol.\%}$	1.88	0.22	1.41	172.34
Fe_3O_4 $_{10\ vol.\%}$	-	0.08	2.69	118.34
Fe_3O_4 $_{15\ vol.\%}$	9.28	0.10	2.06	109.37
Fe_3O_4 $_{20\ vol.\%}$	7.70	0.09	1.75	84.14
Fe_3O_4 $_{25\ vol.\%}$	5.38	0.11	1.56	93.42
At μ_0H = 15 mT				
CIP $_{10\ vol.\%}$	1.00	0.23	2.09	324.43
CIP $_{15\ vol\%}$	0.57	0.48	1.69	453.23
CIP $_{20\ vol.\%}$	0.32	1.52	1.48	1261.88
CIP $_{25\ vol.\%}$	0.37	1.19	1.36	911.94

MCM $_{10\ vol.\%}$	2.50	0.16	2.23	198.62
MCM $_{15\ vol.\%}$	0.87	0.33	1.77	330.79
MCM $_{20\ vol.\%}$	0.53	0.50	1.55	430.49
MCM $_{25\ vol.\%}$	0.43	0.71	1.41	557.26
Fe_3O_4 $_{10\ vol.\%}$	0.95	0.31	2.69	468.84
Fe_3O_4 $_{15\ vol.\%}$	0.73	0.36	2.06	420.14
Fe_3O_4 $_{20\ vol.\%}$	0.75	0.40	1.75	388.73
Fe_3O_4 $_{25\ vol.\%}$	0.68	0.40	1.56	353.26

Heating Behavior of 15 vol.% of Magnetocaloric Wax Composite under Various AMF Field

The influence of the applied magnetic field on the heating efficiency for a 15 vol.% $Mn_{0.65}Fe_{1.30}P_{0.65}Si_{0.37}$ (MCM) sample is illustrated in **Figure 4.27**. The results indicate that, with the same particle concentrations, the temperature tends to increase over exposure time as the magnetic field strength increases from 5 to 10 mT. This demonstrates that the magnetic field amplitude has a strong influence on the temperature rise. As shown in **Figure 4.27a**, the MCM sample with 15 vol.% particles, when subjected to 5-8 mT magnetic fields, exhibited a gradual rise in temperature and started to stabilize before it reached T_c at 43°C. This suggests that this field strength may be insufficient to generate and dissipate enough heat.

When exposed to a magnetic field of 10 mT, the MCM sample exhibited a trend comparable to those observed in **Figure 4.24a**. The temperature remained constant at around 48°C for 6 min until the end of the 15-minute exposure period. As shown in **Figure 4.27b**, the faster heating rate of the MCM sample under 10 mT showed a decrease in heating rate once it surpassed its transition temperature at 43°C. On the other hand, when exposed to a magnetic field of 9 mT, the sample started to stabilize at approximately 44°C after it reached its transition temperature (T_c) at 43°C and maintained this temperature until the end of the 15-min exposure period. The heating rate is slow; the temperature rises starting from 43°C to the endpoint of the exposure time at 47°C at a rate of only 0.53°C/min.

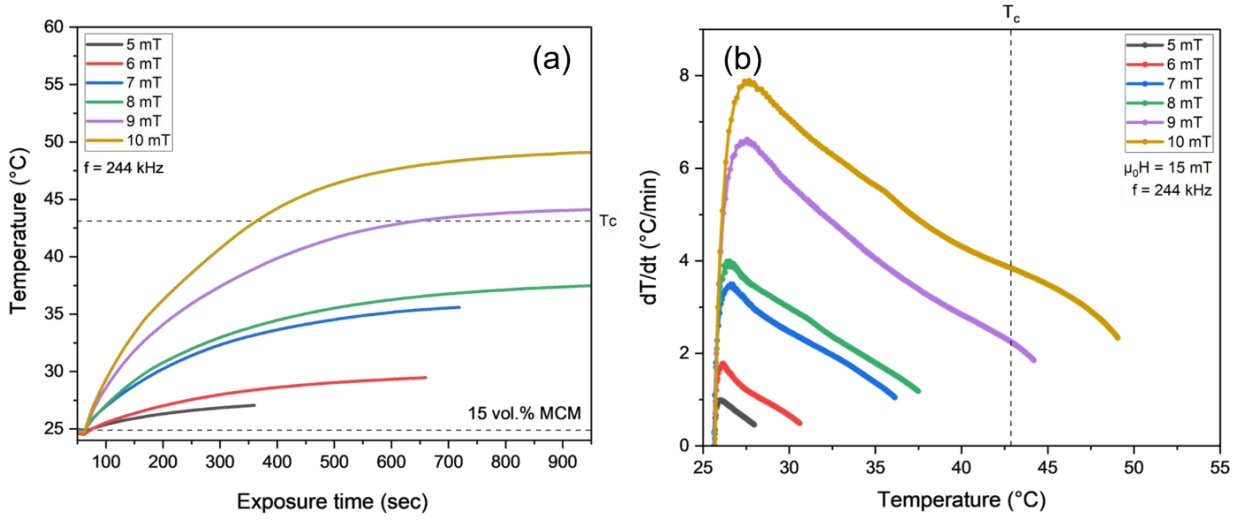

Figure 4.27 Heating behavior of 15 vol.% $Mn_{0.65}Fe_{1.30}P_{0.65}Si_{0.37}$ (MCM) samples when subjected under with different field amplitudes, from 5 to 10 mT at fixed frequency at 244 kHz **a)** temperature changes as a function of exposure time and **b)** its heating rate (dT/dt).

Specific Loss Power (SLP) Value Analysis

The influence of the applied field on the heating efficiency of 15 vol.% MCM wax composite at the fixed frequency at 244 kHz is plotted in **Figure 4.28**. A summary of SLP values determined based on **Eq. 4.1** is provided in **Table 4.9**. The SLP values turns out to gradually increase with an increase in magnetic field amplitudes, ranging from 5 to 10 mT. The results also show that the increase in heating rate (dT/dt) leads to a significant increase in SLP values. In this study, the maximum heating parameters and the highest SAR values were achieved with a combination of a 244 kHz frequency and a 10 mT magnetic field amplitude for the 15 vol.% MCM wax composite.

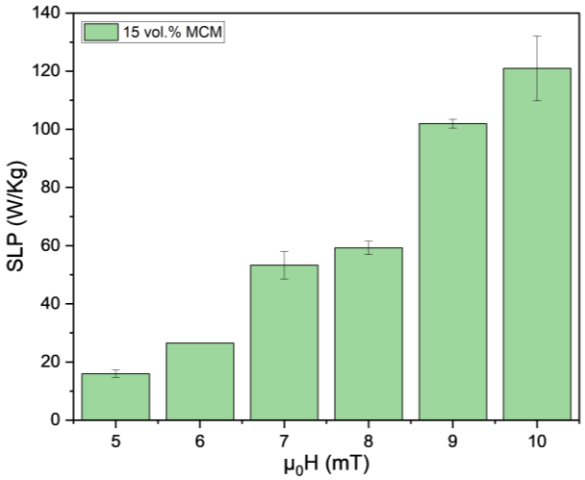

Figure 4. 28 SLP values of 15 vol.% magnetocaloric $Mn_{0.65}Fe_{1.30}P_{0.65}Si_{0.37}$ particles when subjected to different magnetic field amplitudes. The error bars denote the standard deviation.

Table 4.9 Summary of parameters obtained from the temperature rise of 15 vol.% MCM wax composite when subjected to different magnetic field strengths at frequency = 244 kHz. The numbers within the blanket {-} depict the standard deviation (SD).

Experimental condition	Time needed to reach melting temperature 42°C (min)	dT/dt (°C/s)	m_s/m_p	SLP (W/kg)	Sample size
5	-	0.016	1.774	15.99 {1.30}	3
6	-	0.027		26.52 {0.00}	2
7	-	0.054		53.29 {4.71}	2
8	-	0.060		59.25 {2.32}	2
9	7.50	0.103		101.98 {1.52}	3
10	4.48	0.122		121.96 {11.13}	3

Practical Application and Thermal Safety Considerations

In order to melt the wax composite efficiently, the following parameters appear promising: 15 vol.% MCM sample, 10 mT magnetic field, and 244 kHz frequency. This setup is confirmed to be capable of melting the wax composite before reaching the therapeutic range. However, it is crucial to consider thermal safety based on the CEM43 protocol, a thermal dose parameter used to quantify and standardize the effect of hyperthermia on tissues, particularly to prevent cell death. The CEM43 protocol normalizes and converts diverse time-temperature profiles into an equivalent exposure time at 43°C. The blood-brain barrier (BBB) CEM43 = 2 min was used. It means at 43°C, tissue can endure exposure for 2 minutes without significant damage. The calculated results, based on **Eq. 3.4**, are plotted in **Figure 4.29**. It shows that higher

temperatures require shorter exposure times to achieve the same biological effect as the temperature of 43°C. For instance, exposing tissue or cell cultures for 2 min at 43°C causes equivalent effects to 0.125 min at 47°C.

Although the 15 vol.% MCM sample under a 10 mT magnetic field shows the highest heating efficiency and heating rate, facilitating the complete melting of the wax matrix within a short period of exposure time, it may easily cause thermal adverse effects since its saturated temperature is very close to the therapeutic threshold of 47°C. Due to this reason, the 15 vol.% MCM sample under a 9 mT magnetic field shows more promising candidate for further investigation. It combines efficient melting of the wax matrix with stable temperature control within the therapeutic range, ensuring safe and effective use.

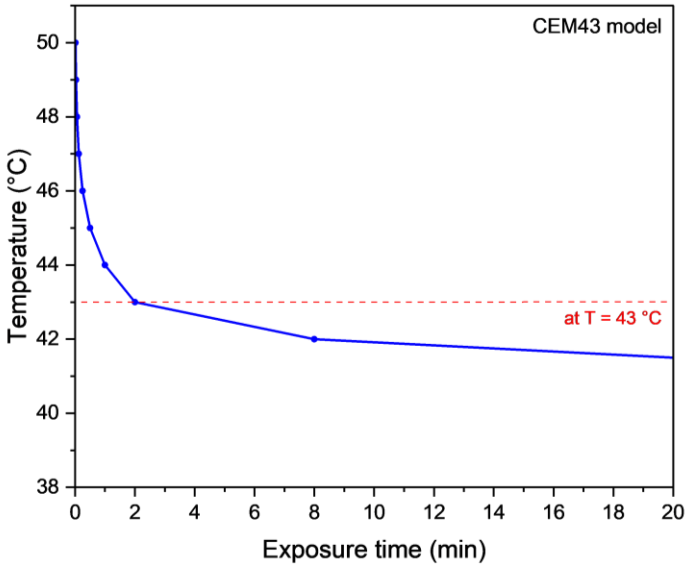

Figure 4.29 CEM43 values plotted for value of CEM43 is 2 min. According to the model, all exposure time-temperature pairs that fall on that line cause the same thermal damage to the tissue.

4.2.2.2. Additional Magnetization Study: Hysteresis Loss Area

The magnetization behavior of three magnetic particles, including carbonyl iron powder (CIP), Fe_3O_4, and magnetocaloric $Mn_{0.65}Fe_{1.30}P_{0.65}Si_{0.37}$ (indicated as MCM), was examined using SQUID analysis at 310 K. The hysteresis loop of these particles, measured from -1 T to 1 T, is shown in **Figure 4.30**. The area of the minor loop in the hysteresis loss was determined by calculating the areas between the increasing and decreasing fields of the magnetization (M) versus magnetic field strength (H) loops within a limited range of 10 mT, which corresponds to the field strength used in inductive heating via an alternating magnetic field. The coercivity (H_c) and remanent magnetization (M_r) values were evaluated and presented in **Table 4.10**. CIP exhibits the highest saturation magnetization (M_s) of 204.93 Am²/kg, compared to Fe_3O_4 (78.57 Am²/kg) and MCM (76.83 Am²/kg). The coercivity values were found to be 0.22, 8.60, and 4.22 Am²/kg for CIP, Fe_3O_4, and MCM, respectively. Moreover, regarding the calculated hysteresis loss area, the Fe_3O_4 sample shows the largest hysteresis area of 1.12 kJ, followed by the MCM and CIP samples at 0.56 kJ and 0.25 kJ, respectively.

Based on the hysteresis loss calculation, Fe_3O_4 is expected to produce more heat compared to the MCM and CIP samples. However, during inductive heating experiments under AMF, it does not exhibit the highest heating efficiency. This discrepancy may be influenced by the heating based on the eddy current effect that occurs during inductive heating experiments. In principle, the heating losses of magnetic materials can originate from hysteresis losses and/or eddy currents. In most magnetic particles, especially in nanoparticles, the main heating mechanism is by hysteresis losses, whereas the Joule effect can be discarded due to the small size of the particles. However, for magnetic materials with larger sizes, such as

in our case, this effect should also be considered. As mentioned earlier, to avoid excessive nonspecific eddy current heating, the Hergt and Dutz limit, where H x f should not exceed 5 x 10^9 A m^{-1} s^{-1} was used. According to the AMF parameters used in the experiment, with a fixed frequency of 244 kHz and a magnetic field of 10 mT, the calculated H x f is equal to 1.96 x 10^9 A m^{-1} s^{-1}. Therefore, the influence of eddy currents in our case may be negligible.

With this in mind, the relationship between the calculated area of magnetic hysteresis loss and heating efficiency observed during the heating experiments is not directly proportional. This relationship may not be straightforward due to several factors, such as particle size, shape, material properties, and the parameters of the applied magnetic field. This might be interesting to investigate further.

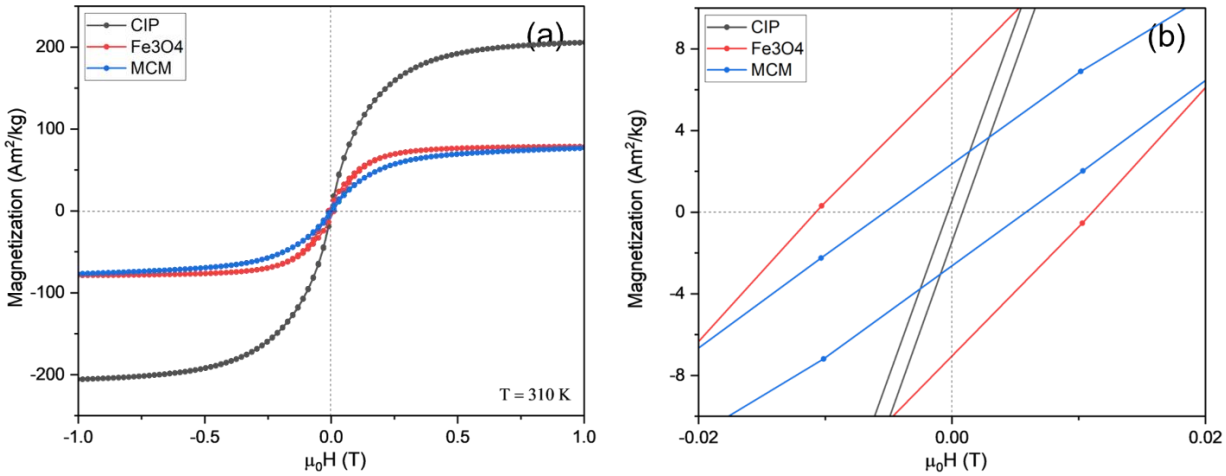

Figure 4. 30 a) Magnetic hysteresis of CIP, Fe_3O_4, and magnetocaloric $Mn_{0.65}Fe_{1.30}P_{0.65}Si_{0.37}$ (MCM) particles and **b)** Magnification of the magnetization loops of a near the origin.

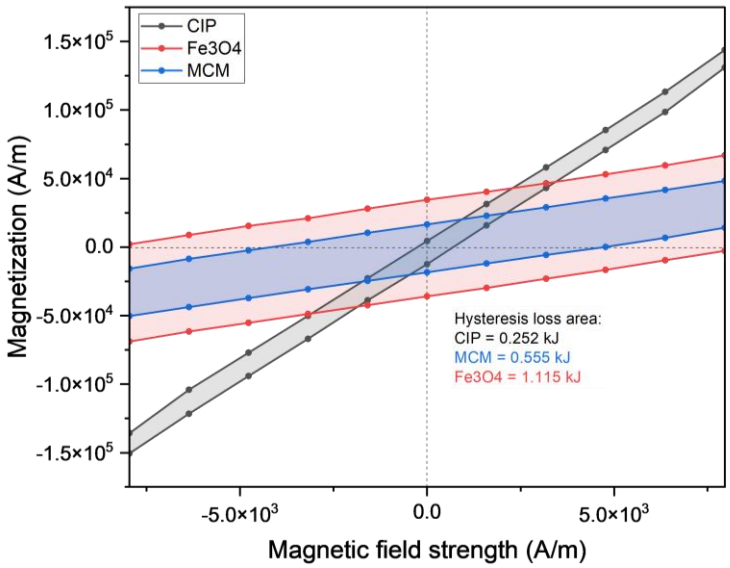

Figure 4. 31 Hysteresis of CIP, Fe_3O_4, and magnetocaloric (MCM) particles within the range of 10 mT.

Table 4.10 Magnetic hysteresis loops for three type magnetic samples used to fabricate magnetic wax composites obtained from the SQUID measurements at a temperature of 310 K.

Magnetic sample	M_s (Am^2/kg)	M_r (Am^2/kg)	H_c (kA/m)	Hysteresis area (kJ/m^3)
CIP	204.93	0.54	0.22	0.25
Fe_3O_4	78.57	6.77	8.60	1.12
MCM	76.83	2.39	4.22	0.56

4.2.2.3. Inductive Heating under Static Magnetic Field (SMF)

The heating behavior of the developed $Mn_{0.65}Fe_{1.30}P_{0.65}Si_{0.37}$ wax composite sample was investigated under a static magnetic field (SMF). The sample, containing 25 vol.% of $Mn_{0.65}Fe_{1.30}P_{0.65}Si_{0.37}$ particles, was positioned between a pair of NdFeB permanent magnets. Thermographic images of the wax composite in an Eppendorf tube, captured during the SMF exposure, are shown in **Figure 4.32a**. The range of temperature change over the exposure time is presented in **Figure 4.32b**.

It was found that after 10 min of exposure to the permanent magnetic field, there was no significant increase in temperature; it remained between 22-25°C, indicating that the fabricated $Mn_{0.65}Fe_{1.30}P_{0.65}Si_{0.37}$ wax composite hardly responds to the static magnetic field. This lack of response is due to the heating generation mechanism of magnetic heating, which is primarily based on hysteresis loss, which requires an oscillating alternating magnetic field (AMF). Under applied magnetic field at 0.01 T, the thermal hysteresis loss (ΔT_{hys}) observed during the cycle with this compound is only 5 K. This is too low to generate significant heat without the facilitation of an AMF. These findings highlight the necessity of using an alternating magnetic field to achieve effective heating in $Mn_{0.65}Fe_{1.30}P_{0.65}Si_{0.37}$ wax composite and suggest that static magnetic field is inadequate for this purpose. Further optimization and experimentation with AMF are essential for utilizing these composites in practical thermal applications.

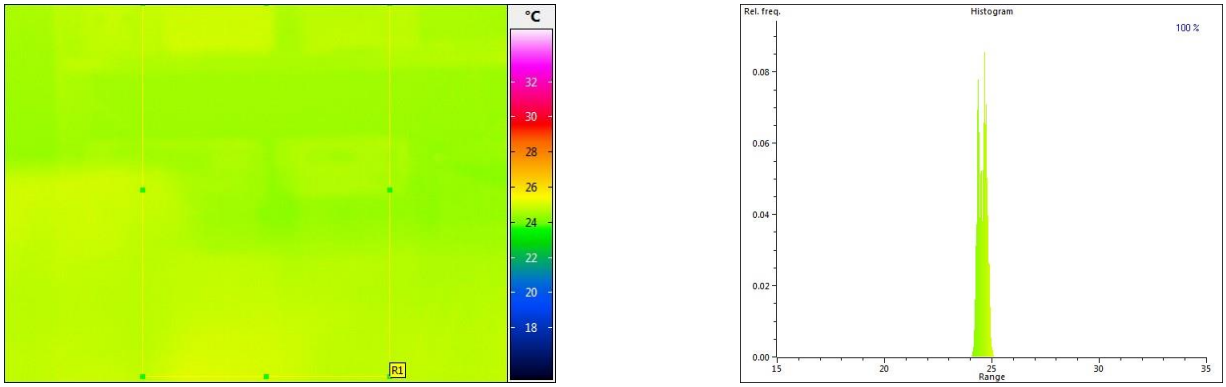

Figure 4.32 Thermographic images of $Mn_{0.65}Fe_{1.30}P_{0.65}Si_{0.37}$ sample with 25 vol.% particle concentration in Eppendorf when subjected between a pair of NdFeB permanent magnets.

4.3. Part 3: Biodegradability Assessment

4.3.1. Biodegradability

The water absorption of the wax composite during the degradation process was determined to monitor changes in its water permeability. This study measured the change in water absorption (PBS at pH 7.4) over time, up to 28 days at 37°C (body temperature) and calculated the percentage of water absorption using **Eq. 3.10**. Two wax samples were observed: an MCM sample with 5 vol.% magnetocaloric particles and a pure wax matrix (30 vol.% BBW wax mixed with lanolin wax). The results for these two samples are shown in **Figure 4.34**.

The data revealed similar water uptake behavior in both samples. Over the 28-day degradation period, both samples exhibited a slight increase in water uptake. For the first 7 days, almost no water uptake was observed, with the percentage of water absorption remaining approximately 5%. By the end of the 28-day immersion in PBS, the samples absorbed around 25% water. Visual inspection of the samples indicated that the pure wax samples remained largely unchanged in shape compared to their initial form. However, the wax samples mixed with magnetic particles showed slight shape changes after 28 days of immersion. **Figure 4.33** presents SEM images showing microcracks in the MCM sample with 5 vol.% magnetocaloric particles after 14 days of immersion. These microcracks were typically located around the edges of the sample, while the surface in the center remained relatively unchanged compared to the pre-immersion sample. So far, these observations provide insights into the degradation and water absorption behavior of the wax composites, highlighting the impact of incorporating magnetocaloric particles on the structural integrity of the wax matrix over time.

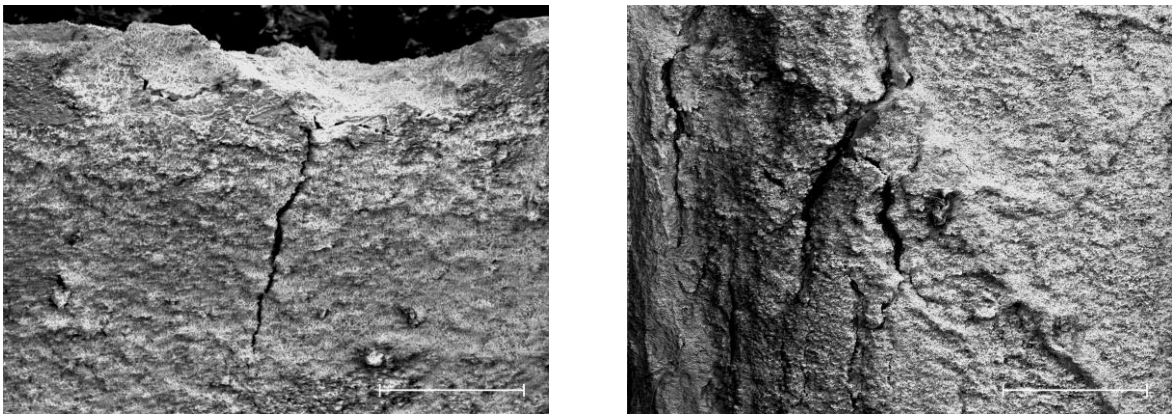

Figure 4.33 SEM images of cracks observed on the surface of the 5 vol.% MCM sample after immersion in PBS at a pH of 7.4 and a temperature of 37°C after 28 days (the scale bar is 500 μm).

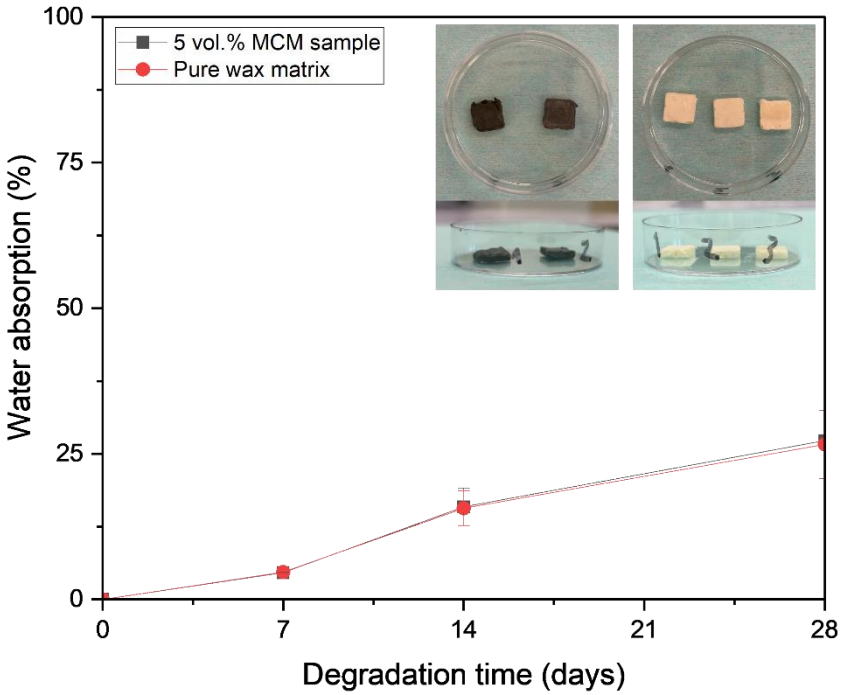

Figure 4.34 The water absorption behavior of the 5 vol.% MCM wax sample and pure wax matrix immersed in PBS at pH 7.4 at 37°C and the morphological changes in the 5 vol.% MCM sample and the pure wax matrix after 28 d of immersion in PBS at a pH of 7.4 and a temperature of 37°C.

5

Conclusion and Recommendations

This master project successfully explored the potential of the magnetocaloric $(Mn,Fe)_2(P,Si)$-based compound for biomedical applications, specifically as a biodegradable membrane for multi-cell separation in Organ-on-Chip platforms. The need for a precise co-seeding timing of organoid and vascular cells necessitated the development of a non-permeable barrier membrane. The wax material was chosen for its hydrophobic properties, effectively separating the different cell cultures until the appropriate maturation stage.

The magnetocaloric $(Mn,Fe)_2(P,Si)$-based compound was selected for further investigation due to its sharp phase transition characteristics and tunable Curie temperature (Tc). These features allow the magnetocaloric compound to self-regulate their temperature, maintaining it within the therapeutic range and preventing potential damage to living cells. The synthesized $Mn_{0.65}Fe_{1.30}Si_{0.37}P_{0.65}$ compound exhibited the desired transition temperature at 316 K (43°C) and particle sizes ranging from approximately 1-5 µm.

A magnetocaloric wax-based composite was then synthesized by integrating the magnetocaloric particles with a wax component. Characterization of this composite under alternating magnetic fields (AMF) revealed that temperature rise significantly increased with higher magnetic concentrations and field amplitudes. Notably, at an applied AMF of 9 mT and a frequency of 244 kHz, a sample containing 15 vol.% magnetic particles stabilized at 44°C after reaching its Curie transition point (43°C). This demonstrated the composite's capability to maintain controlled temperatures within the therapeutic range (42-47°C), efficiently melting the wax without harming living cells. Additionally, degradation assessment based on water absorption percentage and SEM imaging indicated low water permeability and minimal microcracks over time.

In conclusion, this study confirms the potential of magnetocaloric materials with tunable Curie temperatures for self-temperature control in biomedical applications. The high heating efficiency and ability to prevent overheating provide promising prospects for thermal activation processes in various biomedical fields.

By addressing these recommendations, future research can significantly improve the application and effectiveness of magnetocaloric materials in biomedical contexts.

Improve in Curie temperature (T_c):

Although the developed magnetocaloric particles exhibit self-regulating behavior, maintaining their temperature within the therapeutic range remains challenging. Observations under magnetic fields showed that once the transition temperature was exceeded, the temperature increased slightly over T_c before stabilizing and decreasing in heating rate over time. Adjusting the magnetic field from 10 mT to 9 mT reduced the saturated temperature from 47°C to 44°C, making it safer and still effective in melting the wax. However, according to CEM43 protocol data, cells can only endure exposure to a heating source at 44°C for only one minute. Therefore, a T_c of 43°C may be too high. Lowering the T_c slightly would help minimize heating effects that could damage cell cultures, ensuring the material controls temperature within a safer range.

Investigate the relationship between hysteresis loss area and specific loss power (SLP):

The CIP and Fe_3O_4 particles were included to demonstrate the superior self-temperature control of magnetocaloric (MCM) particles due to their Curie temperature (Tc), which is a key feature distinguishing MCM from CIP and Fe_3O_4. However, it is crucial to acknowledge the difficulty in directly comparing hysteresis loss area calculations with experimental results, especially when evaluating the heating efficiency of different magnetic particles. The challenge arises from the varying amounts of each magnetic particle used in the 1 ml composites, calculated based on their density. For instance, 1 ml of a sample with 15 vol.% magnetic particles required 0.765 g of Fe_3O_4, 1.178 g of CIP, and 1.048 g of MCM. To enable a fair comparison of heating efficiency, future experiments should use equal masses of each type of magnetic particle

Investigate the influence of the frequency on the heating efficiency of magnetic wax composite:

Experiments have confirmed that magnetic amplitudes and particle concentrations significantly influence the heating behavior of magnetocaloric (MCM) and other magnetic particles. Several studies have shown that the influence of frequencies on the heating efficiency of magnetic particles. Future research should explore whether tuning frequency or magnetic field provides optimal parameters for inductive heating tests, enhancing the heating efficiency of magnetic wax composites for transient membranes.

Investigate the performance in cell separation via chip platform (injection and evacuation test):

The percentage of water absorption alone cannot confirm that the developed magnetocaloric composite effectively separates two cell cultures. Future studies should include injection tests of the membrane in the chip to evaluate its cell separation capabilities. Additionally, in real biomedical applications, the composite must be removed from the platform after serving as a membrane barrier. Research should focus on methods for opening the membrane and evacuating it from the platform once its function is complete.

References

[1] J. Sarkar, “Ferromagnetic Sputtering Targets and Thin Films for Silicides and Data Storage,” 2014, pp. 501–565. doi: 10.1016/B978-0-8155-1593-7.00007-2.

[2] T. Scepka, “Noninvasive control of magnetic state in ferromagnetic nanodots by Hall probe magnetometry,” 2016.

[3] J. V. Nuzhina, A. A. Shtil, A. Y. Prilepskii, and V. V. Vinogradov, “Preclinical Evaluation and Clinical Translation of Magnetite-Based Nanomedicines,” *J. Drug Deliv. Sci. Technol.*, vol. 54, p. 101282, Dec. 2019, doi: 10.1016/j.jddst.2019.101282.

[4] G. Niraula *et al.*, “The Curie temperature: a key playmaker in self-regulated temperature hyperthermia,” *J. Mater. Chem. B*, vol. 12, no. 2, pp. 286–331, Jan. 2024, doi: 10.1039/D3TB01437A.

[5] I. Hilger, “In vivo applications of magnetic nanoparticle hyperthermia,” *Int. J. Hyperthermia*, vol. 29, no. 8, pp. 828–834, Dec. 2013, doi: 10.3109/02656736.2013.832815.

[6] S. Ganguly and S. Margel, “3D printed magnetic polymer composite hydrogels for hyperthermia and magnetic field driven structural manipulation,” *Prog. Polym. Sci.*, vol. 131, p. 101574, Aug. 2022, doi: 10.1016/j.progpolymsci.2022.101574.

[7] B. Giorgio, *Hysteresis in magnetism: for physicists, materials scientists, and engineers*, 1st ed. Academic Press, 1998.

[8] R. Jedamski *et al.*, “Potential of magnetic Barkhausen noise analysis for in-process monitoring of surface layer properties of steel components in grinding,” *Tm - Tech. Mess.*, vol. 87, pp. 787–798, Nov. 2020, doi: 10.1515/teme-2020-0048.

[9] S. Ahmed, B. L. Rajak, M. Gogoi, and H. D. Sarma, “Chapter 16 - Magnetic nanoparticles mediated cancer hyperthermia,” in *Smart Healthcare for Disease Diagnosis and Prevention*, S. Paul and D. Bhatia, Eds., Academic Press, 2020, pp. 153–173. doi: 10.1016/B978-0-12-817913-0.00016-X.

[10] E. Myrovali *et al.*, “Toward the Separation of Different Heating Mechanisms in Magnetic Particle Hyperthermia,” *ACS Omega*, vol. 8, no. 14, pp. 12955–12967, Mar. 2023, doi: 10.1021/acsomega.2c05962.

[11] B. D. Cullity and C. D. Graham, “Domains and the Magnetization Process,” in *Introduction to Magnetic Materials*, IEEE, 2009, pp. 275–333. doi: 10.1002/9780470386323.ch9.

[12] P. Wilson, “Chapter 3 - Passive Components,” in *The Circuit Designer’s Companion (Fourth Edition)*, P. Wilson, Ed., Newnes, 2017, pp. 93–157. doi: 10.1016/B978-0-08-101764-7.00003-7.

[13] Z. Hedayatnasab, A. Ramazani Saadatabadi, H. Shirgahi, and M. R. Mozafari, “Heat induction of iron oxide nanoparticles with rational artificial neural network design-based particle swarm optimization for magnetic cancer hyperthermia,” *Mater. Res. Bull.*, vol. 157, p. 112035, Jan. 2023, doi: 10.1016/j.materresbull.2022.112035.

[14] M. S. Shaikh, R. Jones, R. Donnan, and R. Dubrovka, “Electromagnetic triggering with metallic microparticles for prospective biomedical applications,” *Results Eng.*, vol. 20, p. 101597, Dec. 2023, doi: 10.1016/j.rineng.2023.101597.

[15] D. Rifai, A. Abdalla, N. Khamsah, M. Aizat, and M. Fadzli, “Subsurface Defects Evaluation using Eddy Current Testing,” *Indian J. Sci. Technol.*, vol. 9, Mar. 2016, doi: 10.17485/ijst/2016/v9i9/88724.

[16] B. Herrero de la Parte *et al.*, “Proposal of New Safety Limits for In Vivo Experiments of Magnetic Hyperthermia Antitumor Therapy,” *Cancers*, vol. 14, no. 13, p. 3084, Jun. 2022, doi: 10.3390/cancers14133084.

[17] S. hyun Noh, S. H. Moon, T. H. Shin, Y. Lim, and J. Cheon, “Recent advances of magneto-thermal capabilities of nanoparticles: From design principles to biomedical applications,” *Nano Today*, vol. 13, pp. 61–76, Apr. 2017, doi: 10.1016/j.nantod.2017.02.006.

[18] F. Zhang, “Tuning Giant Magnetocaloric Materials: A Study of (Mn,Fe)2(P,Si) and NiCoMnTi Heusler Compounds,” 2022, doi: 10.4233/uuid:88a142a9-3ac4-4d97-ab1c-1cf811b07abb.

[19] H.-L. Yan, X. Huang, and C. Esling, “Recent Progress in Crystallographic Characterization, Magnetoresponsive and Elastocaloric Effects of Ni-Mn-In-Based Heusler Alloys—A Review,” *Front. Mater.*, vol. 9, Feb. 2022, doi: 10.3389/fmats.2022.812984.

[20] J. Llacer-Wintle *et al.*, “The magnetopyroelectric effect: heat-mediated magnetoelectricity in magnetic nanoparticle-ferroelectric polymer composites,” *Mater. Horiz.*, vol. 10, no. 7, pp. 2627–2637, Jul. 2023, doi: 10.1039/D2MH01361D.
[21] Z. Behrouzkia, Z. Joveini, B. Keshavarzi, N. Eyvazzadeh, and R. Z. Aghdam, “Hyperthermia: How Can It Be Used?,” *Oman Med. J.*, vol. 31, no. 2, pp. 89–97, Mar. 2016, doi: 10.5001/omj.2016.19.
[22] S. Kumar, M. Kumar, and A. Singh, “Synthesis and characterization of iron oxide nanoparticles (Fe2O3, Fe3O4): a brief review,” *Contemp. Phys.*, vol. 62, no. 3, pp. 144–164, Jul. 2021, doi: 10.1080/00107514.2022.2080910.
[23] Q. Shen, “Tuning Magnetoelastic Transitions in Mn2Sb-based and Fe2Hf-based Magnetocaloric Materials,” 2023, doi: 10.4233/uuid:3f379e63-9a3e-4755-974d-4d2099db43ea.
[24] V. T. Nguyên, “Influence of compositions and size on the giant magnetocaloric effect in (Mn,Fe)2(P,Si)-based compounds,” 2017, doi: 10.4233/uuid:b40864fa-cc4b-43b2-816d-98f810296a24.
[25] X. You, M. Maschek, N. H. H. van Dijk, and E. Brück, “Magnetic phase diagram of the mnx fe2−x p1−y siy system,” *Entropy*, vol. 24, no. 1, 2022, doi: 10.3390/e24010002.
[26] F. Zhang, X. Miao, N. van Dijk, E. Brück, and Y. Ren, “Advanced Magnetocaloric Materials for Energy Conversion: Recent Progress, Opportunities, and Perspective,” *Adv. Energy Mater.*, vol. 14, no. 21, 2024, doi: 10.1002/aenm.202400369.
[27] D. Mertz, O. Sandre, and S. Bégin-Colin, “Drug releasing nanoplatforms activated by alternating magnetic fields,” *Biochim. Biophys. Acta Gen. Subj.*, vol. 1861, no. 6, pp. 1617–1641, Jun. 2017, doi: 10.1016/j.bbagen.2017.02.025.
[28] S. Campbell, D. Maitland, and T. Hoare, “Enhanced Pulsatile Drug Release from Injectable Magnetic Hydrogels with Embedded Thermosensitive Microgels,” *ACS Macro Lett.*, vol. 4, no. 3, pp. 312–316, Mar. 2015, doi: 10.1021/acsmacrolett.5b00057.
[29] A. S. Komlev, R. R. Gimaev, and V. I. Zverev, “Smart magnetocaloric coatings for implants: Controlled drug release for targeted delivery,” *Phys. Open*, vol. 7, p. 100063, May 2021, doi: 10.1016/j.physo.2021.100063.
[30] J. Tang *et al.*, “Programmable shape transformation of 3D printed magnetic hydrogel composite for hyperthermia cancer therapy,” *Extreme Mech. Lett.*, vol. 46, p. 101305, Jul. 2021, doi: 10.1016/j.eml.2021.101305.
[31] Y. lian *et al.*, “Recent advances on the magnetic nanoparticle–based nanocomposites for magnetic induction hyperthermia of tumor: a short review,” *Adv. Compos. Hybrid Mater.*, vol. 4, no. 4, pp. 925–937, Dec. 2021, doi: 10.1007/s42114-021-00373-3.
[32] C. Wang *et al.*, “Smart composite hydrogel with magnetocaloric anisotropy for controllable multi-drug release,” *J. Magn. Magn. Mater.*, vol. 565, p. 170267, Jan. 2023, doi: 10.1016/j.jmmm.2022.170267.
[33] J. N. Anker and O. T. Mefford, Eds., *Biomedical Applications of Magnetic Particles*. Boca Raton: CRC Press, 2020. doi: 10.1201/9781315117058.
[34] Q. Ze *et al.*, “Magnetic Shape Memory Polymers with Integrated Multifunctional Shape Manipulation,” *Adv. Mater.*, vol. 32, Dec. 2019, doi: 10.1002/adma.201906657.
[35] T. A. P. Rocha-Santos, “Sensors and biosensors based on magnetic nanoparticles,” *TrAC Trends Anal. Chem.*, vol. 62, pp. 28–36, Nov. 2014, doi: 10.1016/j.trac.2014.06.016.
[36] Y.-T. Chen, A. G. Kolhatkar, O. Zenasni, S. Xu, and T. R. Lee, “Biosensing Using Magnetic Particle Detection Techniques,” *Sensors*, vol. 17, no. 10, Art. no. 10, Oct. 2017, doi: 10.3390/s17102300.
[37] B. M. Sahoo, B. V. V. R. Kumar, C. N. Patra, J. R. Panda, B. C. Mohanta, and N. N. Palei, “Nanotechnology: A Novel Approach for Drug Development in Health Care System,” *Curr. Nanomater.*, vol. 5, no. 1, pp. 12–25, doi: 10.2174/2405461505666200320152824.
[38] V. Harish *et al.*, “Nanoparticle and Nanostructure Synthesis and Controlled Growth Methods,” *Nanomaterials*, vol. 12, no. 18, Art. no. 18, Jan. 2022, doi: 10.3390/nano12183226.
[39] C. Dhand *et al.*, “Methods and strategies for the synthesis of diverse nanoparticles and their applications: a comprehensive overview,” *RSC Adv.*, vol. 5, no. 127, pp. 105003–105037, Dec. 2015, doi: 10.1039/C5RA19388E.
[40] K. Wu, D. Su, J. Liu, R. Saha, and J.-P. Wang, “Magnetic nanoparticles in nanomedicine: a review of recent advances,” *Nanotechnology*, vol. 30, no. 50, p. 502003, Dec. 2019, doi: 10.1088/1361-6528/ab4241.
[41] H.-R. Shen *et al.*, “Microstructure and magnetic properties of anisotropic Mn-Bi powder prepared by low energy ball milling assisted with polyvinylpyrrolidone,” *J. Magn. Magn. Mater.*, vol. 551, p. 169108, Jun. 2022, doi: 10.1016/j.jmmm.2022.169108.

[42] “Ball milling method for nanomaterial synthesis.” Accessed: Jun. 23, 2024. [Online]. Available: https://www.understandingnano.com/nanomaterial-synthesis-ball-milling.html
[43] “Planetary Mill PULVERISETTE 5/4 classic line / Description.” Accessed: Jun. 23, 2024. [Online]. Available: https://www.fritsch-international.com/sample-preparation/milling/planetary-mills/details/product/pulverisette-54-classic-line/
[44] S. Zhang, Z. Wan, and R. D. Kamm, “Vascularized organoids on a chip: strategies for engineering organoids with functional vasculature,” *Lab. Chip*, vol. 21, no. 3, pp. 473–488, Feb. 2021, doi: 10.1039/D0LC01186J.
[45] V. Carvalho, M. Bañobre-López, G. Minas, S. F. C. F. Teixeira, R. Lima, and R. O. Rodrigues, “The integration of spheroids and organoids into organ-on-a-chip platforms for tumour research: A review,” *Bioprinting*, vol. 27, p. e00224, Aug. 2022, doi: 10.1016/j.bprint.2022.e00224.
[46] K. Katoh, “Effects of Mechanical Stress on Endothelial Cells In Situ and In Vitro,” *Int. J. Mol. Sci.*, vol. 24, no. 22, p. 16518, Nov. 2023, doi: 10.3390/ijms242216518.
[47] T. Yu, Q. Yang, B. Peng, Z. Gu, and D. Zhu, “Vascularized organoid-on-a-chip: design, imaging, and analysis,” *Angiogenesis*, vol. 27, no. 2, pp. 147–172, May 2024, doi: 10.1007/s10456-024-09905-z.
[48] Y. Nashimoto *et al.*, “Integrating perfusable vascular networks with a three-dimensional tissue in a microfluidic device,” *Integr. Biol. U. K.*, vol. 9, no. 6, pp. 506–518, Jun. 2017, doi: 10.1039/c7ib00024c.
[49] I. Salmon *et al.*, “Engineering neurovascular organoids with 3D printed microfluidic chips,” *Lab. Chip*, vol. 22, no. 8, pp. 1615–1629, Apr. 2022, doi: 10.1039/D1LC00535A.
[50] S. M. Won *et al.*, “Natural Wax for Transient Electronics,” *Adv. Funct. Mater.*, vol. 28, no. 32, p. 1801819, 2018, doi: 10.1002/adfm.201801819.
[51] A. H. M. Dezfouli, S. Majidi, and A. Jahangiri, “Magnetocalorically accelerated charging of latent thermal energy storage systems,” *Int. Commun. Heat Mass Transf.*, vol. 145, p. 106850, Jun. 2023, doi: 10.1016/j.icheatmasstransfer.2023.106850.
[52] Z. Jia, C. Hu, Y. Zhang, S. Zhang, and B. Tang, “Exploring electro-thermal conversion in phase change materials: A review,” *Compos. Part Appl. Sci. Manuf.*, vol. 175, p. 107809, Dec. 2023, doi: 10.1016/j.compositesa.2023.107809.
[53] K.-S. Kim *et al.*, “Biodegradable Molybdenum/Polybutylene Adipate Terephthalate Conductive Paste for Flexible and Stretchable Transient Electronics,” *Adv. Mater. Technol.*, vol. 7, no. 2, p. 2001297, 2022, doi: 10.1002/admt.202001297.
[54] Z. Wei, X. Ma, H. Zhao, X. Wu, and Q. Guo, “Accelerable Self-Sintering of Solvent-Free Molybdenum/Wax Biodegradable Composites for Multimodally Transient Electronics,” *ACS Appl. Mater. Interfaces*, Jul. 2022, doi: 10.1021/acsami.2c04647.
[55] K. S. Kim *et al.*, “Isotropic conductive paste for bioresorbable electronics,” *Mater. Today Bio*, vol. 18, p. 100541, Feb. 2023, doi: 10.1016/j.mtbio.2023.100541.
[56] P. Cataldi *et al.*, “An Electrically Conductive Oleogel Paste for Edible Electronics,” *Adv. Funct. Mater.*, vol. 32, no. 23, p. 2113417, Jun. 2022, doi: 10.1002/adfm.202113417.
[57] F. Guillou *et al.*, “Electronic and magnetic properties of phosphorus across the first-order ferromagnetic transition of (Mn , Fe) 2 (P , Si , B) giant magnetocaloric materials,” *Phys. Rev. B*, vol. 92, Dec. 2015, doi: 10.1103/PhysRevB.92.224427.
[58] A. Kiecana, “Magnetic Phase Transitions and Magnetic Structures in Mn-based Compounds,” Delft University of Technology, 2023. doi: 10.4233/UUID:7851D718-D584-45FF-BC68-AB77188E286E.
[59] A. Kiecana, C. Kwakernaak, N. H. van Dijk, and E. Brück, “Effect of the heat treatment on the microstructure, magnetism and magnetocaloric effect in Fe-rich (Mn,Fe)y(P,Si) melt-spun ribbons,” *J. Alloys Compd.*, vol. 932, p. 167635, Jan. 2023, doi: 10.1016/j.jallcom.2022.167635.
[60] N. Thang, H. Yibole, N. van Dijk, and E. Brück, “Effect of heat treatment conditions on MnFe(P,Si,B) compounds for room-temperature magnetic refrigeration,” *J. Alloys Compd.*, vol. 699, Dec. 2016, doi: 10.1016/j.jallcom.2016.12.402.
[61] M. Namvari, James. J. Rosero-Romo, V. Laitinen, A. Kumthekar, D. Salazar, and K. Ullakko, “Effect of moderate Fe doping and heat treatment on the microstructure of Ni-Mn-Ga melt-spun ribbons,” *J. Alloys Compd.*, vol. 969, p. 172424, Dec. 2023, doi: 10.1016/j.jallcom.2023.172424.
[62] “JSM-IT100 InTouchScope™ Scanning Electron Microscope | Products | JEOL Ltd.,” JSM-IT100 InTouchScope™ Scanning Electron Microscope | Products | JEOL Ltd. Accessed: Jul. 05, 2024. [Online]. Available: https://www.jeol.com/

[63] G. C. van Rhoon, “Is CEM43 still a relevant thermal dose parameter for hyperthermia treatment monitoring?,” *Int. J. Hyperth. Off. J. Eur. Soc. Hyperthermic Oncol. North Am. Hyperth. Group*, vol. 32, no. 1, pp. 50–62, 2016, doi: 10.3109/02656736.2015.1114153.
[64] M. Murbach *et al.*, “Thermal tissue damage model analyzed for different whole-body SAR and scan durations for standard MR body coils,” *Magn. Reson. Med.*, vol. 71, no. 1, pp. 421–431, Jan. 2014, doi: 10.1002/mrm.24671.
[65] C. G. Scanes, “Chapter 2 - Animal Attributes Exploited by Humans (Nonfood Uses of Animals),” in *Animals and Human Society*, C. G. Scanes and S. R. Toukhsati, Eds., Academic Press, 2018, pp. 13–40. doi: 10.1016/B978-0-12-805247-1.00002-2.
[66] M. A. Taleb and H. El-Sayed, “Preparation and characterization of lanolin-based condensate and its utilization as a nonionic softener for wool fabric surface,” *J. Appl. Res. Technol.*, vol. 19, no. 5, Art. no. 5, Oct. 2021, doi: 10.22201/icat.24486736e.2021.19.5.1443.
[67] M. Abou-Taleb and H. El-Sayed, “Chapter 25 - By-products during processing of fiber and their use: generation of by-products during wool processing and their utilization,” in *The Wool Handbook*, S. Jose, S. Thomas, and G. Basu, Eds., in The Textile Institute Book Series. , Woodhead Publishing, 2024, pp. 577–592. doi: 10.1016/B978-0-323-99598-6.00017-7.
[68] H. Ding, D. Zhao, and Y. Gao, “Response surface optimization of cholesterol extraction from lanolin alcohol by selective solvent crystallization,” *Chem. Pap.*, vol. 71, no. 1, pp. 71–79, Jan. 2017, doi: 10.1007/s11696-016-0043-1.
[69] J. P. Simpson, N. Thrower, and J. B. Ohlrogge, “How did nature engineer the highest surface lipid accumulation among plants? Exceptional expression of acyl-lipid-associated genes for the assembly of extracellular triacylglycerol by Bayberry (Myrica pensylvanica) fruits,” *Biochim. Biophys. Acta*, vol. 1861, no. 9 Pt B, pp. 1243–1252, Sep. 2016, doi: 10.1016/j.bbalip.2016.01.022.
[70] H. Zhang and M. W. Grinstaff, “Recent Advances in Glycerol Polymers: Chemistry and Biomedical Applications,” *Macromol. Rapid Commun.*, vol. 35, no. 22, pp. 1906–1924, Nov. 2014, doi: 10.1002/marc.201400389.
[71] J. P. Simpson and J. B. Ohlrogge, “A Novel Pathway for Triacylglycerol Biosynthesis Is Responsible for the Accumulation of Massive Quantities of Glycerolipids in the Surface Wax of Bayberry (Myrica pensylvanica) Fruit,” *Plant Cell*, vol. 28, no. 1, pp. 248–264, Jan. 2016, doi: 10.1105/tpc.15.00900.
[72] W. Lai, Y. Wang, and J. He, “Effects of Carbonyl Iron Powder (CIP) Content on the Electromagnetic Wave Absorption and Mechanical Properties of CIP/ABS Composites,” *Polymers*, vol. 12, no. 8, Art. no. 8, Aug. 2020, doi: 10.3390/polym12081694.
[73] D. Diaz-Bleis, C. Vales-Pinzón, Y. Freile-Pelegrín, and J. J. Alvarado-Gil, “Thermal characterization of magnetically aligned carbonyl iron/agar composites,” *Carbohydr. Polym.*, vol. 99, pp. 84–90, Jan. 2014, doi: 10.1016/j.carbpol.2013.07.053.
[74] A. D. M. Charles, A. N. Rider, S. A. Brown, and C. H. Wang, “Improving the actuation performance of magneto-polymer composites by silane functionalisation of carbonyl-iron particles,” *Compos. Part B Eng.*, vol. 196, p. 108091, Sep. 2020, doi: 10.1016/j.compositesb.2020.108091.
[75] M. Salama, M. F. Vaz, R. Colaço, C. Santos, and M. Carmezim, “Biodegradable Iron and Porous Iron: Mechanical Properties, Degradation Behaviour, Manufacturing Routes and Biomedical Applications,” *J. Funct. Biomater.*, vol. 13, no. 2, p. 72, Jun. 2022, doi: 10.3390/jfb13020072.
[76] G. Gąsior, J. Szczepański, and A. Radtke, “Biodegradable Iron-Based Materials—What Was Done and What More Can Be Done?,” *Materials*, vol. 14, no. 12, Art. no. 12, Jan. 2021, doi: 10.3390/ma14123381.
[77] T. Plachy, E. Kutalkova, M. Sedlacik, A. Vesel, M. Masar, and I. Kuritka, “Impact of corrosion process of carbonyl iron particles on magnetorheological behavior of their suspensions,” *J. Ind. Eng. Chem.*, vol. 66, pp. 362–369, Oct. 2018, doi: 10.1016/j.jiec.2018.06.002.
[78] S. S. Laha *et al.*, “Rare-Earth Doped Iron Oxide Nanostructures for Cancer Theranostics: Magnetic Hyperthermia and Magnetic Resonance Imaging,” *Small*, vol. 18, no. 11, p. 2104855, 2022, doi: 10.1002/smll.202104855.
[79] N. Malhotra *et al.*, “Potential Toxicity of Iron Oxide Magnetic Nanoparticles: A Review,” *Molecules*, vol. 25, no. 14, p. 3159, Jul. 2020, doi: 10.3390/molecules25143159.
[80] M. S. RAZZAQUE, “Phosphate toxicity: new insights into an old problem,” *Clin. Sci. Lond. Engl. 1979*, vol. 120, no. 3, pp. 91–97, Feb. 2011, doi: 10.1042/CS20100377.
[81] G. Verma, K. Mondal, and A. Gupta, “Si-based MEMS resonant sensor: A review from microfabrication perspective,” *Microelectron. J.*, vol. 118, p. 105210, Dec. 2021, doi: 10.1016/j.mejo.2021.105210.

[82] Y. Huang *et al.*, “Silica nanoparticles: Biomedical applications and toxicity,” *Biomed. Pharmacother.*, vol. 151, p. 113053, Jul. 2022, doi: 10.1016/j.biopha.2022.113053.
[83] J. Cheng, B. Liu, Y. H. Wu, and Y. F. Zheng, “Comparative *in vitro* Study on Pure Metals (Fe, Mn, Mg, Zn and W) as Biodegradable Metals,” *J. Mater. Sci. Technol.*, vol. 29, no. 7, pp. 619–627, Jul. 2013, doi: 10.1016/j.jmst.2013.03.019.
[84] S. M. Mousavizadeh and S. H. Tabaian, “Effect of Mn Addition on Corrosion and Biocompatibility Characteristics of a New Biodegradable Mg–1Ca–2Zn–1RE Alloy,” *Met. Mater. Int.*, vol. 27, no. 12, pp. 5074–5081, Dec. 2021, doi: 10.1007/s12540-020-00885-5.
[85] A. Mittal, I. Roy, and S. Gandhi, “Magnetic Nanoparticles: An Overview for Biomedical Applications,” *Magnetochemistry*, vol. 8, no. 9, Art. no. 9, Sep. 2022, doi: 10.3390/magnetochemistry8090107.
[86] R. S. Kumar and D. J. Krishna, “Differential Scanning Calorimetry (DSC) Analysis Of Latent Heat Storage Materials For Low Temperature (40-80oC) Solar Heating Applications,” *Int. J. Eng. Res. Technol.*, Aug. 2013, Accessed: Jul. 09, 2024. [Online]. Available: https://www.semanticscholar.org/paper/Differential-Scanning-Calorimetry-%28DSC%29-Analysis-Of-Kumar-Krishna/0d015c16fa0a84033d9a7b8ea42e1c34458403a7
[87] “Thermal Analysis of Phase Change Materials – Three Organic Waxes using TGA, DSC, and Modulated DSC® - TA Instruments.” Accessed: Jul. 31, 2024. [Online]. Available: https://www.tainstruments.com/applications-notes/thermal-analysis-of-phase-change-materials-three-organic-waxes-using-tga-dsc-and-modulated-dsc/
[88] Y. Y. Shao, M. X. Zhang, Y. Zhang, A. R. Yan, and J. Liu, “Effect of annealing on the structure and magnetic entropy change of Mn1.1Fe0.9P0.8Ge0.2 ribbons,” *J. Magn. Magn. Mater.*, vol. 362, pp. 90–92, Aug. 2014, doi: 10.1016/j.jmmm.2014.03.047.
[89] T. Ungár, “Microstructural parameters from X-ray diffraction peak broadening,” *Scr. Mater.*, vol. 51, no. 8, pp. 777–781, Oct. 2004, doi: 10.1016/j.scriptamat.2004.05.007.
[90] B. Abraime *et al.*, “Influence of synthesis methods with low annealing temperature on the structural and magnetic properties of CoFe2O4 nanopowders for permanent magnet application,” *J. Magn. Magn. Mater.*, vol. 500, p. 166416, Apr. 2020, doi: 10.1016/j.jmmm.2020.166416.
[91] T. Nguyen, “First-order phase transitions and giant magnetocaloric effect,” Dissertation (TU Delft), Casimir PhD Series, Delft-Leiden, 2010.
[92] R. Buchwald, M. D. Breed, and A. R. Greenberg, “The thermal properties of beeswaxes: unexpected findings,” *J. Exp. Biol.*, vol. 211, no. 1, pp. 121–127, Jan. 2008, doi: 10.1242/jeb.007583.
[93] S. Nain, N. Kumar, B. Chudasama, and P. Kumar Avti, “The SLP estimation of the nanoparticle systems using size-dependent magnetic properties for the magnetic hyperthermia therapy,” *J. Magn. Magn. Mater.*, vol. 565, p. 170219, Jan. 2023, doi: 10.1016/j.jmmm.2022.170219.
[94] K. Simeonidis *et al.*, “Fe-based nanoparticles as tunable magnetic particle hyperthermia agents Fe-based nanoparticles as tunable magnetic particle hyperthermia agents,” *Journal of Applied Physics*, vol. 114. Sep. 12, 2013. doi: 10.1063/1.4821020.
[95] R. Ferrero *et al.*, “Experimental and Modelling Analysis of the Hyperthermia Properties of Iron Oxide Nanocubes,” *Nanomaterials*, vol. 11, no. 9, p. 2179, Aug. 2021, doi: 10.3390/nano11092179.